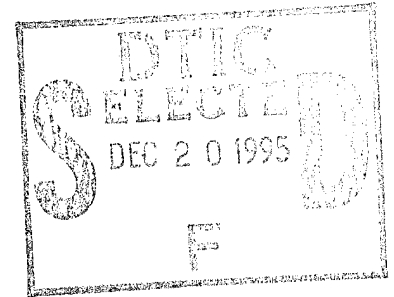
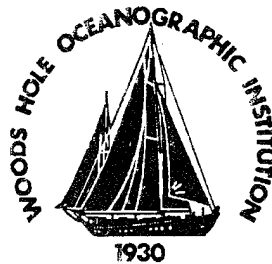


**Woods Hole  
Oceanographic  
Institution**



---

**ADCP Measurements from the  
ICESHELF 94 Experiment**

by

Albert J. Plueddemann and Nancy R. Galbraith

September 1995

**Technical Report**

Funding was provided by the Office of Naval Research through Contract  
No. N00014-90-J-1359.

Approved for public release; distribution unlimited.

---

19951218 107

DTIC QUALITY INSPECTED 1

WHOI-95-11

ADCP Measurements from the  
ICESHELF 94 Experiment

by

Albert J. Plueddemann and Nancy R. Galbraith

Woods Hole Oceanographic Institution  
Woods Hole, Massachusetts 02543

September 1995

**Technical Report**

Funding was provided by the Office of Naval Research through Contract  
No. N00014-90-J-1359.

Reproduction in whole or in part is permitted for any purpose of the United States  
Government. This report should be cited as Woods Hole Oceanog. Inst. Tech. Rept.,  
WHOI-95-11.

Approved for public release; distribution unlimited.

Approved for Distribution:



Philip L. Richardson, Chair  
Department of Physical Oceanography

Accession For	
NTIS CRA&I	<input checked="checked" type="checkbox"/>
DTIC TAB	<input type="checkbox"/>
Unannounced	<input type="checkbox"/>
Justification	
By	
Distribution /	
Availability Codes	
Dist	Avail and/or Special
A-1	

## Abstract

The ICESHELF 94 Experiment was conducted during April of 1994 from an ice camp in the Lincoln Sea at approximately  $84^{\circ}$  N,  $63^{\circ}$  W. An Acoustic Doppler Current Profiler (ADCP) was operated at the camp from 8 to 24 April in order to characterize the internal wave field at the site. The ADCP was suspended below the ice with transducers facing downwards from a depth of 12 m. This report describes the ADCP configuration and presents the raw data recorded by the ADCP. The processing steps involved in computing horizontal velocities in geographic coordinates from the raw data are described, and time series and spectra of the resulting velocity data are presented. Horizontal velocities of good quality (estimated precision of about  $1 \text{ cm s}^{-1}$ ) were obtained between 27.7 m and 137.0 m depth with 7.8 m resolution. Data were obtained at five minute intervals, but averaged to 1 hr during processing to suppress instrument noise. Spectra show the velocity field to be dominated by variance at semi-diurnal frequency, with a maximum in energy between 50 and 110 m depth. The semi-diurnal tidal frequency ( $M_2 = 0.0805 \text{ cph}$ ) cannot be distinguished from the local inertial frequency ( $f = 0.0829 \text{ cph}$ ) in the records. Maximum amplitudes of 8 to  $10 \text{ cm s}^{-1}$  were seen near 80 m depth. Velocities from an InterOcean S4 current meter deployed at the same site were compared to those from the ADCP. Typical comparisons showed component velocity differences with means of less than  $0.5 \text{ cm s}^{-1}$  and standard deviations from 1.0 to  $1.5 \text{ cm s}^{-1}$ . The largest differences were associated with peaks in the semi-diurnal oscillations, with the S4 underspeeding relative to the ADCP.

# Contents

<b>Abstract</b>	<b>1</b>
<b>List of Tables and Figures</b>	<b>3</b>
<b>1 Introduction</b>	<b>6</b>
<b>2 ADCP Data</b>	<b>10</b>
2.1 Configuration . . . . .	10
2.2 Leader data . . . . .	12
2.3 Profile data in beam coordinates . . . . .	19
2.4 Velocity in geographic coordinates . . . . .	35
<b>3 ADCP – S4 Comparisons</b>	<b>53</b>
<b>Acknowledgments</b>	<b>84</b>
<b>References</b>	<b>85</b>



## List of Figures

1	ICESHELF 94 experimental site . . . . .	7
2	ICESHELF 94 camp position . . . . .	8
3	ICESHELF 94 CTD profile . . . . .	9
4	Ensemble number and BIT status . . . . .	14
5	Voltages and current . . . . .	15
6	Temperature . . . . .	16
7	Tilt and heading . . . . .	17
8	Tilt and heading standard deviation . . . . .	18
9	Beam 1 radial velocity . . . . .	21
10	Beam 2 radial velocity . . . . .	22
11	Beam 3 radial velocity . . . . .	23
12	Beam 4 radial velocity . . . . .	24
13	Beam 1 echo amplitude . . . . .	25
14	Beam 2 echo amplitude . . . . .	26
15	Beam 3 echo amplitude . . . . .	27
16	Beam 4 echo amplitude . . . . .	28
17	Beam 1 percent good . . . . .	29
18	Beam 2 percent good . . . . .	30
19	Beam 3 percent good . . . . .	31
20	Beam 4 percent good . . . . .	32
21	Beam 3 echo amplitude, 9-12 April . . . . .	33
22	Beam 3 radial velocity, 9-12 April . . . . .	34
23	Raw and filtered heading . . . . .	39
24	East velocity . . . . .	40
25	North velocity . . . . .	41
26	East velocity, 8-16 April . . . . .	42

27	East velocity, 16-24 April . . . . .	43
28	North velocity, 8-16 April . . . . .	44
29	North velocity, 16-24 April . . . . .	45
30	Vertical velocity . . . . .	46
31	Error velocity . . . . .	47
32	Velocity spectra at 35.5 m . . . . .	48
33	Velocity spectra at 82.3 m . . . . .	49
34	Velocity spectra at 121.4 m . . . . .	50
35	Clockwise rotary spectra vs. depth . . . . .	51
36	Anti-clockwise rotary spectra vs. depth . . . . .	52
37	ADCP vs. S4 east at 75 m . . . . .	56
38	ADCP vs. S4 north at 75 m . . . . .	57
39	ADCP vs. S4 speed at 75 m . . . . .	58
40	ADCP vs. S4 direction at 75 m . . . . .	59
41	ADCP vs. S4 east at 105 m . . . . .	60
42	ADCP vs. S4 north at 105 m . . . . .	61
43	ADCP vs. S4 speed at 105 m . . . . .	62
44	ADCP vs. S4 direction at 105 m . . . . .	63
45	Speed scatter plot at 75 m . . . . .	64
46	Direction scatter plot at 75 m . . . . .	65
47	Speed scatter plot at 105 m . . . . .	66
48	Direction scatter plot at 105 m . . . . .	67
49	Profile comparison for S4-04 . . . . .	68
50	Profile comparison for S4-06 . . . . .	69
51	Profile comparison for S4-07 . . . . .	70
52	Profile comparison for S4-08 . . . . .	71
53	Profile comparison for S4-09 . . . . .	72

54	Profile comparison for S4-10 . . . . .	73
55	Profile comparison for S4-12 . . . . .	74
56	Profile comparison for S4-14 . . . . .	75
57	Profile comparison for S4-16 . . . . .	76
58	Profile comparison for S4-18 . . . . .	77
59	Profile comparison for S4-19 . . . . .	78
60	Profile comparison for S4-22 . . . . .	79
61	Profile comparison for S4-24 . . . . .	80
62	Profile comparison for S4-26 . . . . .	81
63	Profile comparison for S4-29 . . . . .	82
64	Profile comparison for S4-32 . . . . .	83

## List of Tables

1	ADCP parameter settings . . . . .	11
2	Depths for the fifteen velocity records . . . . .	36
3	ADCP – S4 comparison summary . . . . .	55

# 1 Introduction

The ICESHELF 94 Experiment was conducted between 18 March and 9 June 1994 from an ice camp at the edge of the continental shelf in the Arctic Ocean. The experiment included observations of environmental, oceanographic and underwater acoustic parameters. The measurements reported here were a part of the oceanographic background data collected in conjunction with underwater acoustics studies. The nominal camp location was  $84^{\circ}$  N,  $63^{\circ}$  W, between northern Greenland and the Queen Elizabeth Islands in the Lincoln Sea (Figure 1). The water depth was about 500 m at the experimental site. North of the site, topography is dominated by the intersection of the Lomonosov Ridge with the shelf. The camp position was monitored using a Global Positioning System (GPS) receiver between 4 and 26 April (Figure 2). The mean GPS position was  $83^{\circ} 53'$  N,  $62^{\circ} 58'$  W. The net camp displacement was about 4 km to the west, and only 310 m to the south. The camp was effectively stationary between 7 and 18 April. The most rapid camp motion was between 19 and 22 April, with drift speeds of about  $2.0 \text{ cm s}^{-1}$  to the northwest. A typical CTD cast from the camp (Figure 3) shows a mixed layer extending to about 45 m depth, an upper pycnocline associated with a sub-surface temperature maximum extending from 50 to 110 m depth, and a lower pycnocline between 120 and 220 m where both temperature and salinity increase steadily with depth.

This report describes data from an Acoustic Doppler Current Profiler (ADCP) used to characterize the internal wave field in the upper pycnocline. The internal wave measurements were a joint effort between Woods Hole Oceanographic Institution (WHOI) and the Naval Research and Development (NRaD) branch of the Naval Command and Control Ocean Surveillance Center in San Diego. WHOI supplied a 300 kHz RD Instruments ADCP and associated hardware for deployment. The instrument was deployed, operated, and recovered by NRaD. The ADCP was operated at the camp from 7 to 24 April. High quality velocity data were obtained for 15 depth cells between 27.7 m and 137.0 m depth with vertical resolution of 7.8 m and estimated precision of about  $1 \text{ cm s}^{-1}$ . This report presents the principal variables measured by the ADCP, including instrument performance parameters, instrument orientation, Doppler velocity, backscattered echo amplitude, and data quality parameters. The second section summarizes the ADCP configuration, describes the processing steps involved in computing horizontal velocities in geographic coordinates, and presents time series and spectra of the resulting velocity data.

An InterOcean S4 electro-magnetic current meter was also deployed at the camp. A combination of fixed-depth time series and vertical profiling was done between 9 and 24 April. The S4 velocity data are compared to those from the ADCP as a means of assessing the relative performance of the two instruments. The fourth section shows the results of the ADCP-S4 comparison study.

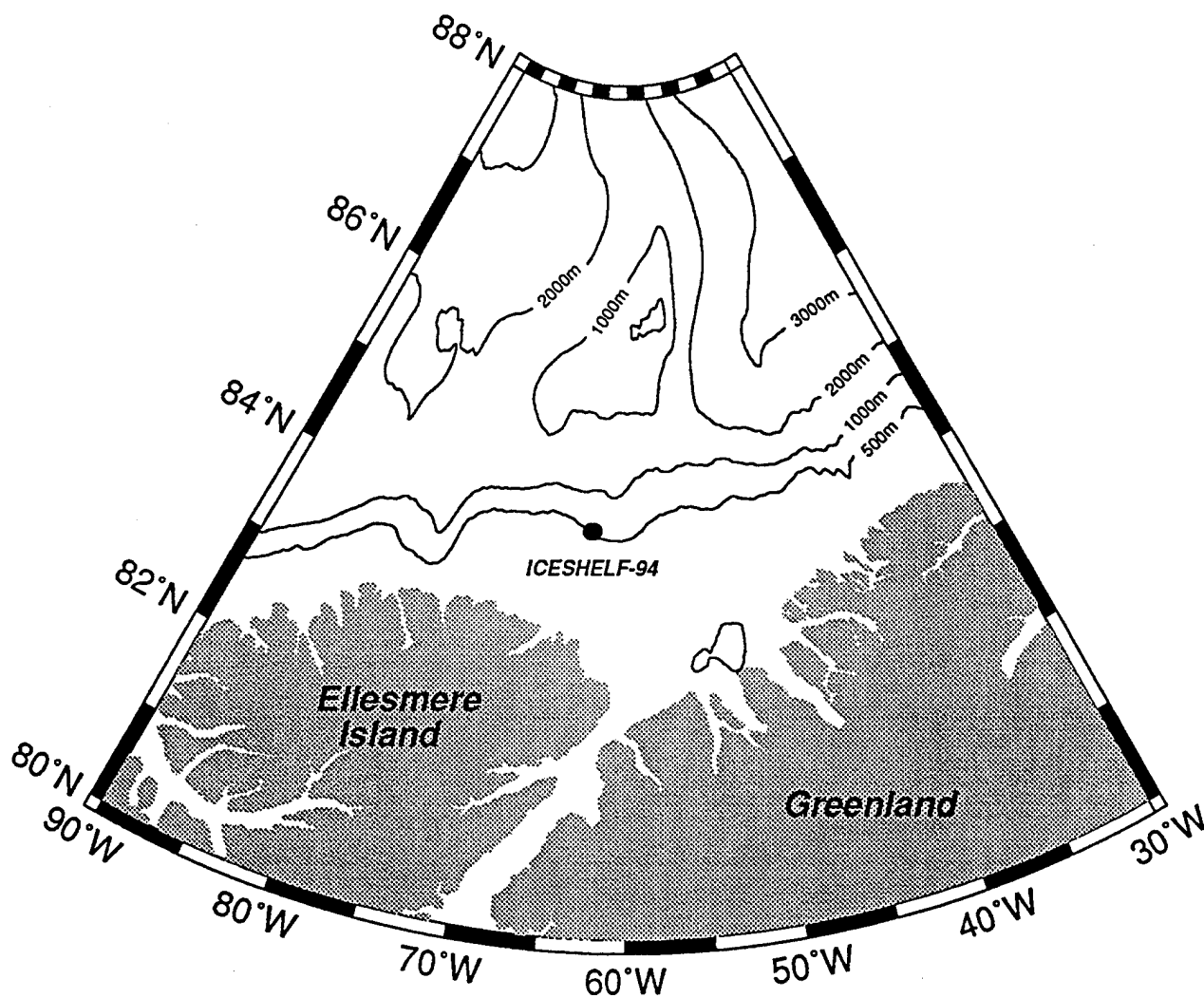


Figure 1: Location of the ICESHELF 94 ice camp in the Lincoln Sea. The principal topographic feature is the Lomonosov Ridge to the north of the camp.

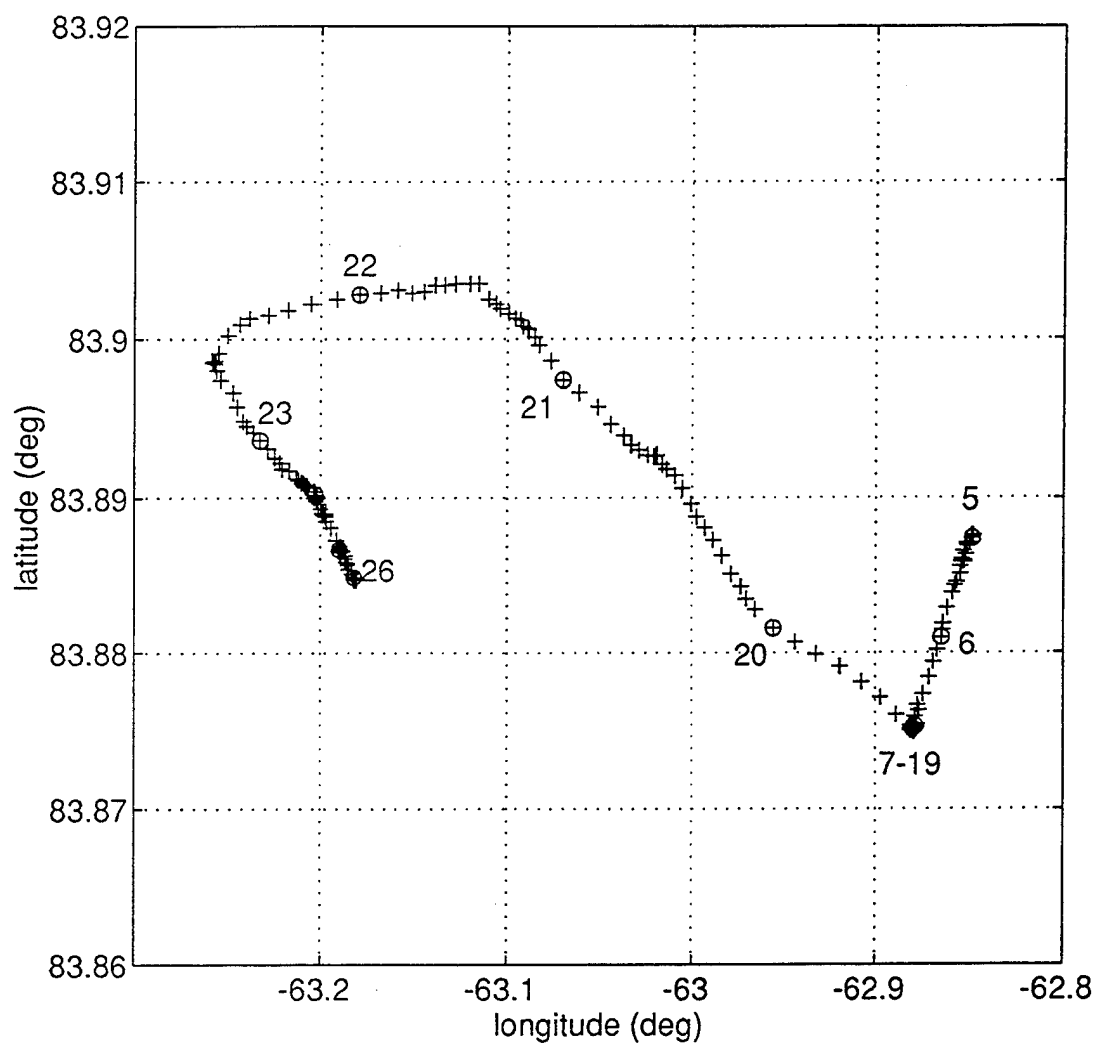


Figure 2: Position of the ICESHELF 94 ice camp from 4–26 April. Hourly GPS positions, shown as crosses, were generated from data recorded at 30 s intervals. Positions from the first hour of each day are circled and labeled with the day in April.

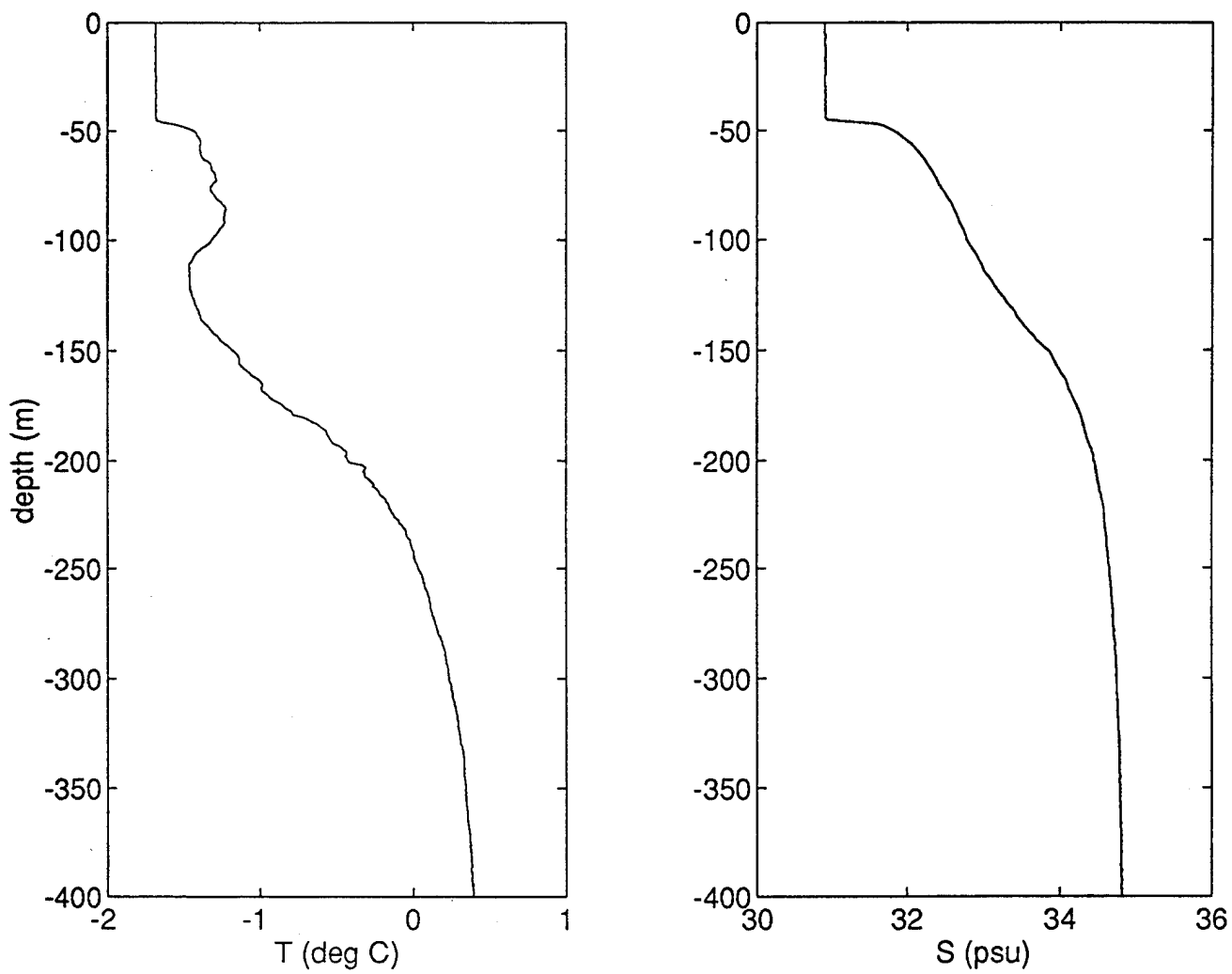


Figure 3: Typical profiles of temperature (left) and salinity (right) in the upper 400 m. These profiles are from 1517 UT 11 April 1994.

## 2 ADCP Data

### 2.1 Configuration

The ADCP was a 300 kHz, self-contained unit manufactured by RD Instruments and outfitted with pendulum tilt sensors, a flux gate compass, and 8 Mbyte of solid-state memory. The instrument was fitted to a steel load cage and deployed through a 36" diameter ice hole prepared with a hot-water drill ring. Chain was used to suspend the instrument with the transducers facing downwards at a depth of 12 m. The four transducers transmit acoustic energy along narrow beams (approximately 4° half-power beamwidth) insonifying a volume of fluid determined by the beamwidth, the duration of the acoustic pulse, and the distance from the transducers. Backscattered energy from the volume insonified by the transmitted pulse arrives at the transducers with a Doppler shift proportional to the average speed of the scatterers in the volume. To the extent that the scatterers are advected with the fluid, Doppler shifts estimated at successive times after transmission provide a profile of water velocity as a function of distance along the beam. The four downward-slanting beams are separated by 90° in azimuth and pointed downward at an angle of 60° from the horizontal. Each beam provides a profile of radial (along-beam) velocity that contains contributions from both horizontal and vertical components of the fluid velocity. The four beams form two, co-planar "Janus" pairs that can be used to separate horizontal and vertical velocity components for motions with horizontal scales large compared to the separation between the beams (Rowe and Young, 1979; Joyce *et al.*, 1982).

The principal parameter settings for the ICESHELF 94 ADCP are summarized in Table 1. Additional information on ADCP operating parameters and their interpretation can be found in the manufacturers literature (RD Instruments, 1989).

The ADCP was configured to send out 100 pulsed transmissions with a duration of 12.53 ms from each transducer at 0.6 s intervals for a period of 1 min. This sequence of transmissions, called an ensemble, was repeated at 5 min intervals. The backscattered signal from each transmission was processed over equally spaced time intervals corresponding to successively deeper insonified volumes known as depth cells. The depth cell length is the vertical component of the insonified volume. Using the default soundspeed of  $1475 \text{ m s}^{-1}$ , the processing interval corresponded to a 4 m depth cell length and the pulse duration to 8 m depth resolution (Table 1). Thus, the data were "oversampled" by a factor of two in depth and adjacent depth cells were not independent. Using the *in situ* soundspeed of  $1440 \text{ m s}^{-1}$ , the actual depth cell length was 3.9 m, and the depth resolution was 7.8 m.

Fifty depth cells were recorded for each transmission, giving a nominal profiling interval of 200 m. Accounting for the *in situ* soundspeed and the depth of the transducers, the first depth cell was centered at a depth of 17.9 m and the center of



parameter	value
time between pings (sec)	0.6
pings per ensemble	100
ensemble interval (sec)	300
number of depth cells	50
depth cell length (m)	4
transmit pulse length (m)	8
blank after transmit (m)	0
transducer depth (m)	12
pitch/roll compensation	off
heading compensation	off
bottom track	off

Table 1: Principal parameter settings for the ICESHELF 94 ADCP. Most parameters not shown in the table were set to their default values.

the last cell was at a depth of 209.2 m. The transient response of the electronics to the pulse transmission typically corrupts the first few depth cells, and the manufacturer recommends a "blank" period before the first processing interval. However, no blanking was used for the ICESHELF 94 deployment. Assessment of the data showed that the third depth cell (25.7 m depth) was the first one which was not corrupted by the transient response. Because of the attenuation and spreading of the transmitted signal, the backscattered energy level decays with range  $r$  as approximately  $r^{-2}$ , and the maximum depth is not always attainable before the signal is lost in the background noise of the system. During the ICESHELF 94 deployment data of consistently high quality were seldom found below depth cell 32 (139.0 m depth) and were never found at the maximum profiling depth (cell 50, 209.2 m). The transient response at near-range and low signal-to-noise levels at far range combined to limit the usable profiling interval to between depth cells 3 and 32.

The precision of velocity estimates from ADCPs has been investigated theoretically by Theriault (1986). Theriault used a simplified model of the scatterer field and the velocity field to derive an expression for the lower bound on velocity estimate variance. For the instrument configuration used in this experiment, Theriault's expression results in a lower-bound standard deviation for the 100 pulse average horizontal velocities of about  $0.4 \text{ cm s}^{-1}$ . Field observations indicate that the actual velocity precision is typically larger than this theoretical lower bound by a factor of 2 or more (Pinkel, 1982; Hansen 1985). The observed velocity precision for ICESHELF 94 was estimated to be about  $1.0 \text{ cm s}^{-1}$  at mid depth, a factor of 2.5 above the theoretical

lower bound. The flux-gate compass in the ADCP was calibrated in the laboratory before and after the experiment. The results showed a typical sinusoidal error curve (Schramm, 1989) with amplitude of about  $2^\circ$ .

The velocity observed by the instrument is relative to the moving platform (i.e. the ice) to which it is attached. The effect of platform motion can be removed by adding the appropriate component of ice drift to the relative velocity measured by the instrument. Only the relative velocities, uncorrected for platform drift, are presented in this report. However, the ice velocity during ICESHELF 94 was generally small compared to the fluid velocity (Figure 2), making the drift correction insignificant. The exception was during 19–22 April when drift velocities of several  $\text{cm s}^{-1}$  were seen.

## 2.2 Leader data

The “leader” consists of configuration parameters (which are constant, even though they are recorded with every ensemble) and several variables relating to instrument performance, instrument orientation, and environmental conditions. The interesting leader variables are shown in Figures 4–8.

Figure 4 shows time series of ensemble number and Built In Test (BIT) status. The ensemble number increases monotonically, indicating no timing problems. A total of 4890 ensembles representing 17 days of data were recorded before the instrument was recovered at the termination of the experiment. Some ensembles at the start and end of the record did not contain useful data since the instrument was turned on prior to deployment and turned off after recovery. The first and last ensembles with good data were 34 and 4865, respectively. The BIT status was always zero, indicating no errors in the transmit, receive, or echo processing circuitry.

Figure 5 shows time series of ADCP voltages and current. The high voltage input is the level at the input to the transducer power amplifier. The operational range is 14–40 V, while values above 30 V are expected for a fresh battery pack. The low voltage input is a measure of the voltage to the ADCP processing electronics. The operational range is 5.5–12 V; values above 6 V are expected. The transmit current is measured at the output of the power amplifier board. Maximum current should be near 1.8 A when the high voltage input is equal to 40 V. A low current condition is indicated if the transmit current is below 1.0 A.

Figure 6 shows the time series of temperature at the transducer head (12 m depth). After an initial drop (possibly because the instrument was still equilibrating after deployment) the temperature remained constant at  $-1.84^\circ\text{C}$ . The precision of the temperature measurement is  $0.0122^\circ\text{C}$ , and the constant observed value suggests that the temperature in the mixed layer changed by less than this amount during

the experiment. Temperature calibration tests on other ADCPs have shown that typical accuracies are about  $0.10^{\circ}\text{C}$ . The ADCP temperature sensor was not calibrated for this experiment, but comparison with the CTD, which indicated a mixed layer temperature of about  $-1.68^{\circ}\text{C}$  (Figure 3), suggests a negative bias of as much as  $0.16^{\circ}$ .

Figure 7 shows time series of ensemble averaged pitch, roll, and heading in instrument coordinates. Pitch measures the tilt of the beam 3/beam 4 axis, roll measures the tilt of the beam 1/beam 2 axis, and heading measures the rotation of the transducer head (see RD Instruments, 1989 for details). Instrument tilt was constant within the noise limits of the sensors with mean values of  $0.10^{\circ}$  and  $-0.24^{\circ}$  for pitch and roll, respectively. Heading showed a periodic (once daily) oscillation with amplitude of  $5\text{--}10^{\circ}$ . The mean heading was  $-116.0^{\circ}$ .

Figure 8 shows time series of the standard deviation of pitch, roll, and heading. This is the standard deviation of the 100 pings which make up each ensemble average. Pitch and roll standard deviations are recorded with a precision of  $0.1^{\circ}$  and heading standard deviation with a precision of  $1.0^{\circ}$ . Thus, there was no significant variability in pitch, roll, or heading within the ensembles.

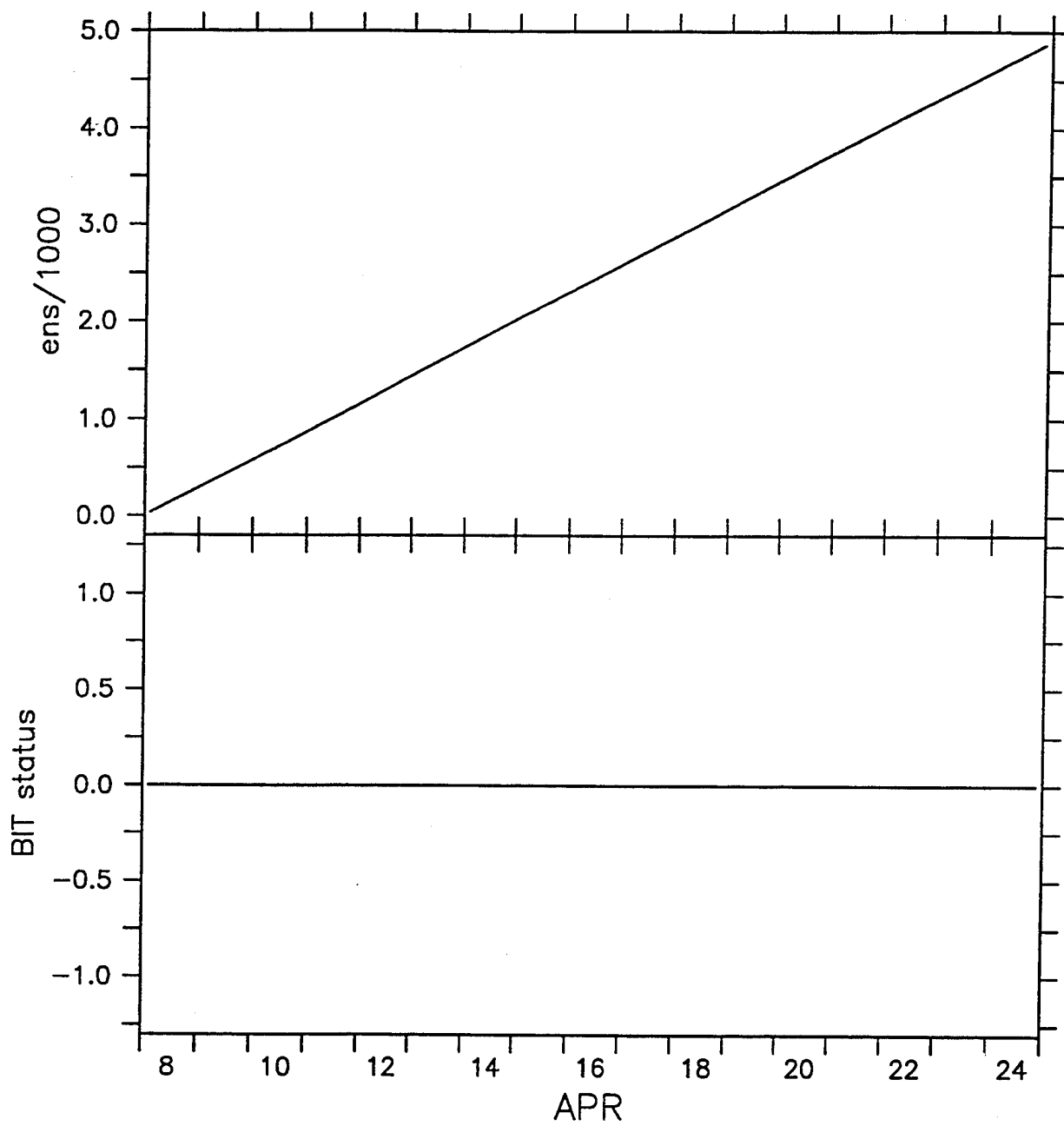


Figure 4: Time series of ensemble number (upper panel) and Built In Test (BIT) status (lower panel).

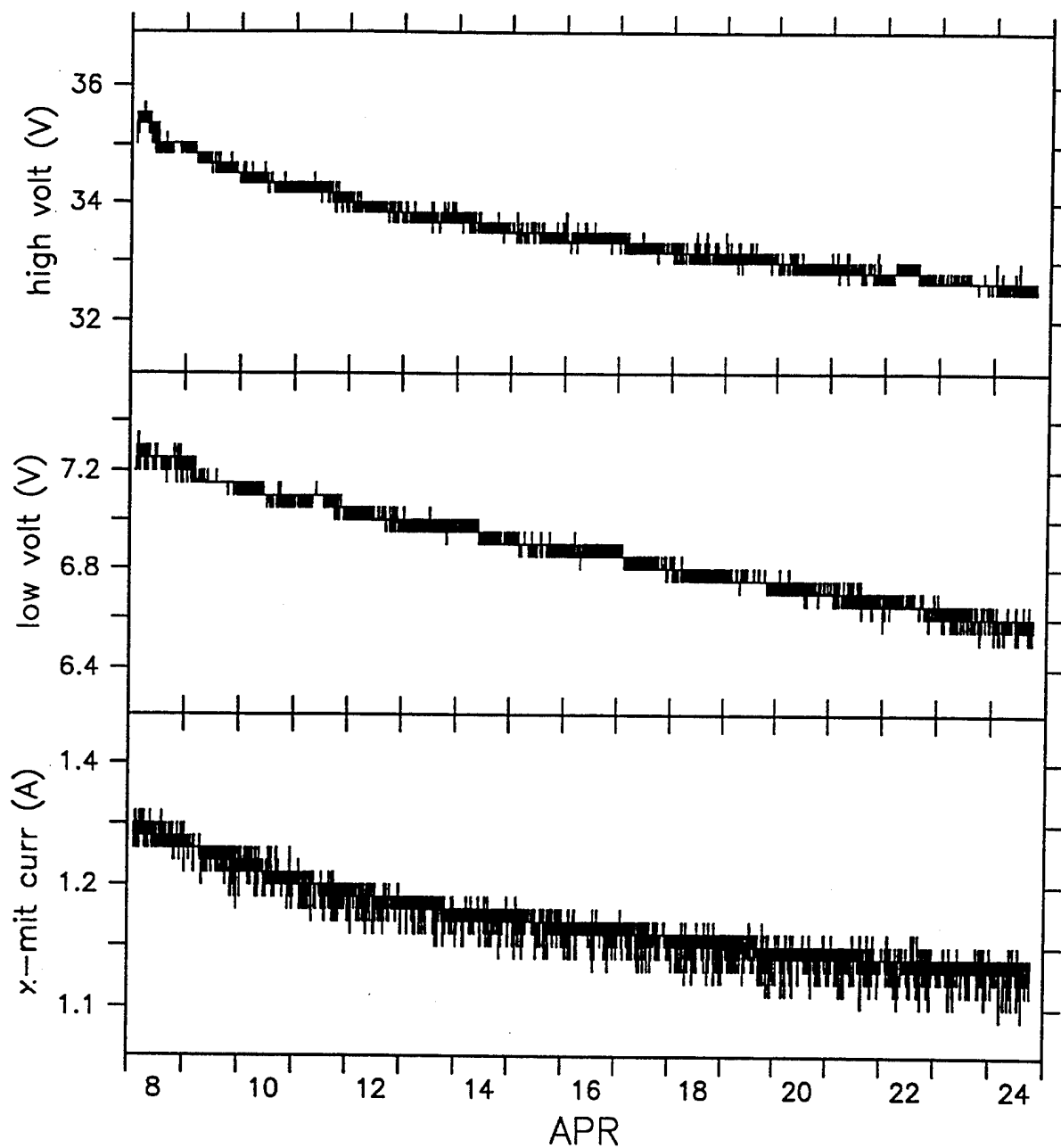


Figure 5: Time series high voltage input (upper panel), low voltage input (middle panel), and transmit current (lower panel).

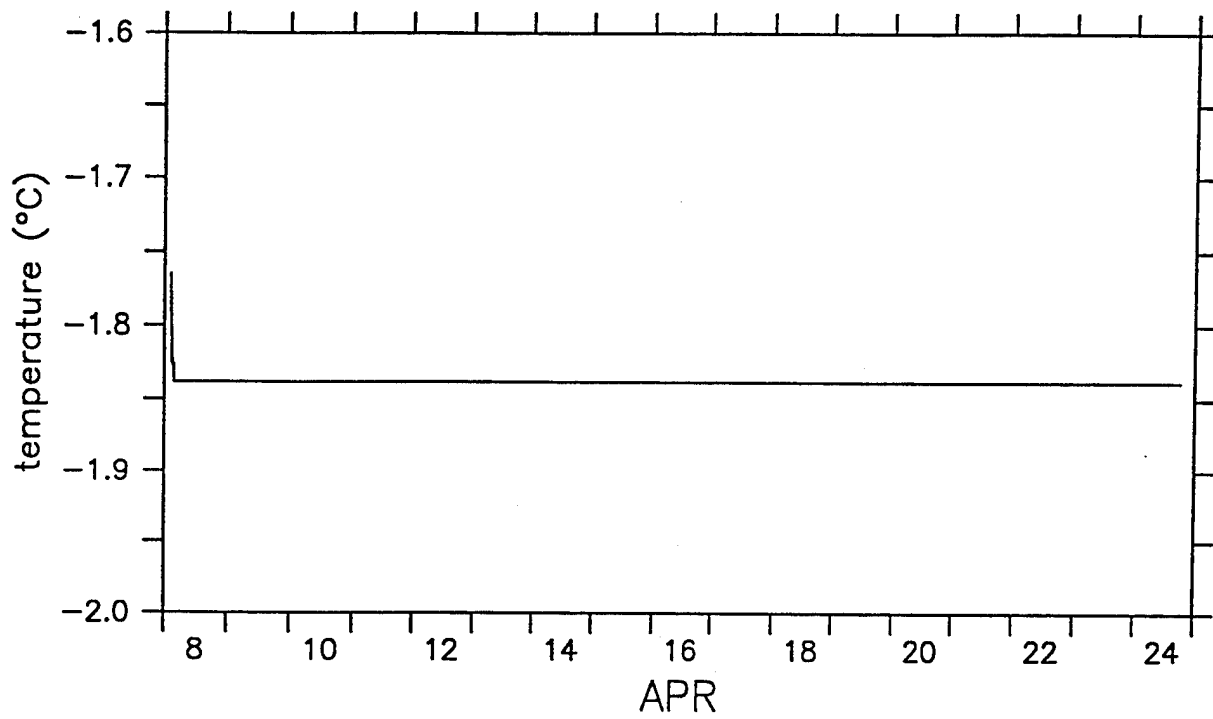


Figure 6: Time series of temperature at the transducer head.

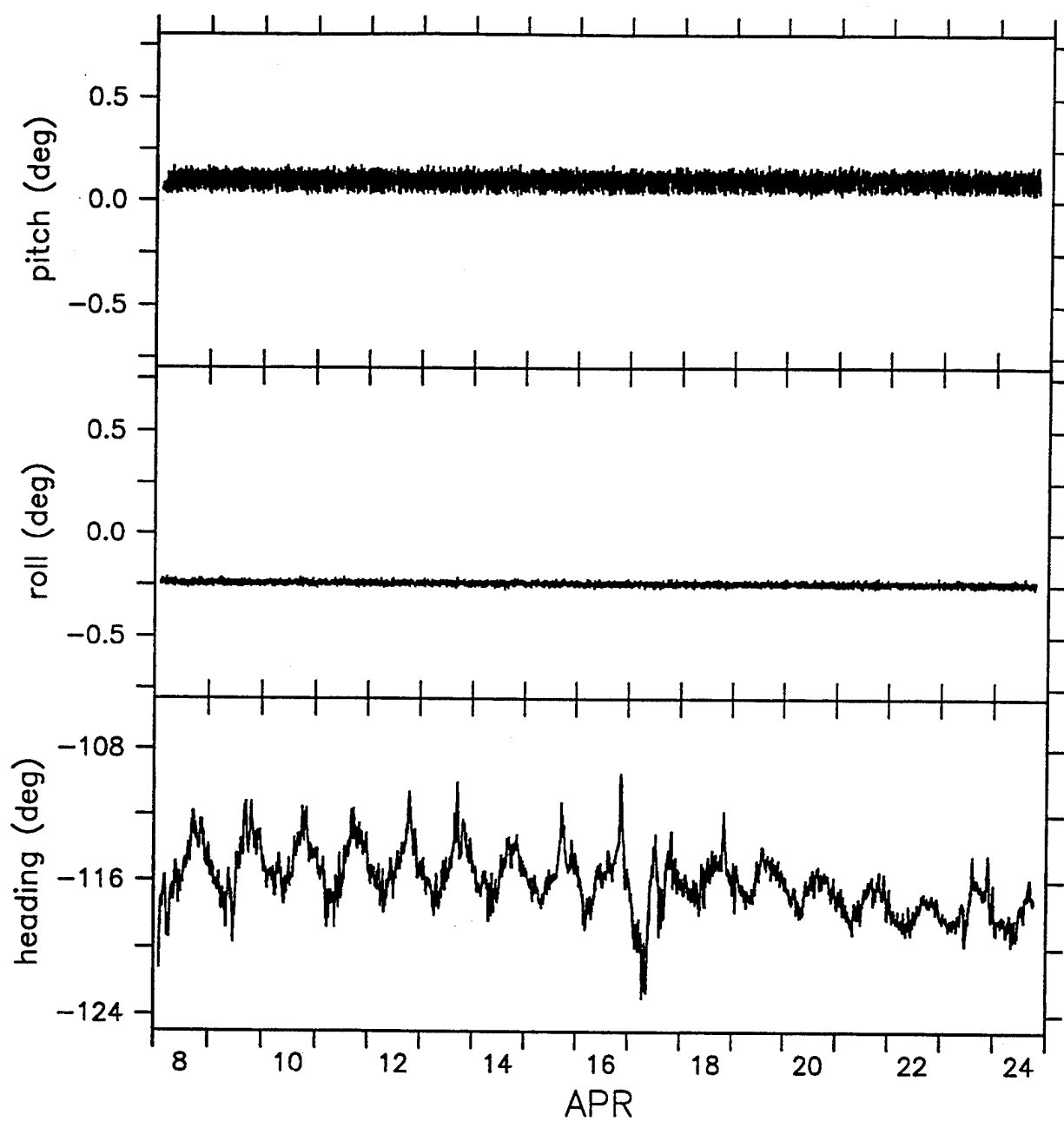


Figure 7: Time series of pitch (upper panel), roll (middle panel), and heading (lower panel) in instrument coordinates.

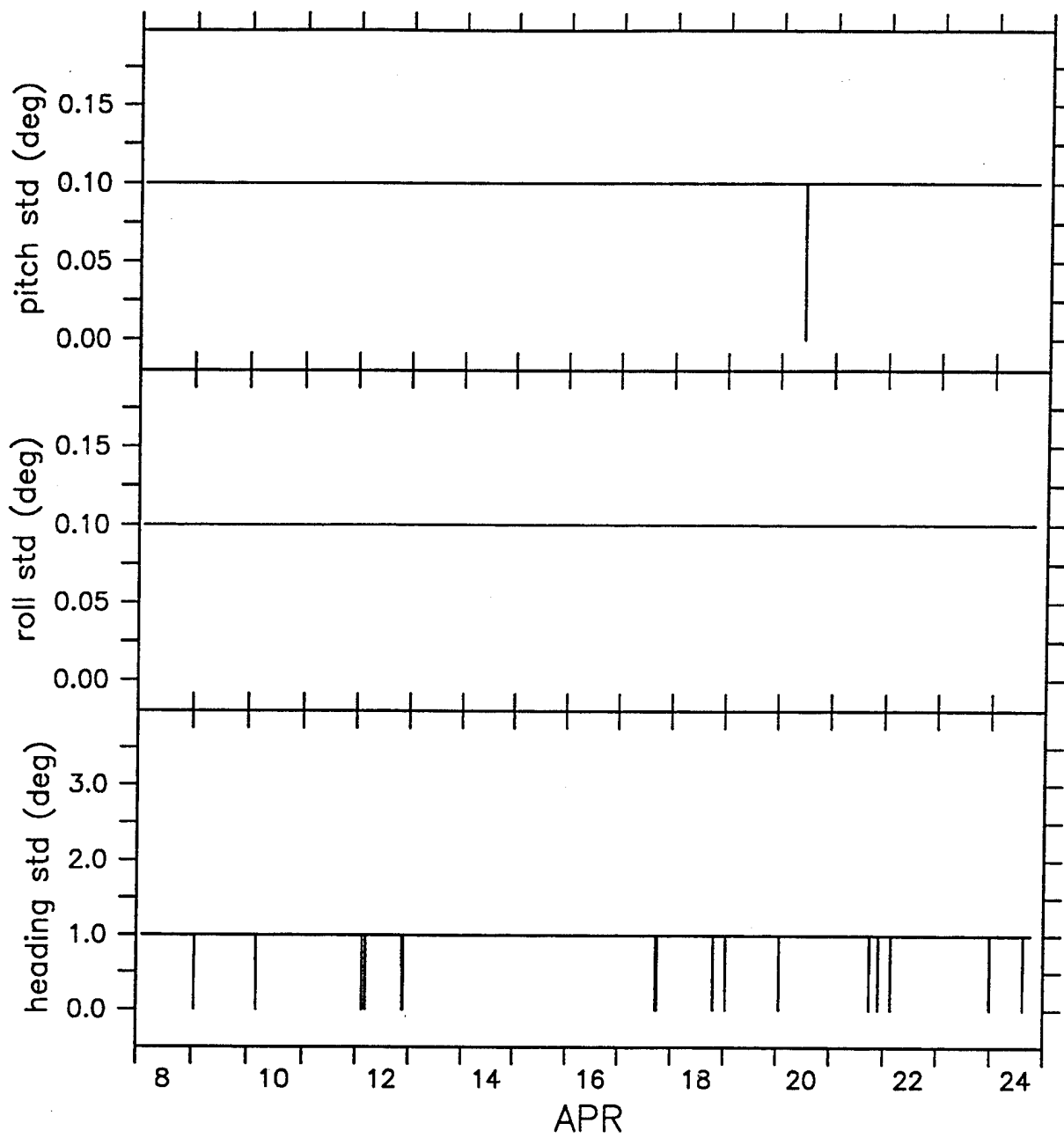


Figure 8: Time series of the standard deviation of pitch (upper panel), roll (middle panel), and heading (lower panel).



## 2.3 Profile data in beam coordinates

Three types of ensemble-averaged "profile" data were recorded: Radial velocity, echo amplitude, and a data quality parameter. The radial velocity is just the along-beam component of velocity estimated from the Doppler shift of the returned signal (Rowe and Young, 1979). The echo amplitude is a relative measure of the acoustic intensity of the backscattered signal, and is estimated from the output of an automatic gain control circuit (cf. Flagg and Smith, 1989). The data quality parameter gives the percentage of data for each ensemble which are considered "good" based on pre-set criteria such as the signal-to-noise ratio. This parameter is referred to as "percent good".

Figures 9-12 show time series of velocity in beam coordinates. The "radial" (along beam) velocity for a single beam is shown for the odd depth cells from 1 (17.9 m) to 35 (150.7 m). The first time series is "flat" because it is within the region corrupted by the transient response to the pulse transmission, as described above. The signal-to-noise ratio drops below the pre-set threshold of 6 dB between cells 31 and 35 causing "drop-outs" in the velocity. Depth cell 33 shows the effect of these drop-outs, particularly in the latter part of the deployment. Depth cell 35 is dominated by drop-outs, and only occasionally shows a good data point on the plot. Consistent, high quality data were found between cells 3 and 32. The "spikes" in the lower portion of the data from beam 3 are due to an object in the beam. An instrument package was periodically lowered and raised from a location within the ice camp which was close to the ADCP. The orientation of the ADCP resulted in beam 3 data being occasionally corrupted by the presence of the package.

Figures 13-16 show time-depth contours of echo amplitude. Amplitude is high near the transducers and decays with depth. Beams 2 and 4 appear to perform the best (showing the highest amplitude at depth) and beam 3 the worst. "Streaks" of enhanced echo amplitude from the object which corrupts the velocities in Figure 11 are identifiable in the "raw" (5 min ensemble average) echo amplitude, but not in the 3 hr averaged data presented here.

Figures 17-20 show time-depth contours of "percent good". This parameter contains essentially the same information as echo amplitude. A band of relatively low percent good related to the transient response is seen in the upper two depth cells of each beam. Percent good values are near 100 between 30 m and 80 m depth for all four beams. Percent good decreases rapidly with increasing depth below about 100 m as a result of decreasing echo amplitude and signal-to-noise ratio.

Figures 21 and 22 show expanded views of beam 3 echo amplitude and radial velocity, respectively, during 9-12 April for depths from 92.1 m to 158.5 m. This is a section where the data corruption from the profiling instrument package is particularly clear. The "streaks" of increased echo amplitude are the signature of the

package being raised upwards through the beam. The radial velocity shows anomalous behavior which is clearly related to the positions of the echo amplitude streaks. This problem only occurred in beam 3, making it possible to correct the velocity data using the information in beam 4. This correction is described in the next section.

Beam 1

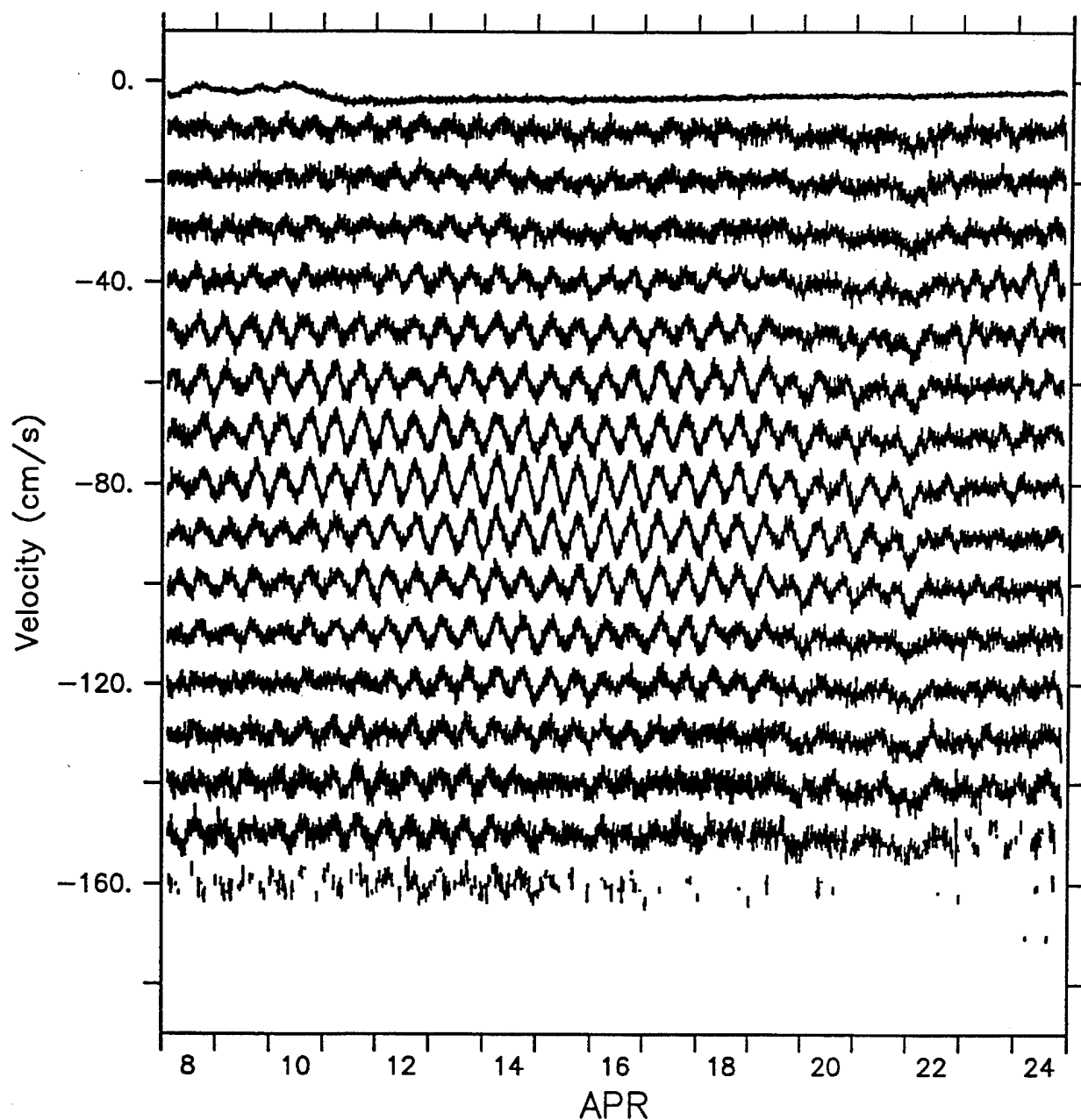


Figure 9: Time series of radial velocity: Beam 1. Odd depth cells from 1 (17.9 m) to 35 (150.7 m) are shown for each ensemble (5 min sampling period). Successive depths are offset by  $-10 \text{ cm s}^{-1}$ .

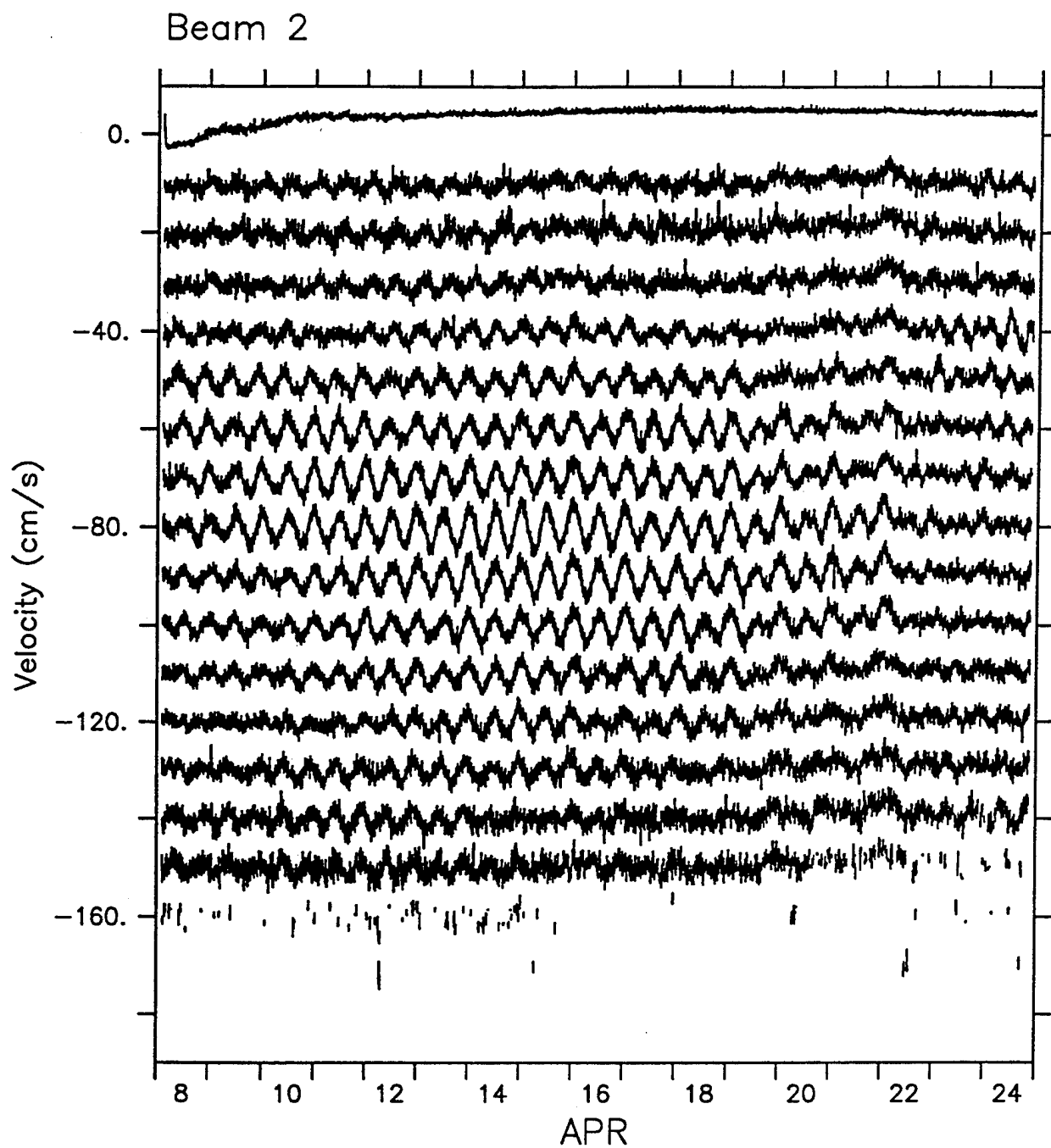


Figure 10: Time series of radial velocity: Beam 2.

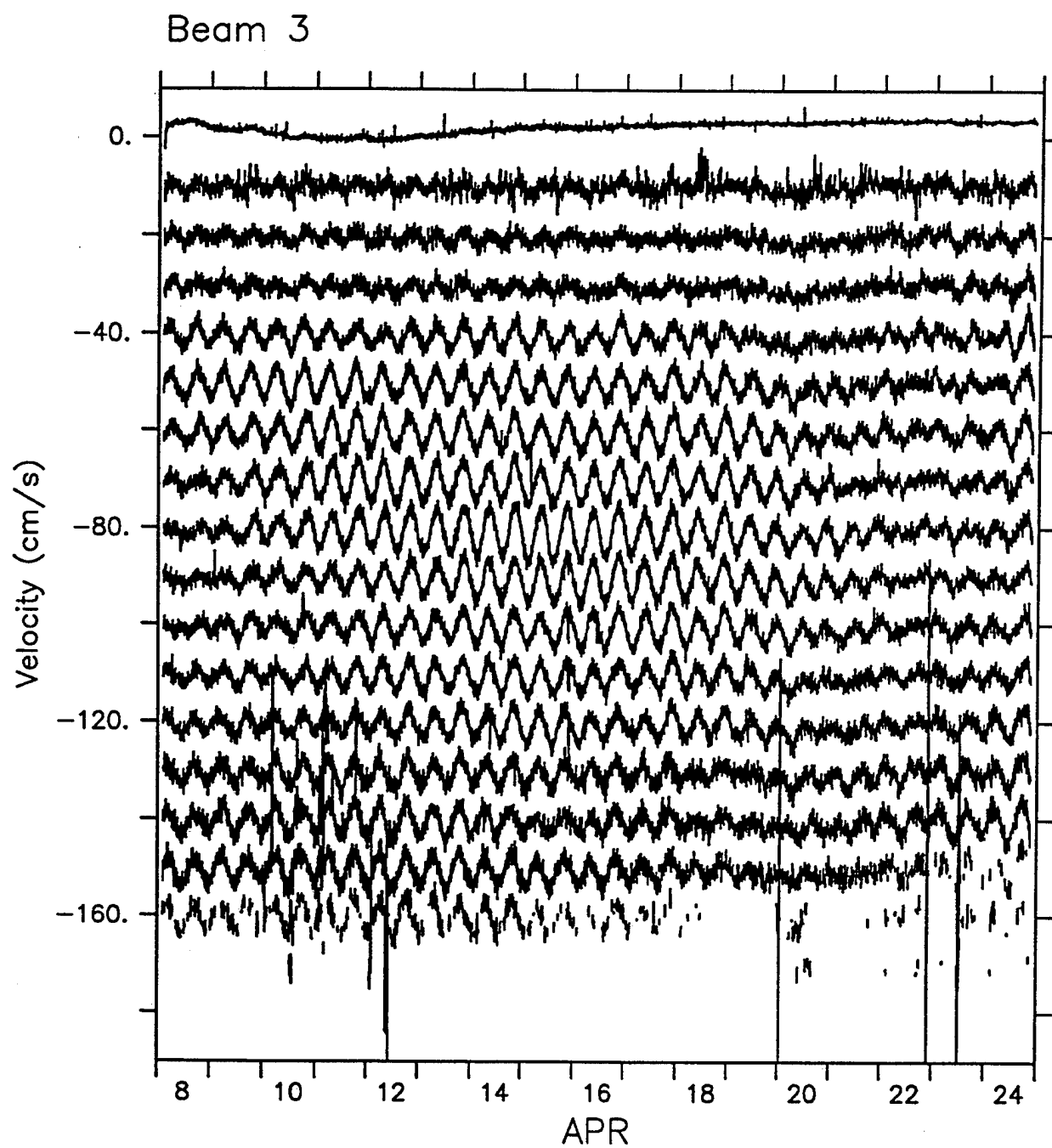


Figure 11: Time series of radial velocity: Beam 3.

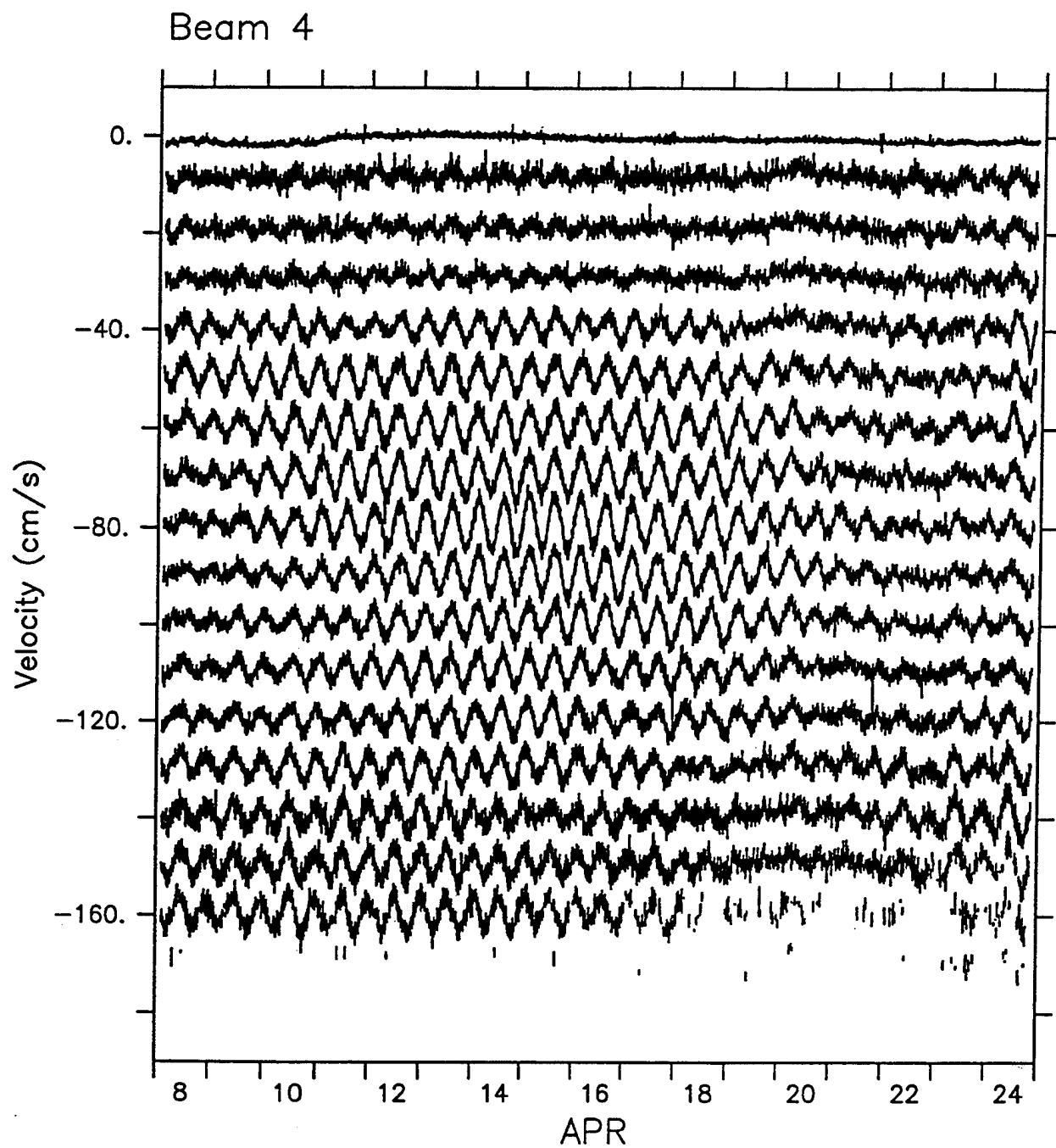


Figure 12: Time series of radial velocity: Beam 4.

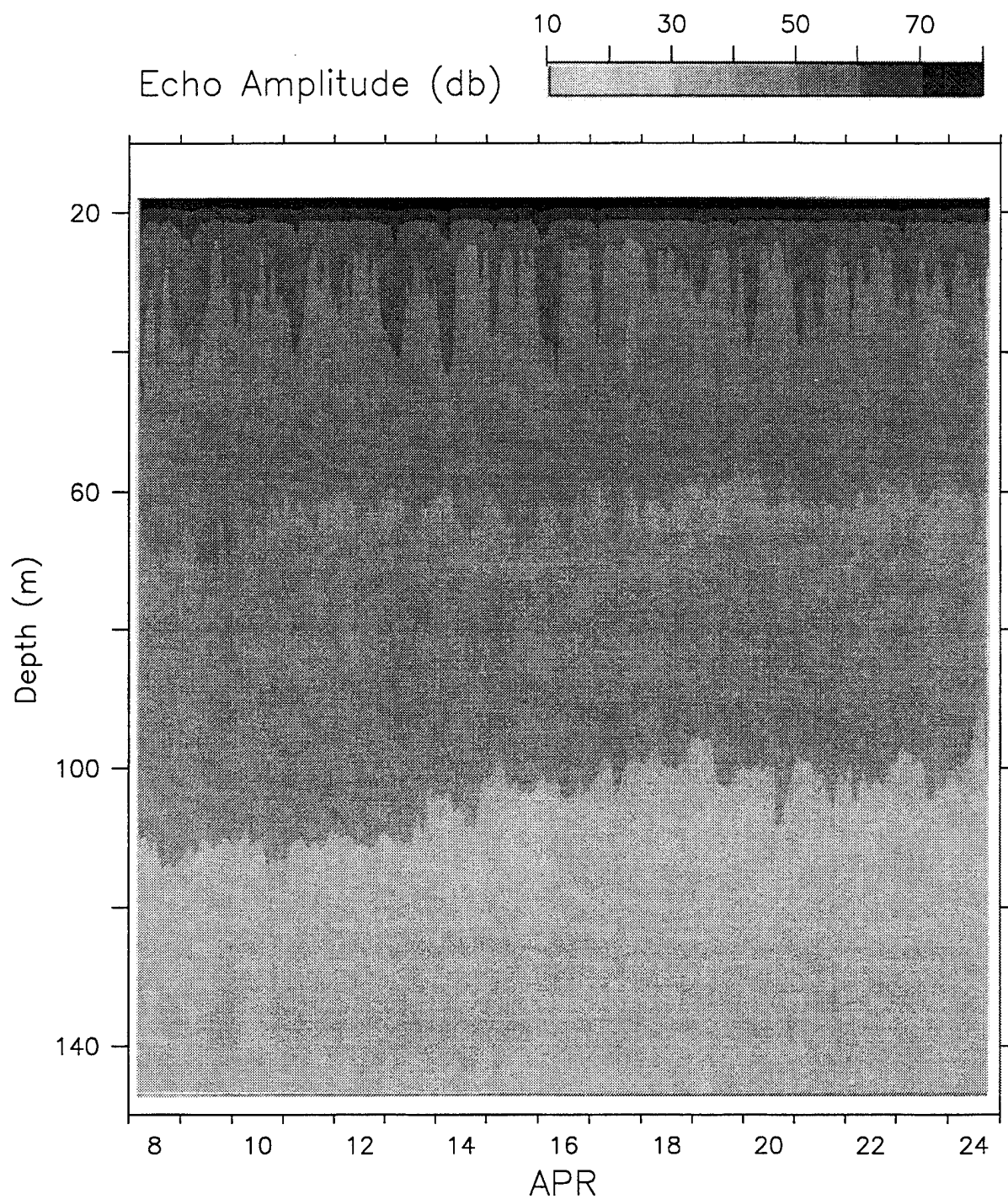


Figure 13: Time-depth contours of echo amplitude: Beam 1. Depth cells from 1 (17.9 m) to 34 (146.8 m) are contoured from 3 hour averaged data.

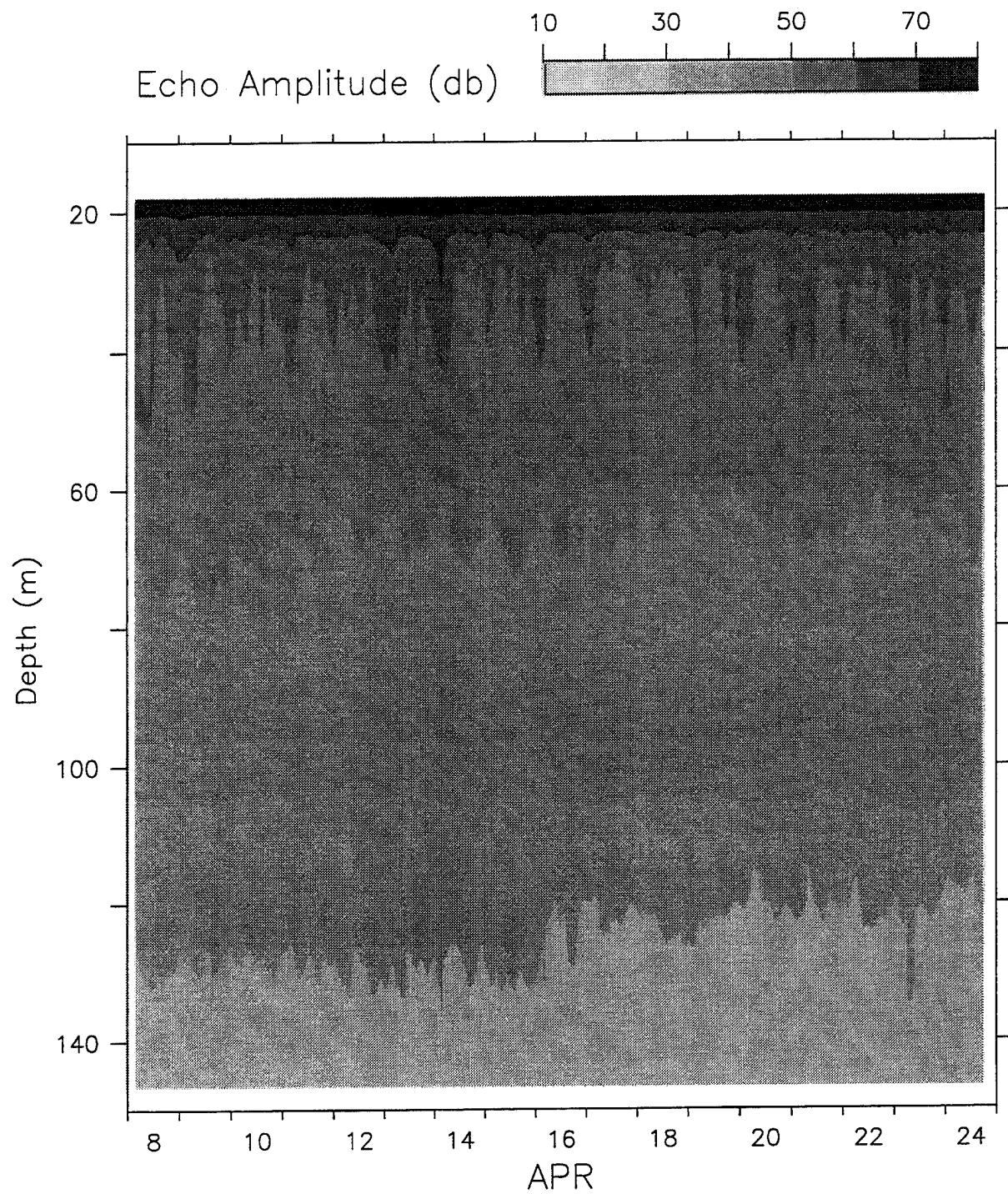


Figure 14: Time-depth contours of echo amplitude: Beam 2.



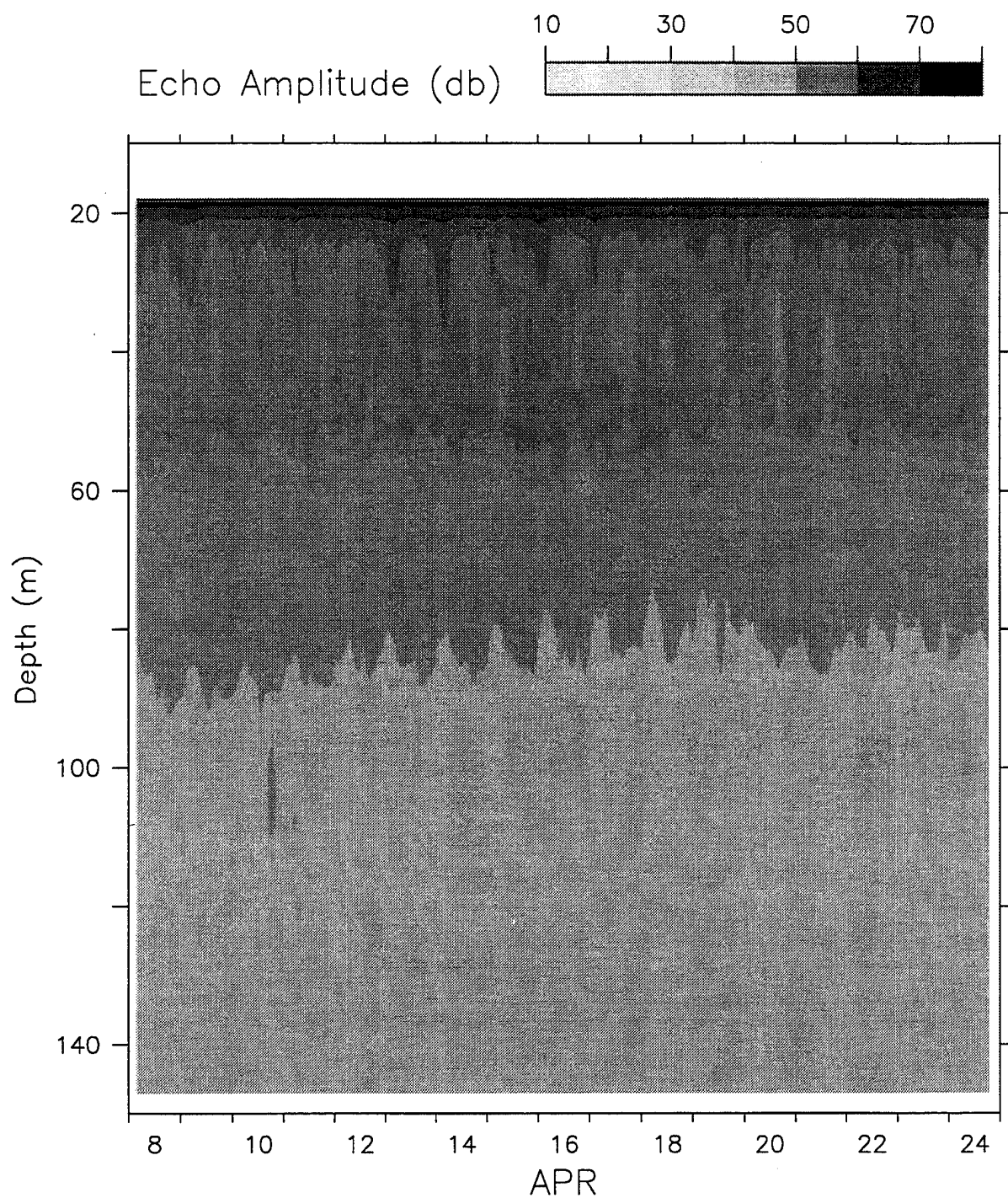


Figure 15: Time-depth contours of echo amplitude: Beam 3.

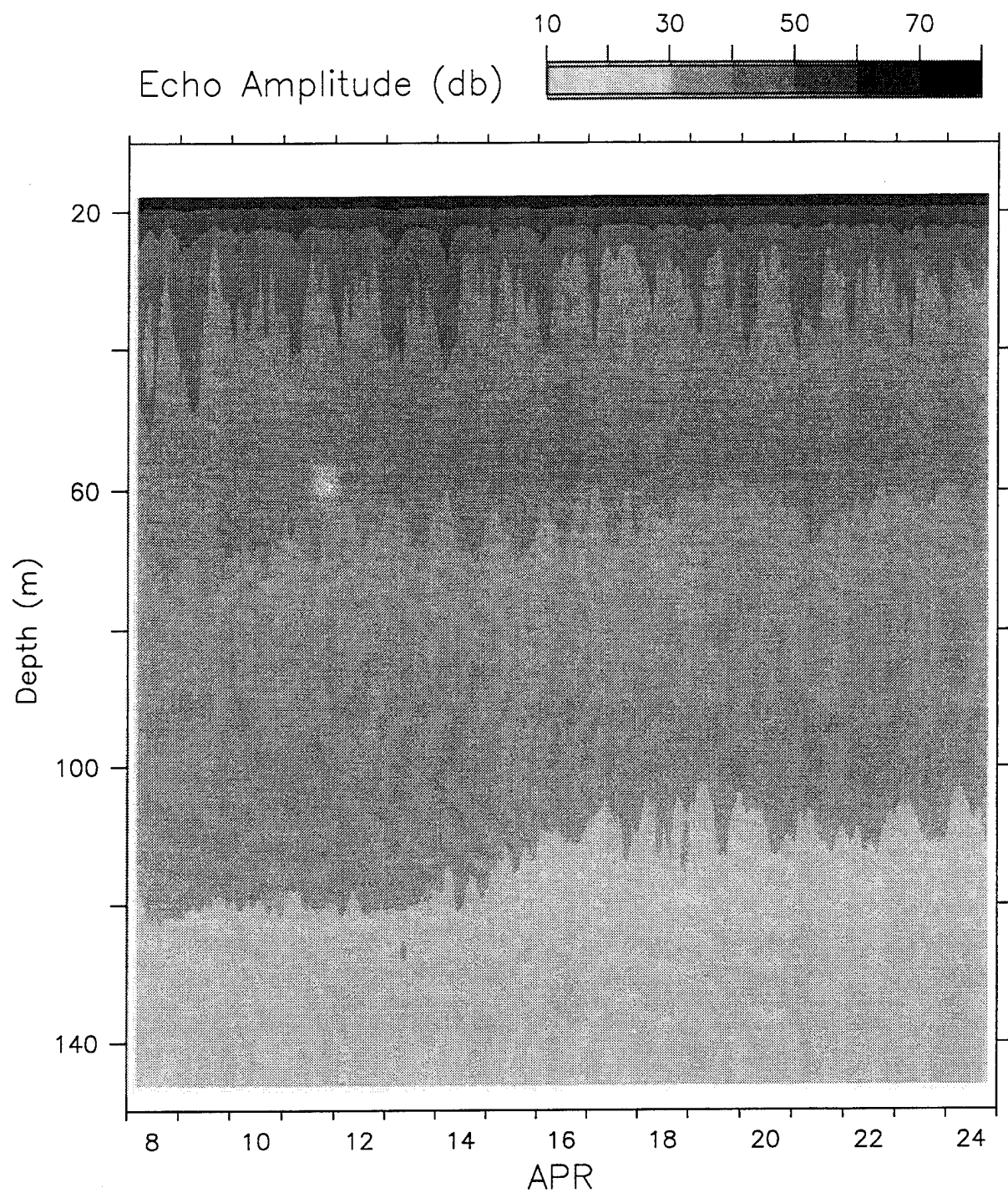


Figure 16: Time-depth contours of echo amplitude: Beam 4.

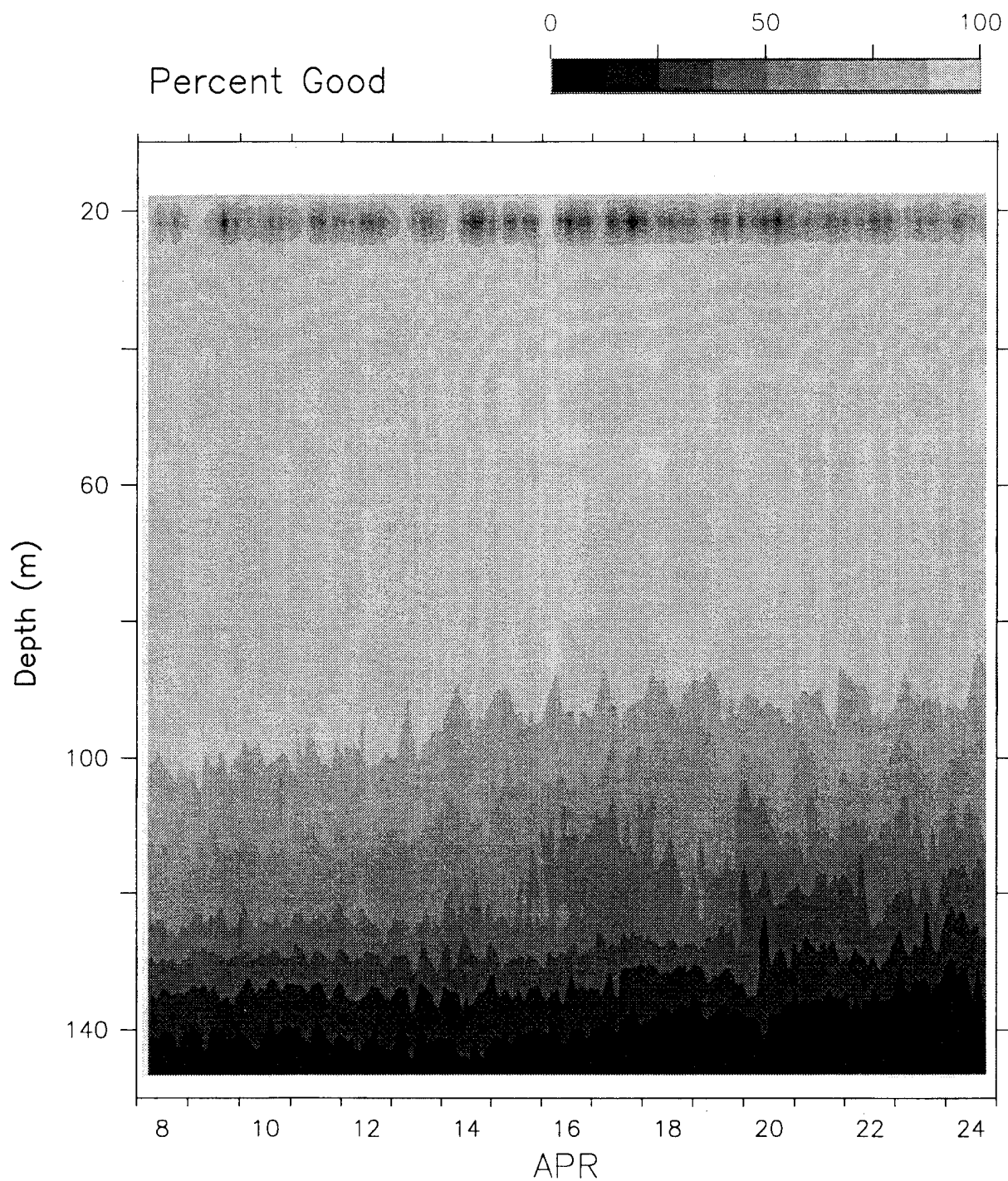


Figure 17: Time-depth contours of percent good: Beam 1. Depth cells from 1 (17.9 m) to 34 (146.8 m) are contoured from 3 hour averaged data.

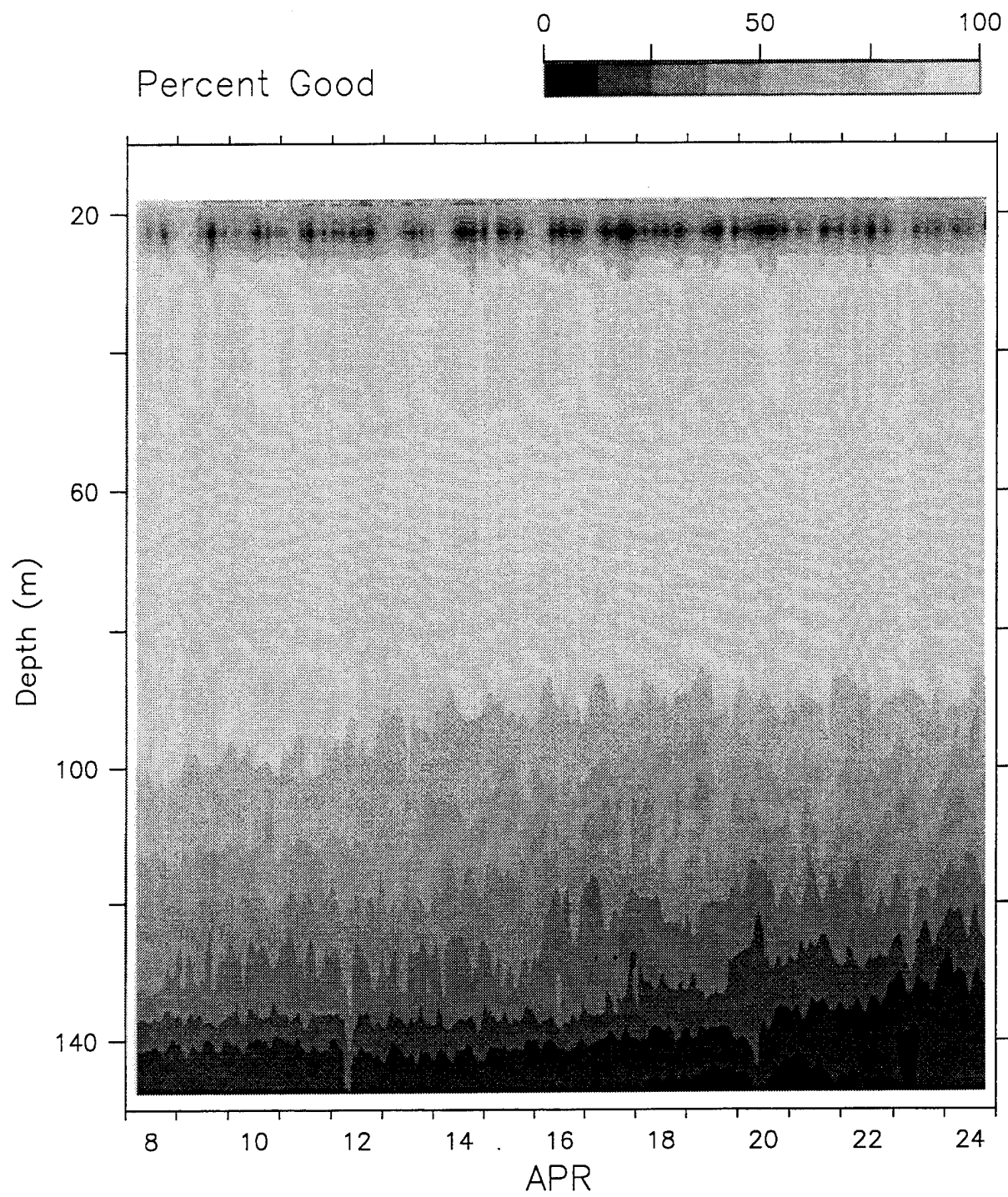


Figure 18: Time-depth contours of percent good: Beam 2.



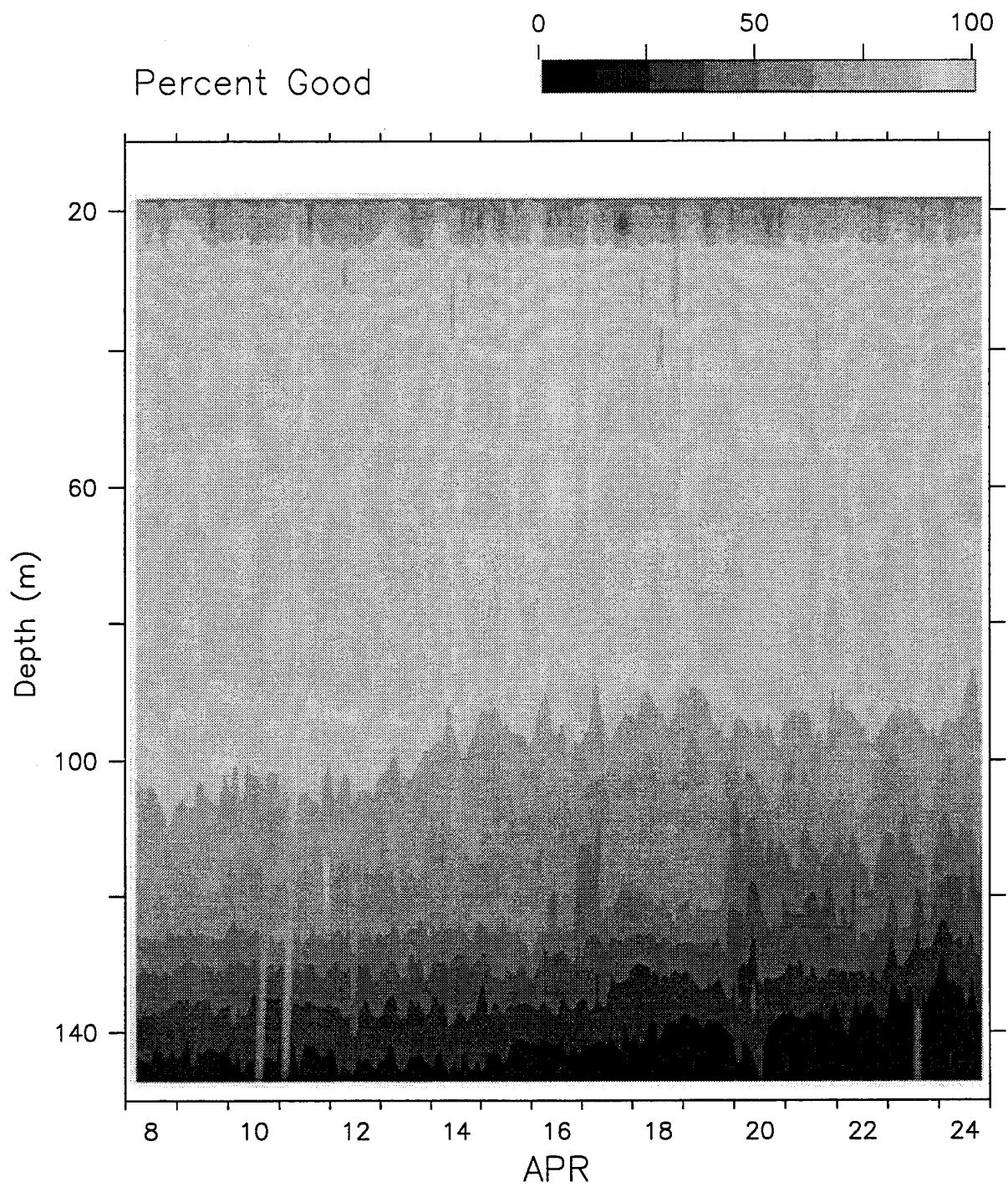


Figure 19: Time-depth contours of percent good: Beam 3.

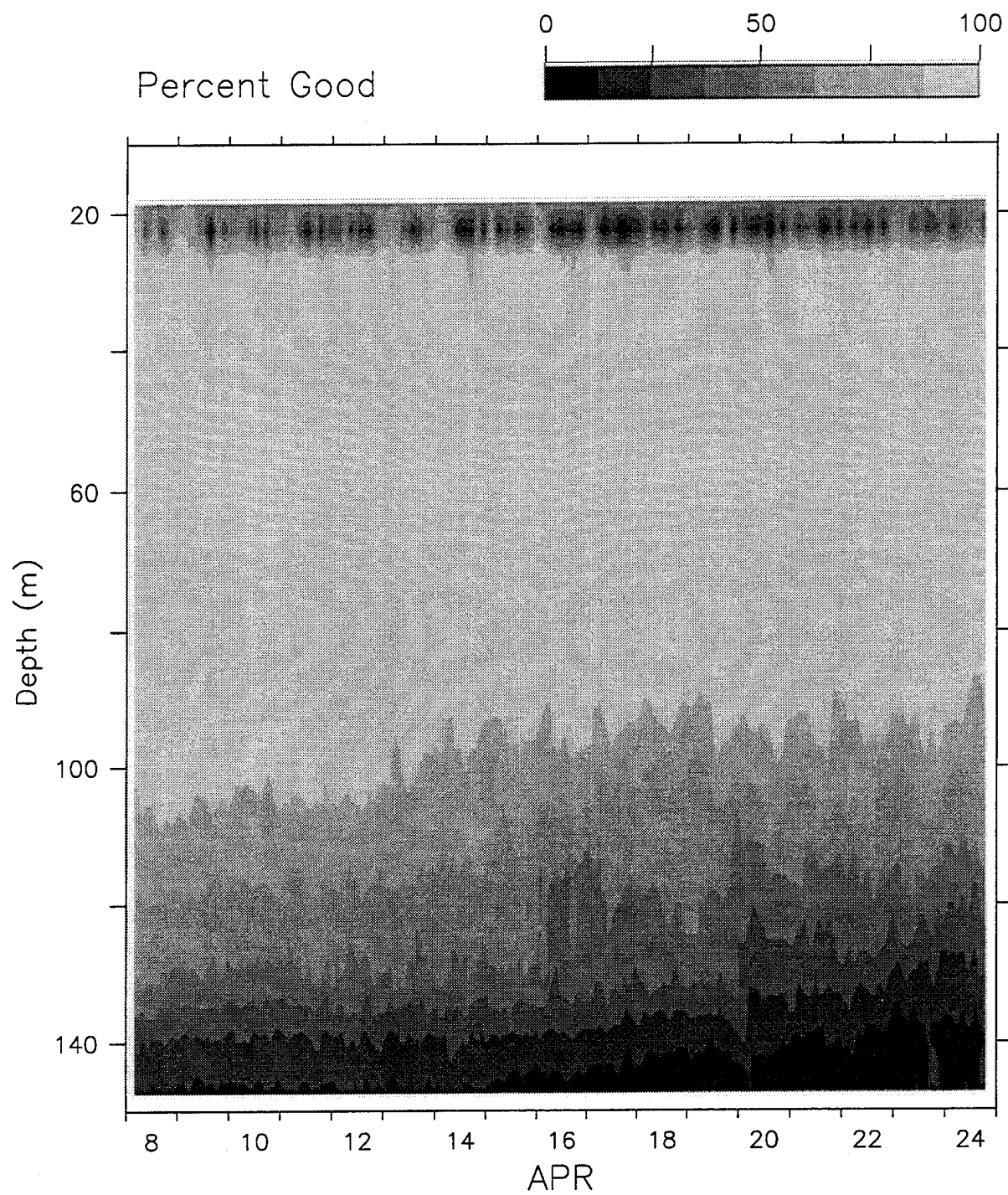


Figure 20: Time-depth contours of percent good: Beam 4.

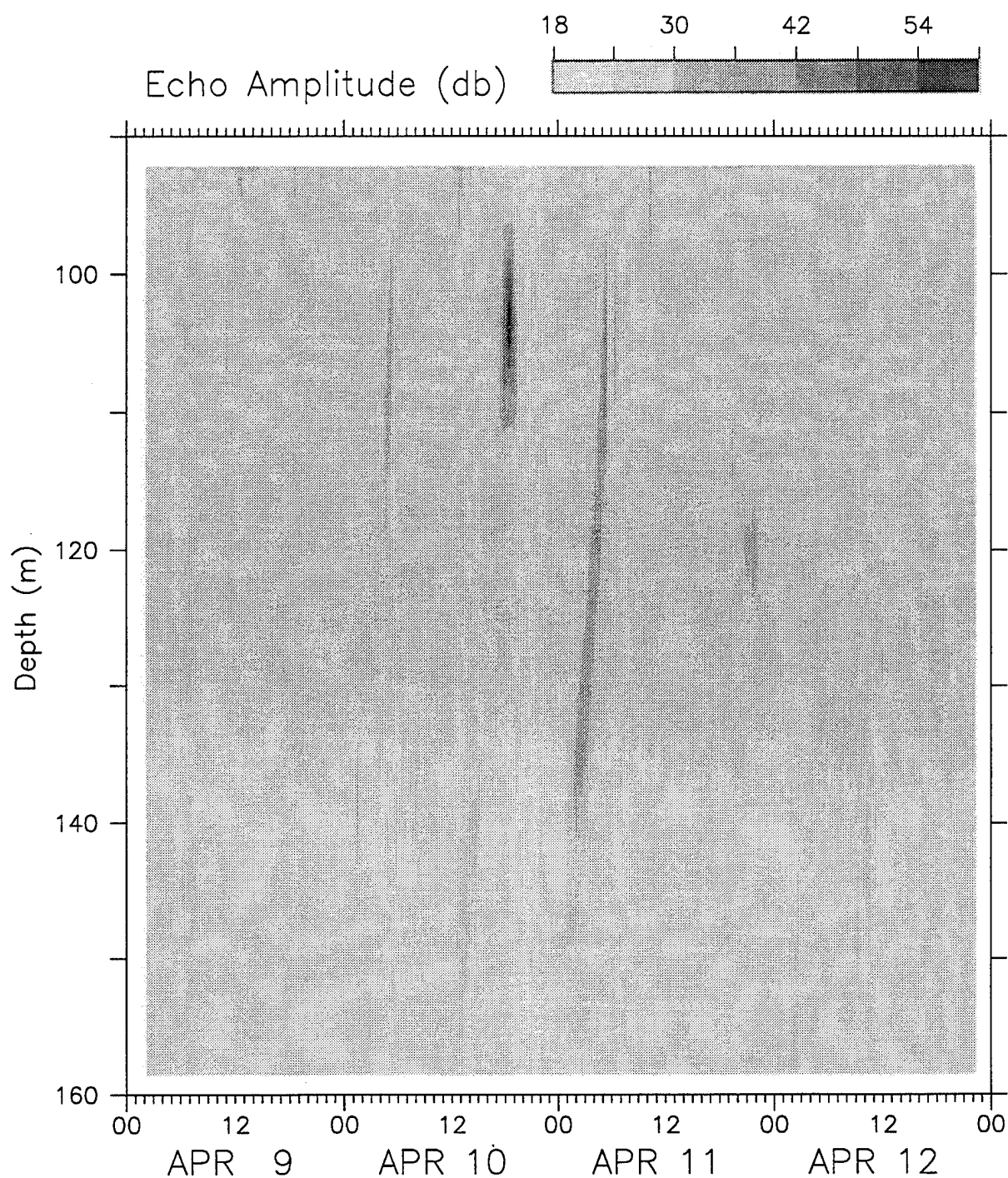


Figure 21: Time-depth contours of echo amplitude during 9-12 April: Beam 3. Depth cells from 20 (92.1 m) to 37 (158.5 m) are contoured from the 5 min ensemble data. The expanded scale highlights the period when an object was detected in the beam.

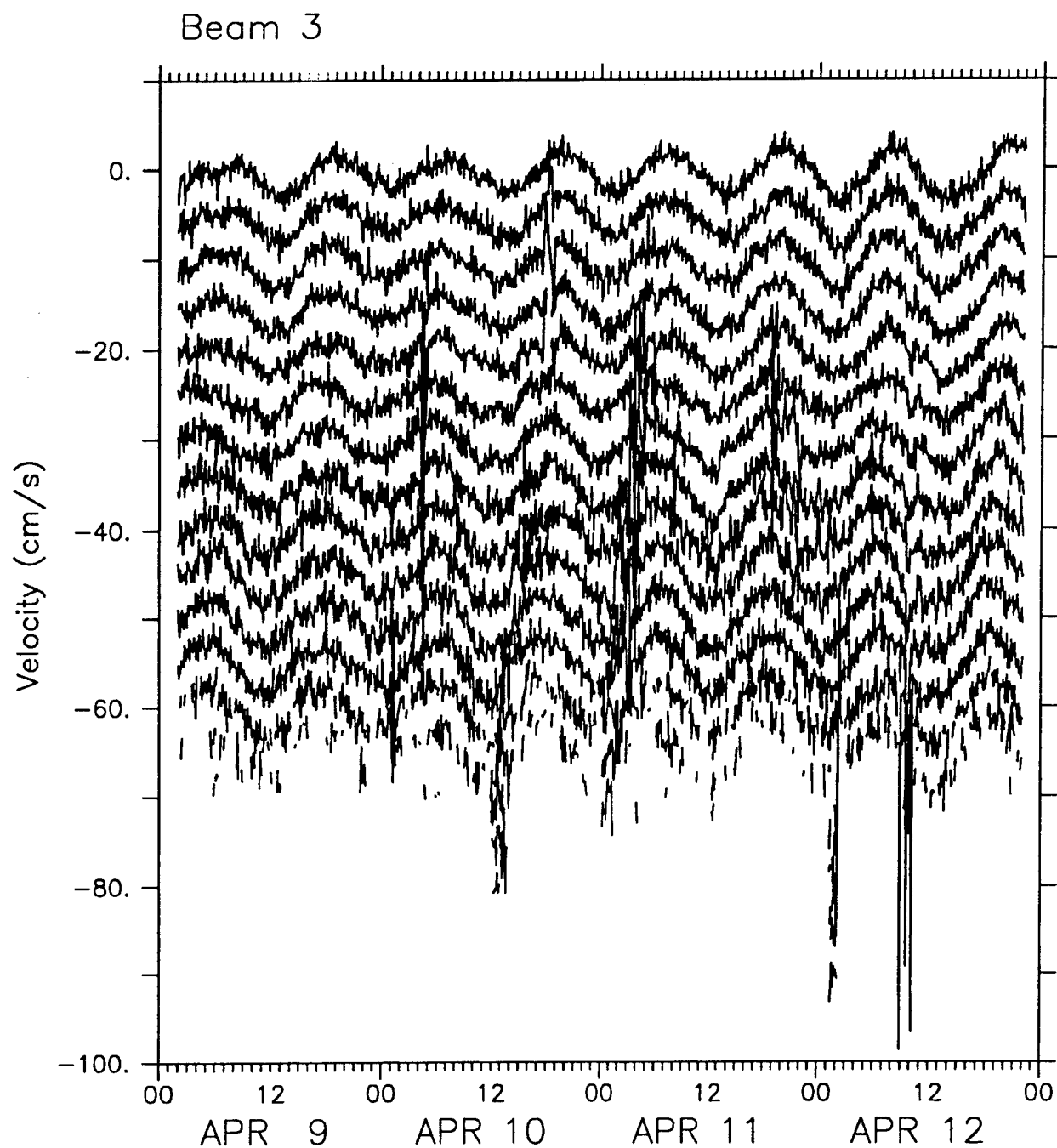


Figure 22: Time series of radial velocity during 9–12 April: Beam 3. Depth cells from 20 (92.1 m) to 37 (158.5 m) are plotted from the 5 min ensemble data. Successive depths are offset by  $-5 \text{ cm s}^{-1}$ .



## 2.4 Velocity in geographic coordinates

The estimation of geographic velocity components from the four radial velocities was not done on a pulse-by-pulse basis. Instead, the ensemble averaged values of instrument orientation were used to correct the averaged radial velocities for tilt and heading variation. This technique allowed evaluation of the quality of the orientation data and the velocities from each beam before performing the transformation into geographic coordinates. Both of these issues were important, as described below. In order for this technique to produce valid results the variability in instrument orientation during the ensemble must be small. It was assumed that the ice-anchored ADCP would be stable enough over the 1 min sample interval that the average instrument orientation could be used to correct the average velocities without introducing significant error. Results show that this was a good assumption since the standard deviations of tilt and heading within ensembles had typical values of only  $0.1^\circ$  and  $1^\circ$ , respectively (Figure 8).

The diurnal heading variability seen in Figure 7 was the result of variations in the horizontal magnetic field, and did not represent true rotation of the instrument (Sotirin and Newton, 1993). This was shown by comparing the actual ice camp rotation to the heading variation observed by a flux gate compass which was fixed relative to the camp. A theodolite was used to determine camp rotation by measuring the bearing of the sun relative to a reference flag located on the ice floe. The compass showed diurnal variability similar to that seen in Figure 7, but the camp bearing did not. In order to suppress the false heading variation, but preserve the true, low-frequency heading changes, a 24 hr running mean filter was applied to the ADCP heading before component velocities were computed (Figure 23).

Occasional outliers in the radial velocity data (see Figures 9–12) were eliminated by testing for cases where the difference in velocity between adjacent points was greater than  $5 \text{ cm s}^{-1}$ . This technique proved ineffective for beam 3 due to the nature of the contamination from the profiling instrument package (Figures 21–22). However, it was recognized that since beam 4 was uncontaminated, the sum of the beam 3 and beam 4 velocities (similar to the four-beam sum “error velocity” used by RD Instruments) would isolate the corrupted data. A velocity threshold of  $3 \text{ cm s}^{-1}$  applied to the two-beam sum provided a simple means to eliminate bad points in beam 3. Points rejected as a result of either the first-difference test or the threshold test were replaced by interpolated values.

The edited and interpolated beam velocities were used along with the instrument tilt records and the 24 hr filtered heading to compute the velocities in geographic coordinates (cf. Joyce *et al.*, 1982). A constant offset of  $-76.0$  degrees was applied to the heading to account for the magnetic variation at the site. As described above, the transient response at near-range and low signal-to-noise levels at far range limited

rec	depth (m)
1	27.7
2	35.5
3	43.2
4	51.1
5	58.9
6	66.7
7	74.5
8	82.3
9	90.1
10	98.0
11	105.8
12	113.6
13	121.4
14	129.2
15	137.0

Table 2: Depths for the fifteen, depth-averaged ADCP records. The ADCP was configured with a nominal depth cell length of 4 m and depth resolution of 8 m. Using the *in situ* soundspeed of  $1440 \text{ m s}^{-1}$ , the actual depth cell length was 3.9 m, and the depth resolution was 7.8 m. Depth cells 3–32 were averaged in pairs, matching the depth cell length to the vertical resolution and giving fifteen 7.8 m depth cells between 27.7 and 137.0 m depth.

the usable depth cells. Velocities from depth cells 3–32 were extracted and averaged in pairs (to match the depth cell length to the vertical resolution) giving a basic data set with fifteen 7.8 m depth cells between 27.7 and 137.0 m depth. Table 2 gives the depths for the resulting fifteen velocity records. Examination of horizontal velocity spectra (presented below) showed that the  $1 \text{ cm s}^{-1}$  noise threshold was reached at a frequency of about 1 cph. To suppress this noise, the velocity data were smoothed in time over 1 hr and sub-sampled at 15 min intervals.

Figures 24 and 25 present the horizontal velocity components as time series for each of the fifteen averaged depths. Figures 26–29 show the same data as time–depth contour plots. The records are dominated by oscillations with period near twelve hours and maximum amplitudes about midway through the profiling range. The semi-diurnal tidal frequency ( $M_2 = 0.0805 \text{ cph}$ ) cannot be distinguished from the local inertial frequency ( $f = 0.0829 \text{ cph}$ ) in these records. Henceforth these are referred to as “semi-diurnal oscillations”. A clear change in character can be seen near

50 m depth as relatively weak velocities in the mixed layer give way to the stronger, oscillatory flow in the upper pycnocline. This transition is particularly sharp in the north component, as can be seen by comparing the third record in the time series plot (43.3 m depth, just above the mixed layer base) with the fourth (51.1 m, just below the mixed layer). The semi-diurnal oscillations show a peak in energy during 14–16 April and decay after 21 April. Diurnal oscillations are evident starting on 19 April. The effect of ice motion can be seen as depth-independent offsets in the relative velocities between 19 and 22 April. The effect is the most noticeable in the east component.

Maximum component amplitudes were found between 75 and 90 m depth, and had values of 8 to 10  $\text{cm s}^{-1}$ . The maximum speed was 13.3  $\text{cm s}^{-1}$  from the record at 82.3 m depth. The 17 day mean velocities were to the S-SE at all depths. Mean speeds were largest for the uppermost record (2  $\text{cm s}^{-1}$  at 27.7 m depth) and nearly constant at 1.4  $\text{cm s}^{-1}$  below. The standard deviations of the 1 hr average velocities were smallest (1.5 to 2  $\text{cm s}^{-1}$ ) in the mixed layer. The largest standard deviations (3 to 4  $\text{cm s}^{-1}$ ) were found between 50 and 110 m depth, roughly corresponding to the extent of the sub-surface temperature maximum seen in the CTD profiles (Figure 3). Below 110 m the standard deviations dropped to intermediate values (2.5 to 3  $\text{cm s}^{-1}$ ).

Figure 30 shows the vertical velocity which results from processing the four beams of ADCP data. The vertical velocity variance was smallest at mid depth and increased for both shallower and deeper depths. The standard deviation of the 1 hr average velocity shown in the figure was near 0.1  $\text{cm s}^{-1}$  from 51.1 to 113.6 m, increasing to 0.2  $\text{cm s}^{-1}$  above and below. The records have the character of “white” noise and it is concluded that no geophysically meaningful vertical velocities have been detected above the instrument noise floor. However, the observed velocities are still of interest for assessment of instrument performance. Assuming the observed vertical velocities to be dominated by instrument noise, the standard deviation from the 5 min ensemble data can be used to estimate horizontal velocity precision. The standard deviation of the 5 min vertical velocities (not shown) was near 0.4  $\text{cm s}^{-1}$  at mid depth, increasing to almost 0.6  $\text{cm s}^{-1}$  above and below. Note that the vertical velocity is computed from all four beams, and the horizontal velocities from only two. Accounting for this, and the factor of  $\tan(\theta)$  (where  $\theta$  is the beam angle) between horizontal and vertical velocity estimates, the equivalent horizontal velocity precision would be 1.4  $\text{cm s}^{-1}$  at mid depth.

Figure 31 shows the “error velocity”, which provides a useful consistency check on the four beam horizontal velocity estimates (RD Instruments, 1989). The error velocity is essentially the difference between two estimates of vertical velocity. The vertical velocity in Figure 30 was computed from all four beams, but it is possible to make two separate vertical velocity estimates, one from each of the beam pairs

used to estimate the horizontal velocities. The difference between these two vertical velocities is reported as the error velocity. The lack of any distinct features in the 1 hr averaged error velocity above a noise floor of about  $0.1 \text{ cm s}^{-1}$  indicates that the horizontal velocity is of high quality.

Figures 32–34 show rotary spectra of horizontal velocity centered at depths of 35.5, 82.3, and 121.4 m. Spectra from all depths are combined in contour plots in Figures 35 and 36. All spectra are dominated by a peak at semi-diurnal frequency, with a smaller peak at diurnal frequency evident at most depths. Both diurnal and semi-diurnal peaks are largest in the clockwise rotating component. The strength of the diurnal peak increases noticeably at the mixed layer base and is relatively constant below. The semi-diurnal peak also increases below the mixed layer base, but grows to a maximum near 80 m depth and then gradually decays below. Low frequency ( $f < 0.03 \text{ cph}$ ) energy does not show substantial changes with depth. At high frequency ( $f > 1 \text{ cph}$ ) the spectra at mid-depth flatten out to a consistent level of about  $0.2 (\text{cm s}^{-1})^2 / \text{cph}$ . Shallower and deeper spectra are not as flat at high frequency, producing the “C” shaped contours seen in Figures 35 and 36. The mid-depth spectra were used to estimate horizontal velocity precision by assuming that the level where the spectra flattened out at high frequency was the “white” noise level of the measurements. This resulted in an estimated velocity standard deviation of  $1.1 \text{ cm s}^{-1}$ , in reasonable agreement with the precision of  $1.4 \text{ cm s}^{-1}$  estimated from the vertical velocity at mid depth.

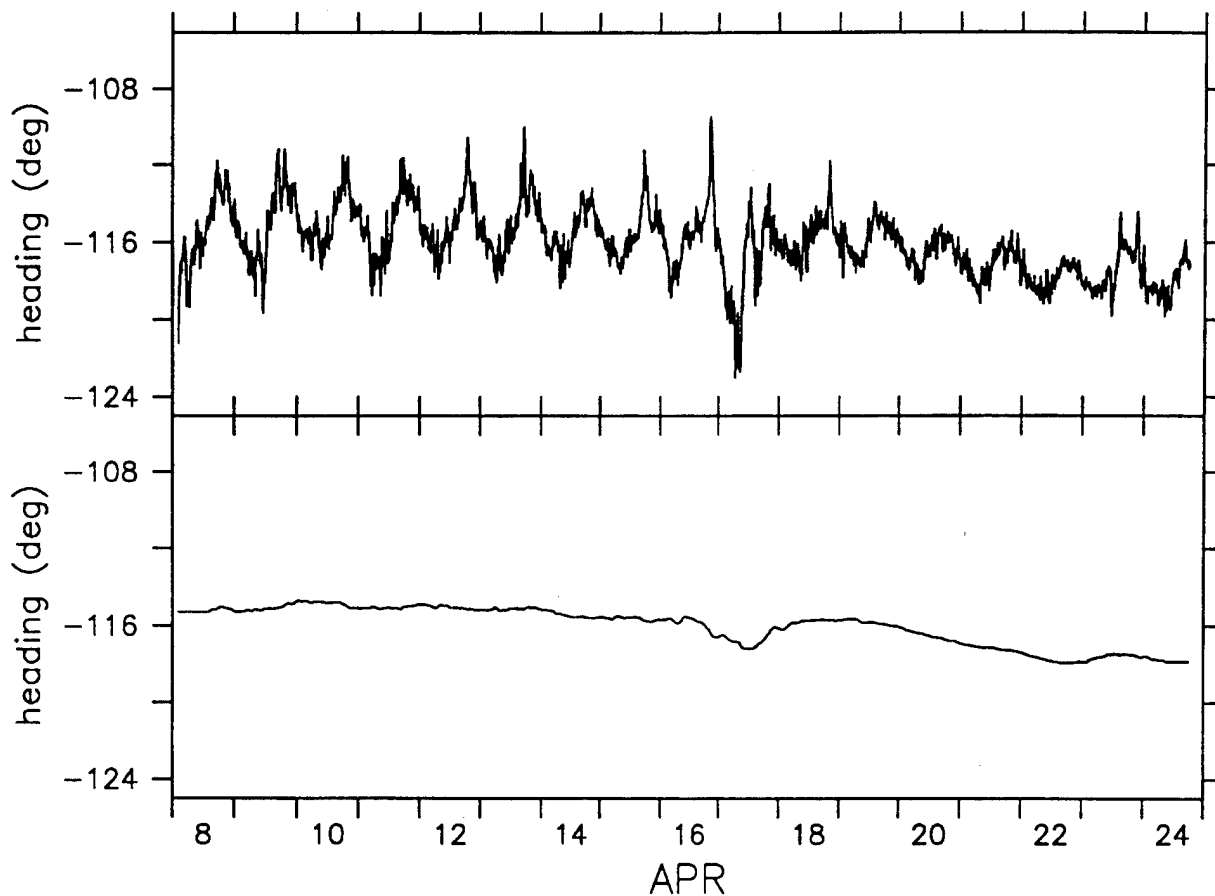


Figure 23: Time series of “raw” (5 min sample interval) ADCP compass heading (upper panel) compared to the same data after smoothing with a 24 hr filter (lower). The filtering was necessary to suppress false heading oscillations resulting from variations in the magnetic field.

## East Velocity

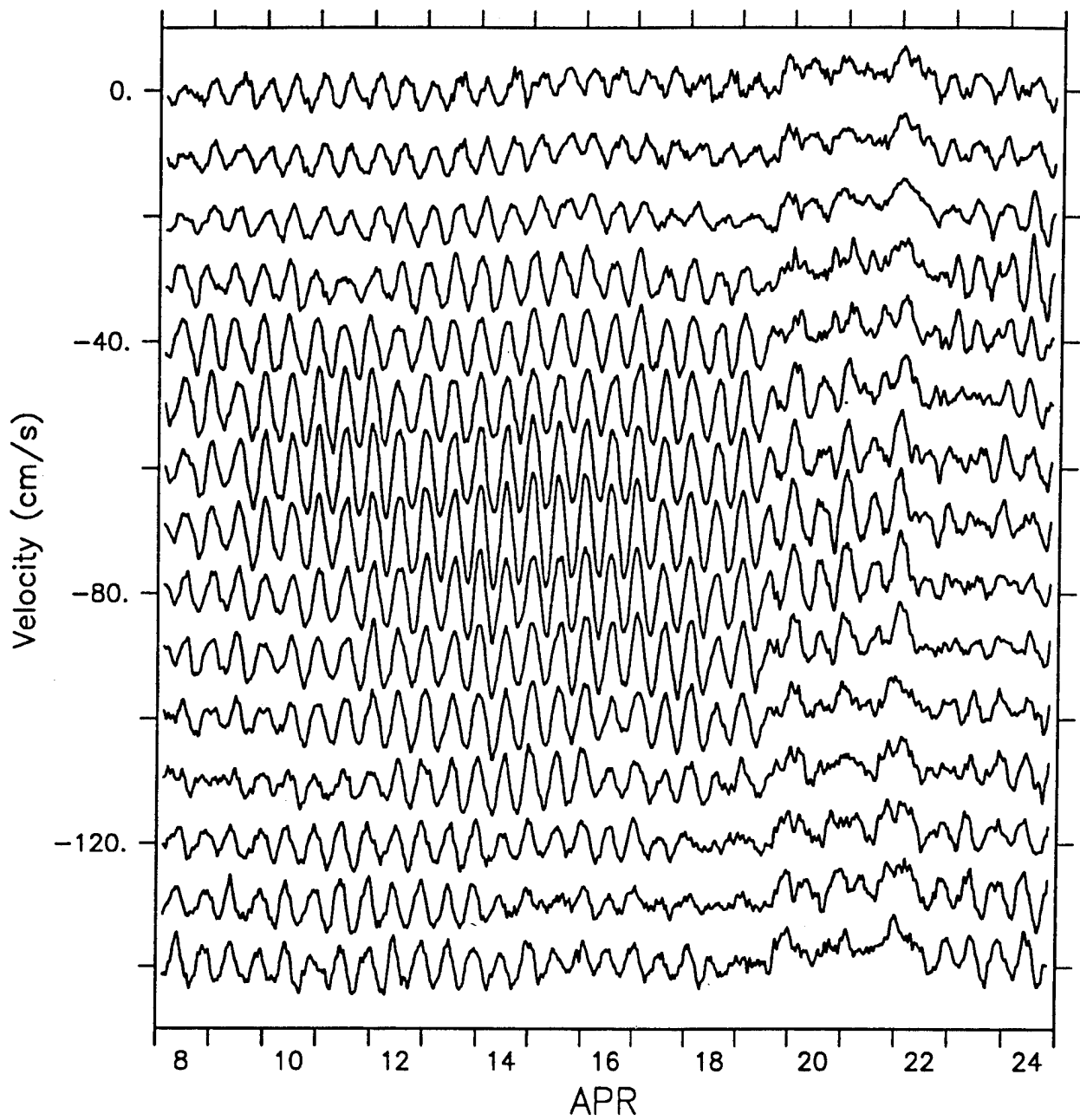


Figure 24: Time series of East velocity. Data from depth cells 3 to 32 were smoothed over 12 ensembles (1 hr) in time and averaged over 2 cells (7.8 m) in depth. The resulting velocity time series for 15 depths (27.7 to 137.0 m) are shown with successive depths offset by  $-10 \text{ cm s}^{-1}$ .

# North Velocity

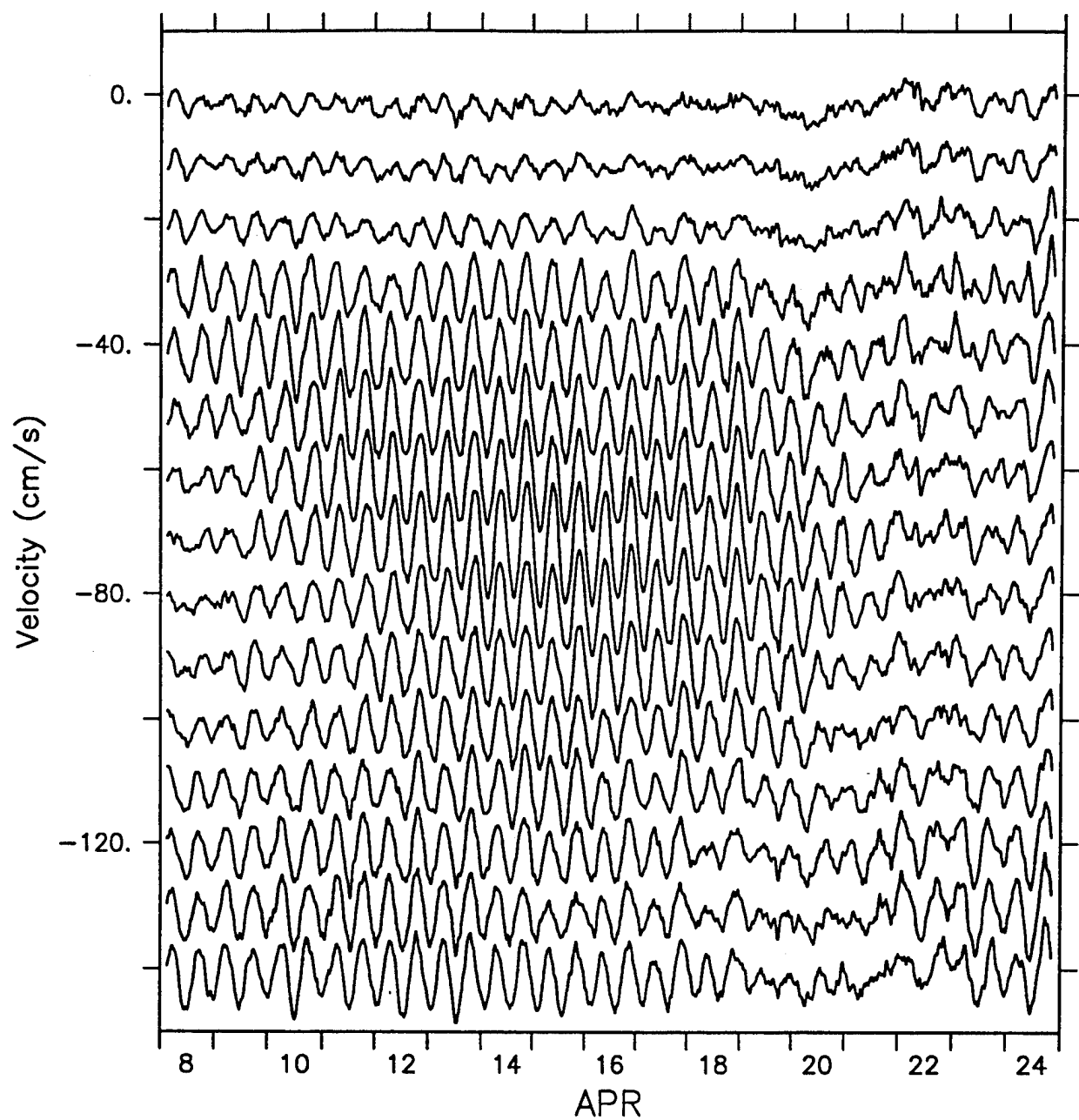


Figure 25: Time series of North velocity.

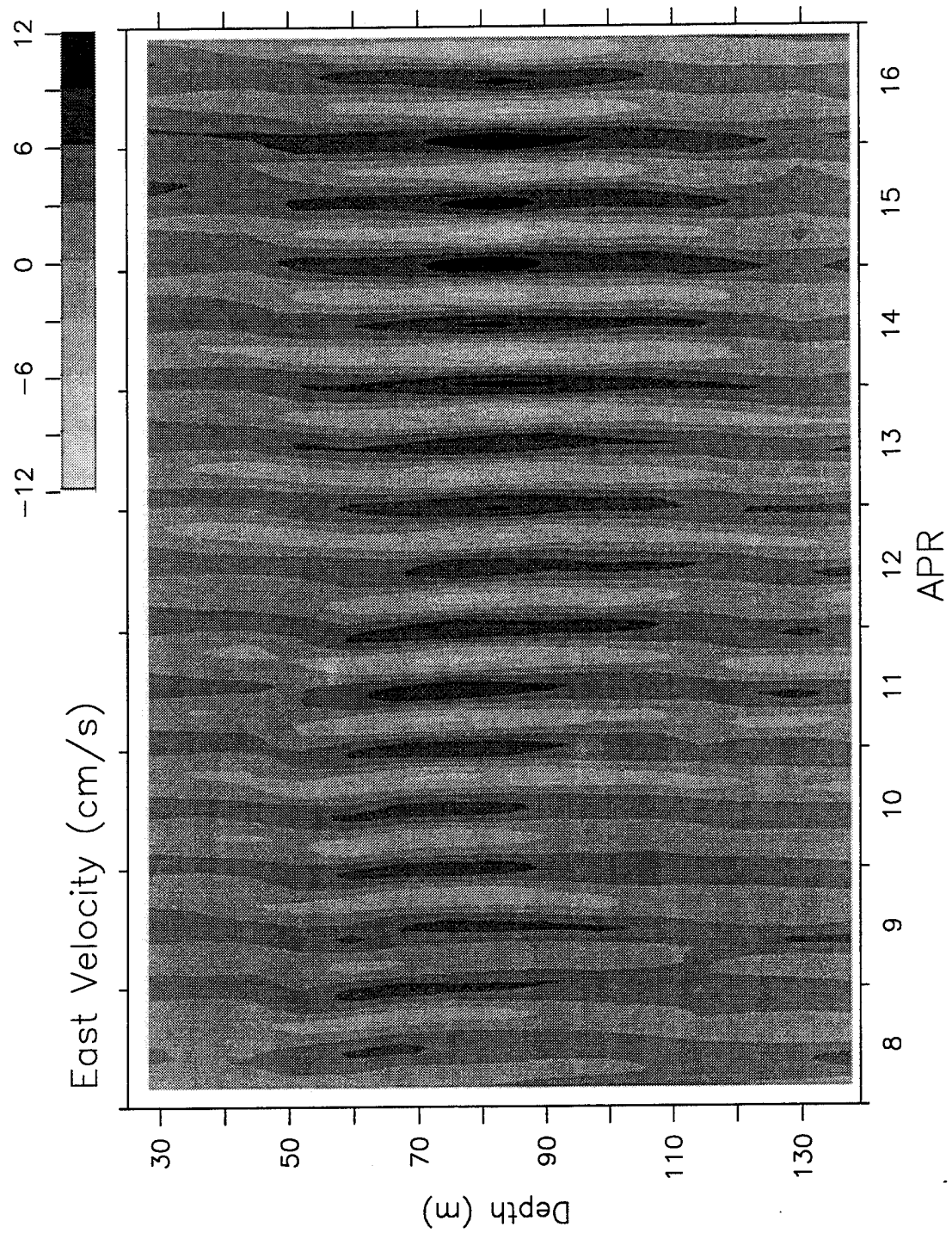


Figure 26: Contours of East velocity for 8–16 April. The 1 hr, 2 depth cell averaged time series were smoothed over 3 hr and contoured.



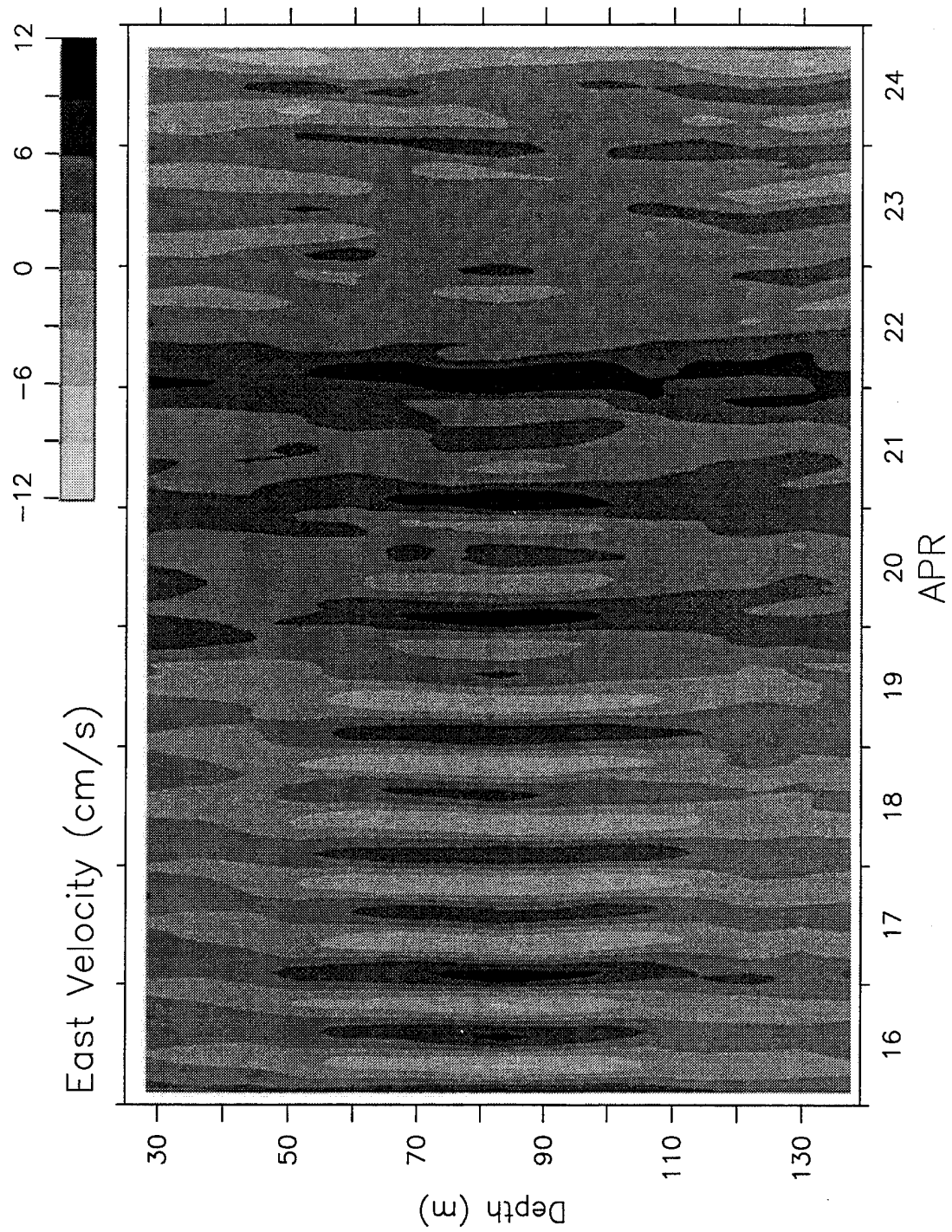


Figure 27: Contours of East velocity for 16–24 April.

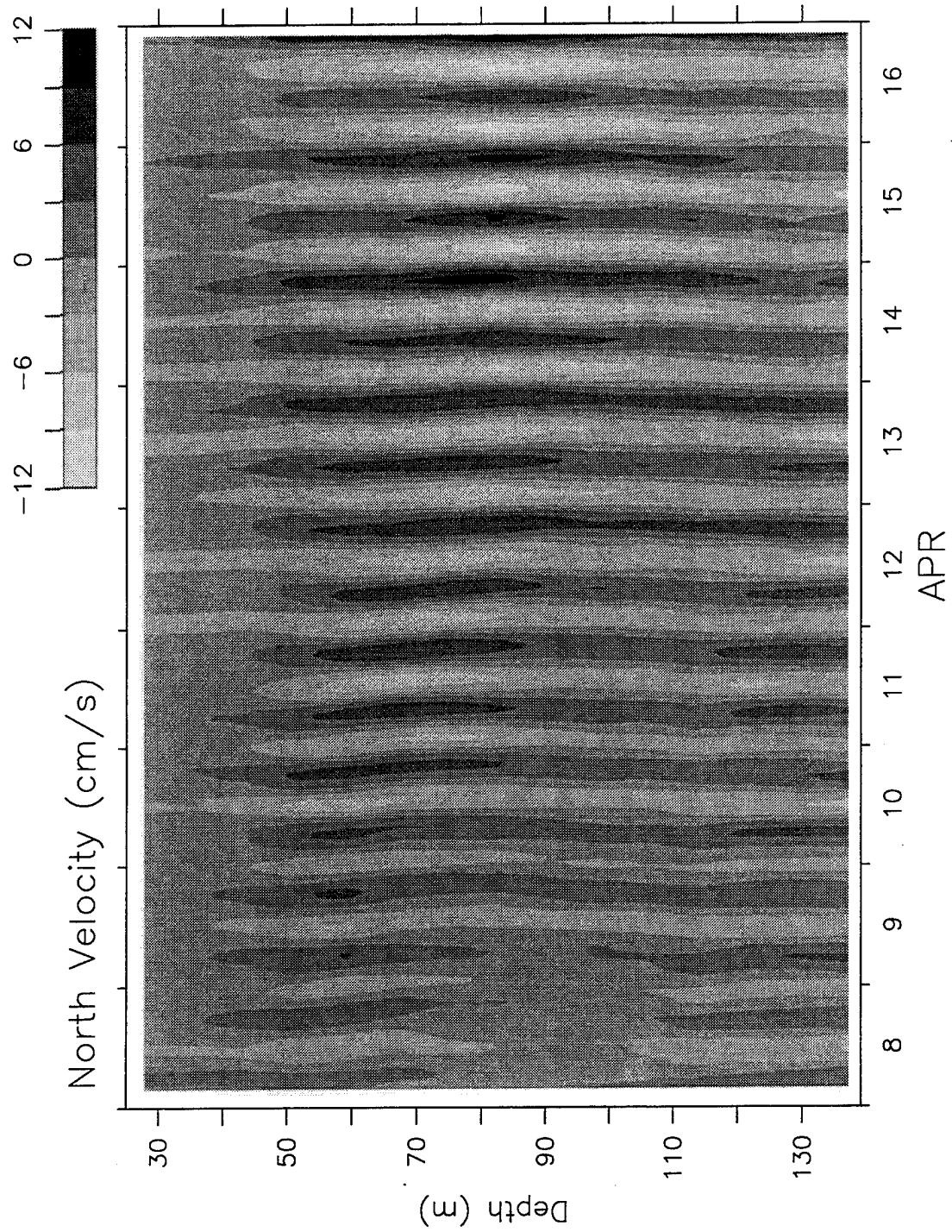


Figure 28: Contours of North velocity for 8–16 April. The 1 hr, 2 depth cell averaged time series were smoothed over 3 hr and contoured.

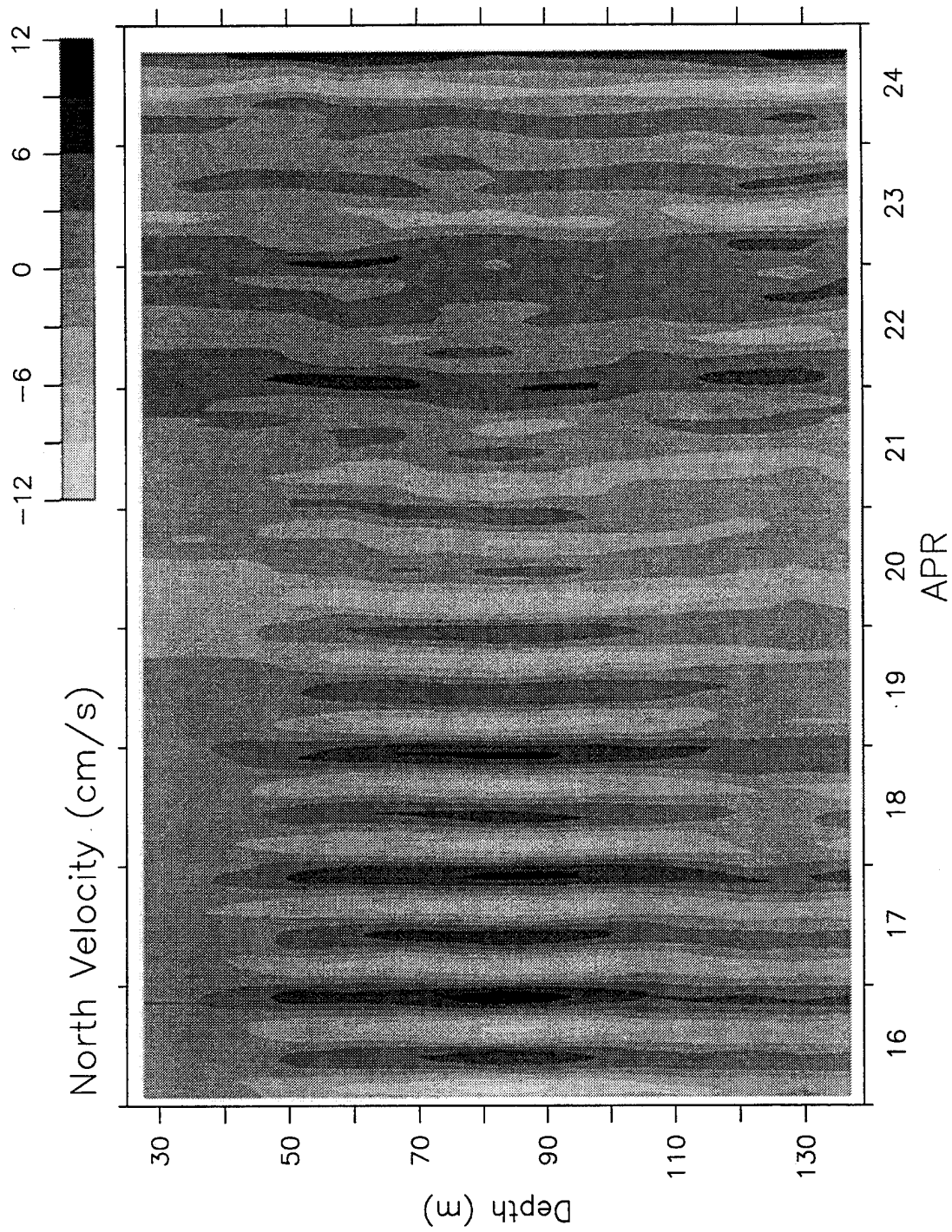


Figure 29: Contours of North velocity for 16–24 April.

# Vertical Velocity

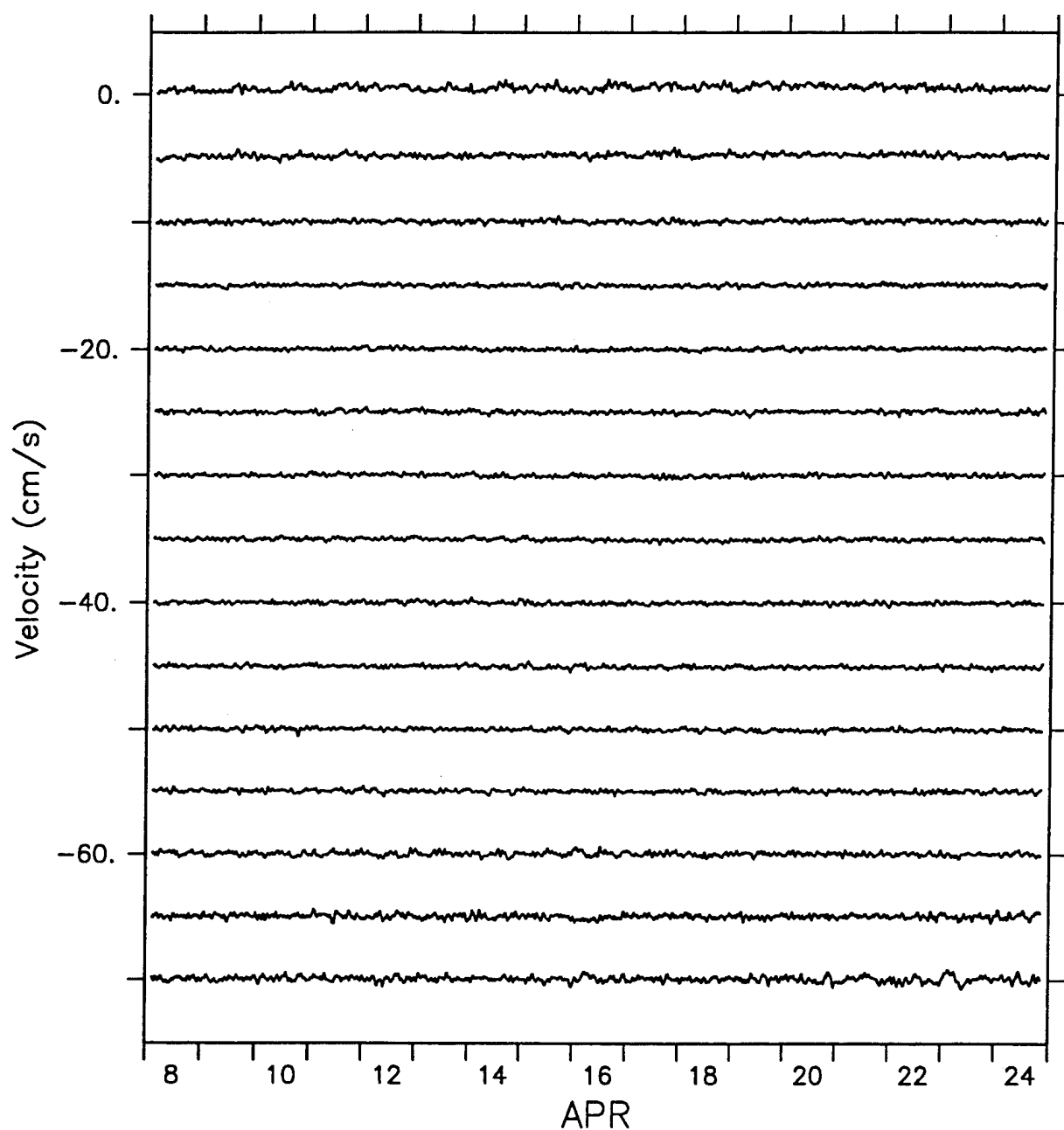


Figure 30: Time series of vertical velocity. Data from depth cells 3 to 32 were smoothed over 12 ensembles (1 hr) in time and averaged over 2 cells (7.8 m) in depth. The resulting velocity time series for 15 depths (27.7 to 137.0 m) are shown with successive depths offset by  $-5 \text{ cm s}^{-1}$ .

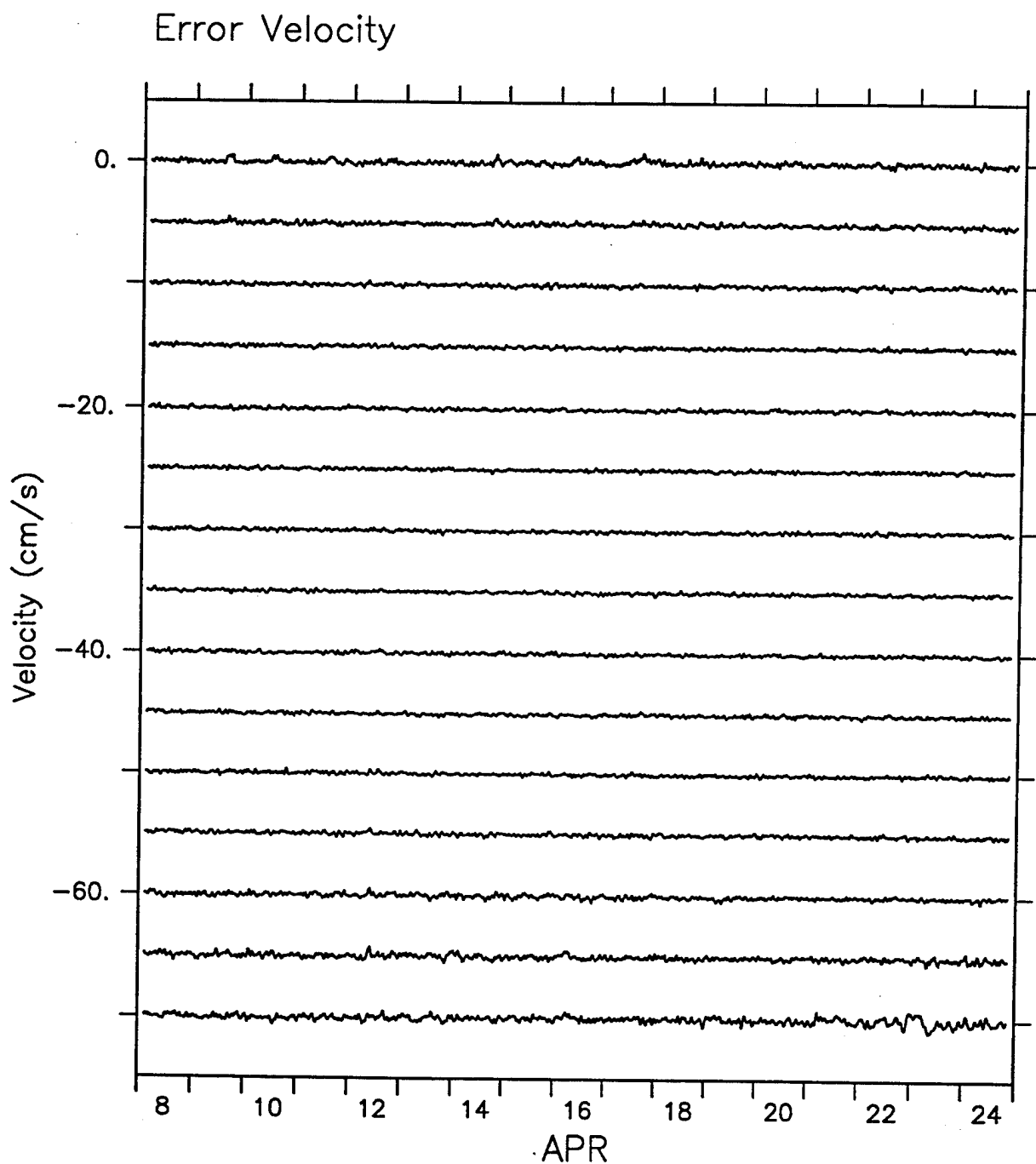


Figure 31: Time series of error velocity. Data from depth cells 3 to 32 were smoothed over 12 ensembles (1 hr) in time and averaged over 2 cells (7.8 m) in depth. The resulting velocity time series for 15 depths (27.7 to 137.0 m) are shown with successive depths offset by  $-5 \text{ cm s}^{-1}$ .

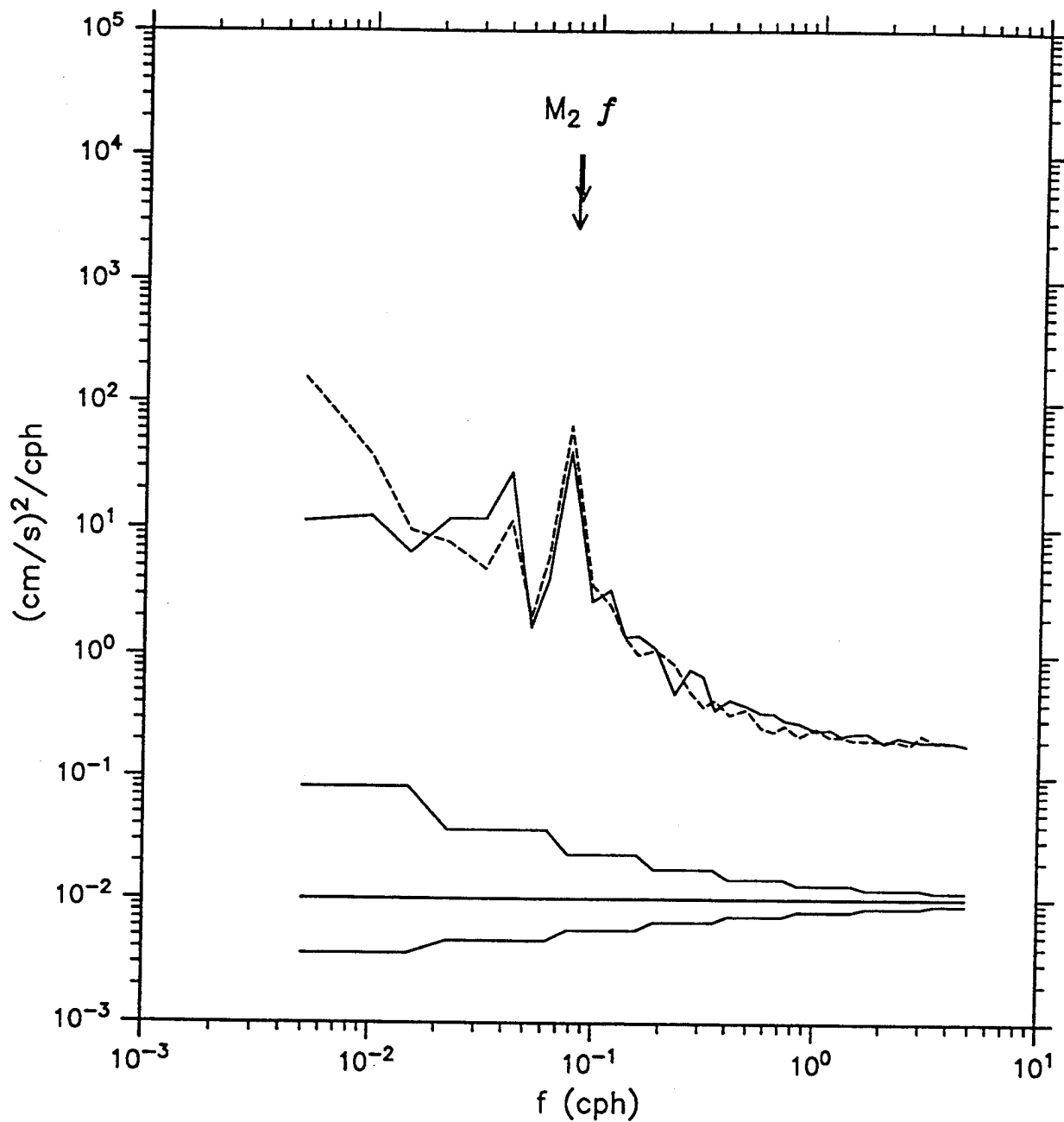


Figure 32: Rotary spectra at 35.5 m depth. Spectral estimates from depth cells 5-6 were averaged to form the average clockwise (solid) and anti-clockwise (dashed) rotary spectra. The semi-diurnal tidal frequency ( $M_2 = 0.0805$  cph, long arrow) and local inertial frequency ( $f = 0.0829$  cph, short arrow) are marked for reference.

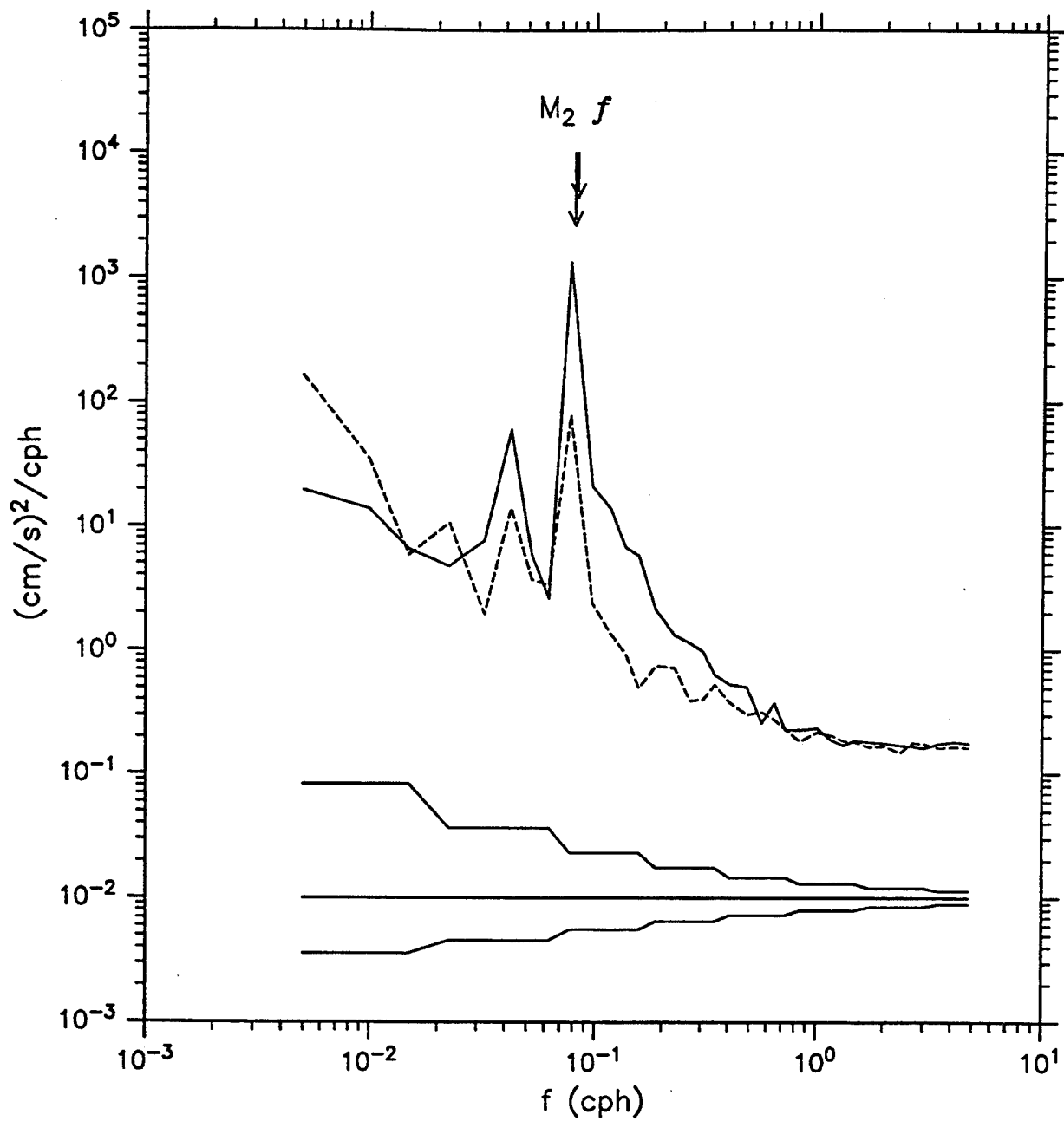


Figure 33: Rotary spectra at 82.3 m depth. Spectral estimates from depth cells 15-16 were averaged to form the average clockwise (solid) and anti-clockwise (dashed) rotary spectra.

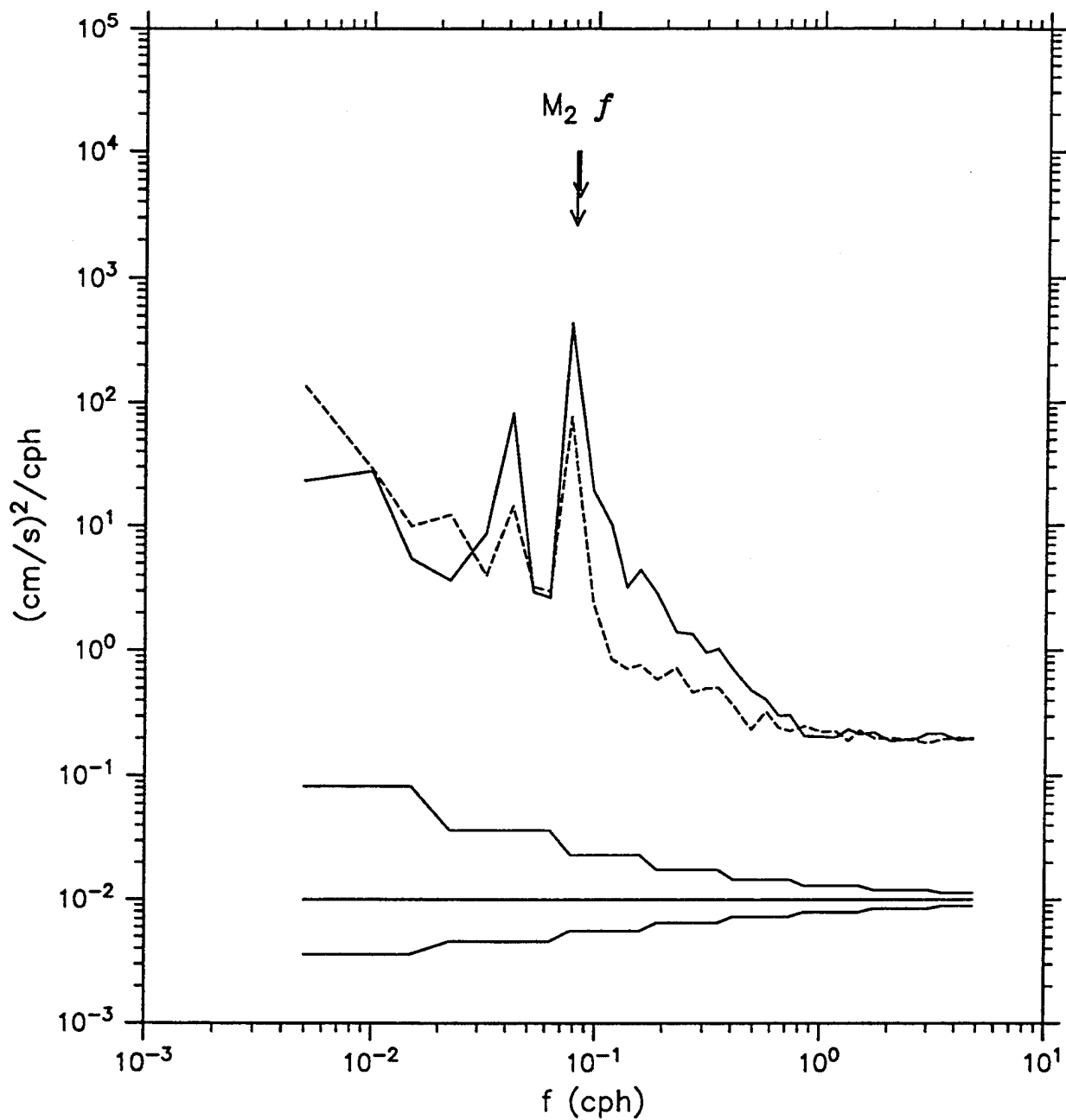


Figure 34: Rotary spectra at 121.4 m depth. Spectral estimates from depth cells 25–26 were averaged to form the average clockwise (solid) and anti-clockwise (dashed) rotary spectra.



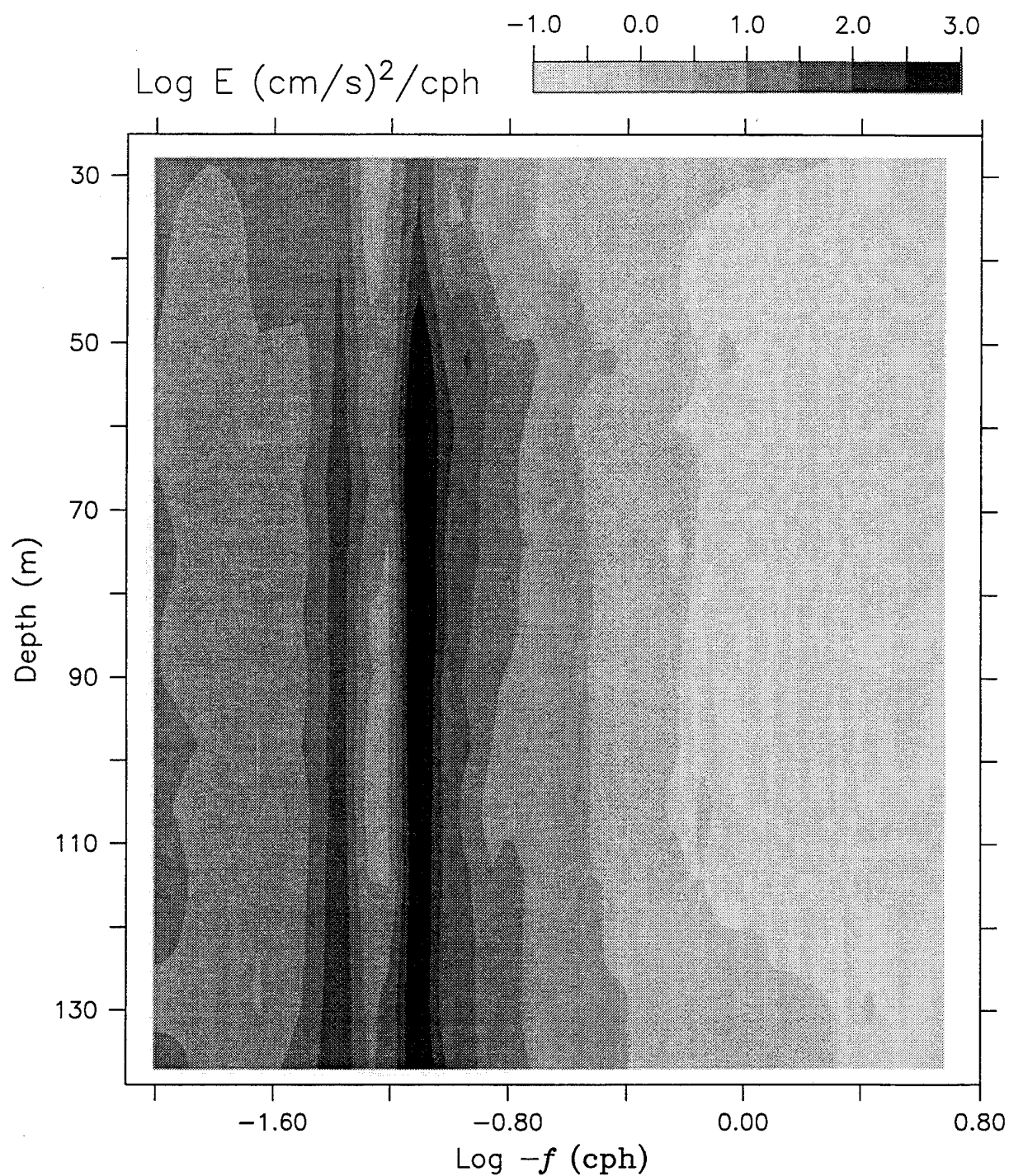


Figure 35: Contours of rotary spectra vs. depth for clockwise rotation. Spectral estimates from depth cells 3-32 were averaged in pairs and contoured. The log of spectral energy density is shown vs. log frequency and depth.

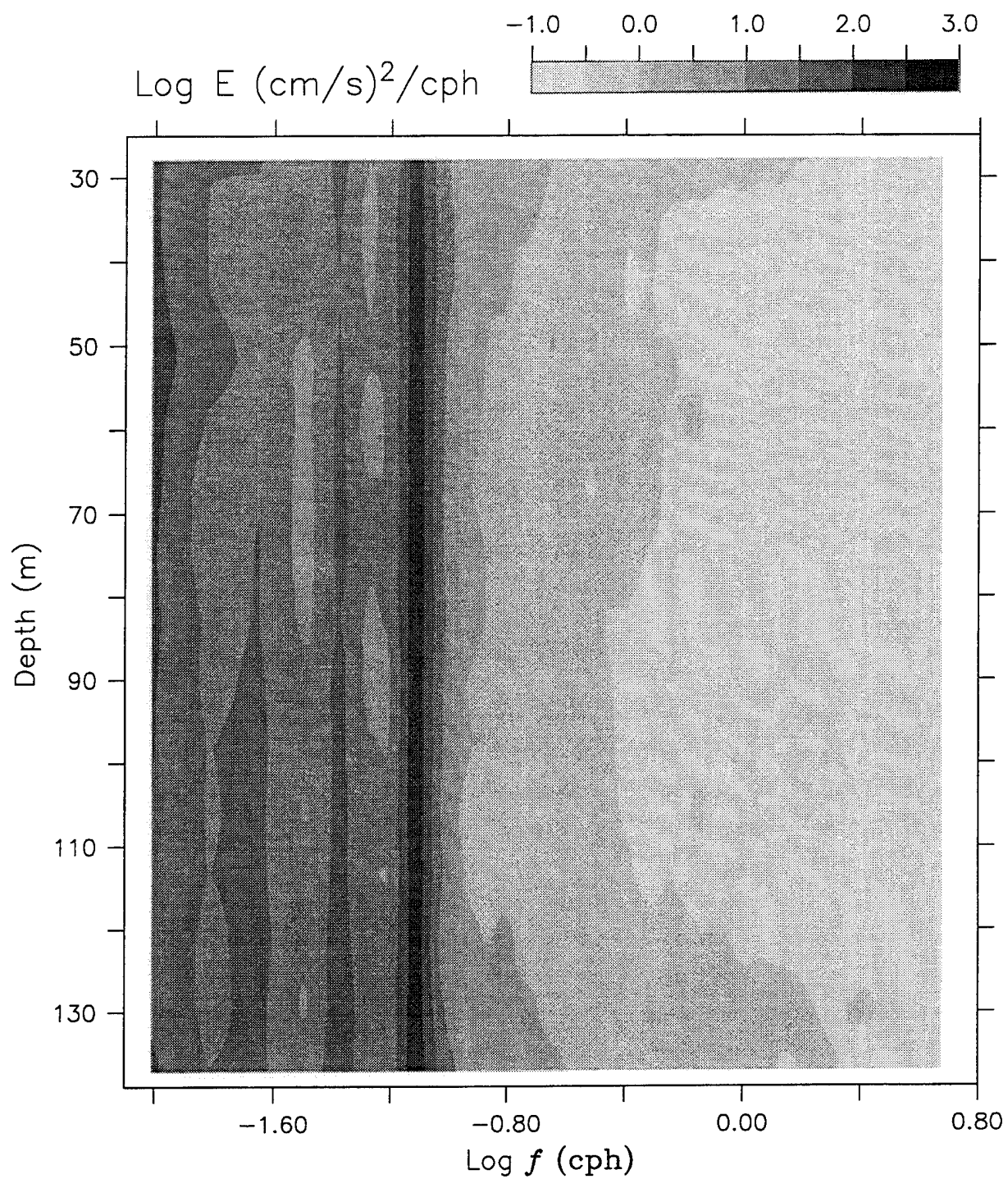


Figure 36: Contours of rotary spectra vs. depth for anti-clockwise rotation. Spectral estimates from depth cells 3-32 were averaged in pairs and contoured. The log of spectral energy density is shown vs. log frequency and depth.

### 3 ADCP – S4 Comparisons

An InterOcean S4 electromagnetic current meter was deployed at the ice camp between 10 and 24 April. The basic measurements were current speed, current direction, and depth. Measurements were made in both "time series" and "profile" modes. Time series measurements were obtained by lowering the current meter to a fixed depth and leaving it in place for several hours. Profiles were obtained by raising and lowering the instrument at a constant, slow rate. During some raisings the instrument was stopped for a few minutes at several depths. Only the lowerings with nearly constant speed and no stops were used in the comparison study. Different sampling schemes were used for the time series and profile data. During time series deployments, 1 min average data were recorded every 5 min. During profiling, continuous 10 second averages were recorded. A total of 13 time series and 16 profiles were extracted for use in the comparison study.

The S4 time series were obtained at three nominal depths – 75, 100, 300, and 400 m. The 300 and 400 m S4 data were outside of the depth interval observed by the ADCP (Table 2) and could not be used in the comparison. Data from 3 time series at 75 m depth and 3 time series at 105 m depth were processed together to generate the comparison statistics. The combined records span about 36 hr for each depth, but they are discontinuous because the time series were periodically interrupted by the collection of profile data. Spectra of the S4 time series indicated a lower noise floor, and hence greater velocity precision (about  $0.25 \text{ cm s}^{-1}$ ) than the ADCP. However, since the ADCP data were dominated by noise for  $f > 1 \text{ cph}$ , the comparisons were done with both data sets smoothed over 1 hr. Speed and direction were converted to horizontal velocity components, corrected for magnetic variation, smoothed over 1 hr, and sub-sampled at 15 min intervals matching the ADCP time base. No attempt was made to account for diurnal oscillations which may have been present in the S4 compass data.

Figures 37–40 show the time series comparisons at 75 m depth, and Figures 41–44 show the comparisons at 105 m depth. The speed comparison at 75 m depth shows the S4 consistently under-speeding relative to the ADCP. The component velocity differences were largest at the peaks of the semi-diurnal oscillations. The resulting semi-diurnal oscillations in the velocity differences are of about the same amplitude in both components. The direction difference shows considerable scatter, but no significant mean difference. The speed comparison at 105 m also shows under-speeding by the S4, but to a lesser degree than at 75 m. The largest differences are confined to the 15 April S4 deployment, where one of the few periods where the S4 significantly over-speeds relative to the ADCP is also found. Directional differences show more scatter at 105 m than at 75 m. However, directional differences tend to be largest at low speeds, and the 105 m record is characterized by lower speeds than at 75 m.

Figures 45–48 show the speed and direction comparisons as scatter plots. The scatter plot of speed at 75 m shows a reasonably linear slope for speeds below  $7 \text{ cm s}^{-1}$ , but with a clear offset in the intercept as a result of the mean speed difference. The scatter increases at higher speed. The speed comparison at 105 m is also reasonably linear below  $7 \text{ cm s}^{-1}$ . This relationship breaks down at higher speeds where the S4 shows under-speeding similar to that seen at 75 m. The directional differences at 75 m are relatively constant with direction. At 105 m the directional differences are largest between 40 and  $170^\circ$ . This corresponds to the periods where speeds are near their minimum values.

The S4 profiles were done over the full water depth at the site, about 500 m. The lowering rate was about  $30 \text{ cm s}^{-1}$ , and a typical profile took 25–30 min to complete. The ten second samples in profiling mode corresponded to a depth resolution of about 3 m. The “mean time” of the S4 profile was taken to be the average time of all samples within the ADCP depth interval. Prior to comparison with the ADCP profiles, the S4 data were averaged over 3 points in depth and interpolated to the nominal ADCP depths (Table 2). The ADCP data used in the profile comparisons were averaged over two depth cells, but were still at the original 5 min ensemble sampling interval. The ADCP profile matching (within 5 min) the mean time of the S4 profile was identified, and this profile was then averaged with two adjacent profiles (one before and one after) to give a 15 min average ADCP profile with a mean time approximately matching that of the S4 profile.

Figures 49–64 show the 16 profile comparisons. Mean speed differences were largest ( $0.7$  to  $1.4 \text{ cm s}^{-1}$ ) between 43.2 and 82.3 m depth, dropping to  $0.5 \text{ cm s}^{-1}$  or less above and below. Mean differences were larger in the north component than in the east component. The largest mean difference ( $-1.3 \text{ cm s}^{-1}$ ) was seen at 74.5 m depth in the north component. The standard deviations of speed differences were between 1 and  $1.5 \text{ cm s}^{-1}$ , and showed no clear pattern with depth. As with the mean differences, the standard deviations of the differences were largest in the north component. The largest standard deviation ( $2.1 \text{ cm s}^{-1}$ ) was in the north component at 74.5 m depth. Mean direction differences varied from less than  $1^\circ$  to  $12^\circ$ . No distinct pattern of variation with depth was evident.

Table 3 summarizes the comparison statistics.

	md u	sdd u	md v	sdd v	md s	sdd s	md d
TS-075	-0.15	1.44	0.27	1.72	1.77	0.81	-0.5
TS-105	0.38	0.93	-0.15	1.18	0.46	0.72	6.4
PR-01	1.04	1.47	-0.64	0.88	0.15	1.46	-9.61
PR-02	0.78	1.13	-0.63	0.75	0.37	1.24	-9.64
PR-03	0.31	1.09	-0.66	1.03	0.66	1.11	-5.62
PR-04	0.69	1.28	-0.56	1.65	0.85	1.46	7.36
PR-05	0.54	1.26	0.06	1.75	1.20	1.46	1.36
PR-06	0.07	1.52	-0.38	0.96	0.81	0.63	-11.55
PR-07	0.30	2.12	-1.31	1.21	1.42	1.34	-12.05
PR-08	0.36	1.44	-0.82	1.65	1.12	1.58	-3.47
PR-09	0.12	0.98	-0.38	1.10	0.48	0.89	-6.05
PR-10	0.27	0.92	-0.21	1.16	0.35	1.15	-3.85
PR-11	0.09	0.95	0.30	1.06	-0.35	1.02	-2.41
PR-12	-0.30	1.19	-0.20	1.66	-0.32	1.55	5.92
PR-13	-0.32	0.72	0.51	1.37	-0.17	1.23	4.87
PR-14	-0.59	0.98	0.40	1.29	-0.54	1.12	-2.67
PR-15	-0.04	0.83	-0.87	1.16	-0.21	1.21	-0.14
PR-AVG	0.22	1.19	-0.36	1.25	0.39	1.23	-3.17

Table 3: Summary of ADCP – S4 comparison statistics. Mean differences (md) and standard deviation of differences (sdd) are shown for horizontal velocity components (u,v) and speed (s). The mean difference in direction (d) is also shown. The time series (TS) statistics come from all available data pairs at 75 and 105 m depth. The profile (PR) statistics are shown for the 15 ADCP depths (see Table 2). PR-AVG represents the depth average of values computed at each depth.

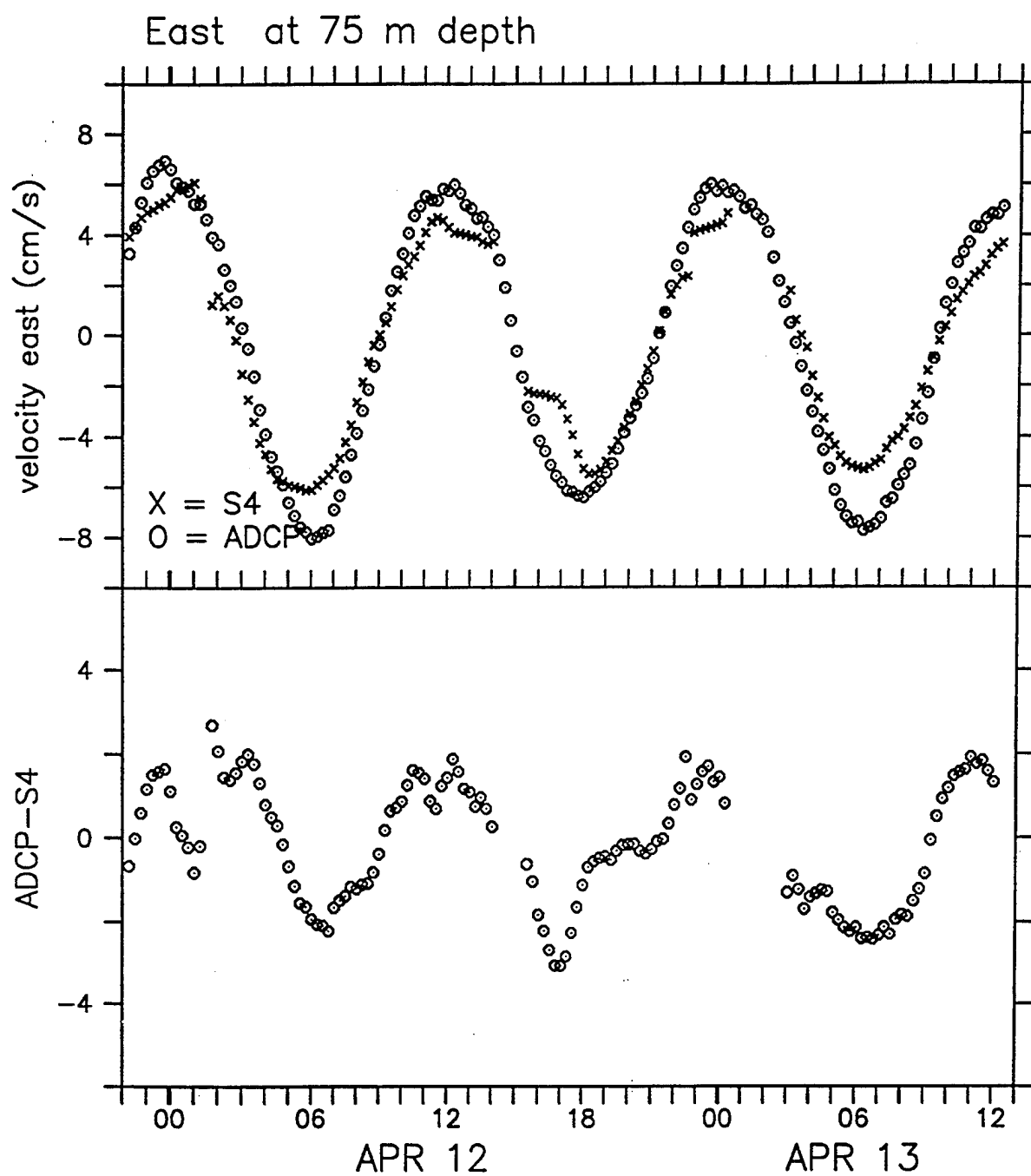


Figure 37: Time series of ADCP and S4 east velocities (upper panel) and ADCP - S4 velocity difference (lower panel) at 75 m depth.

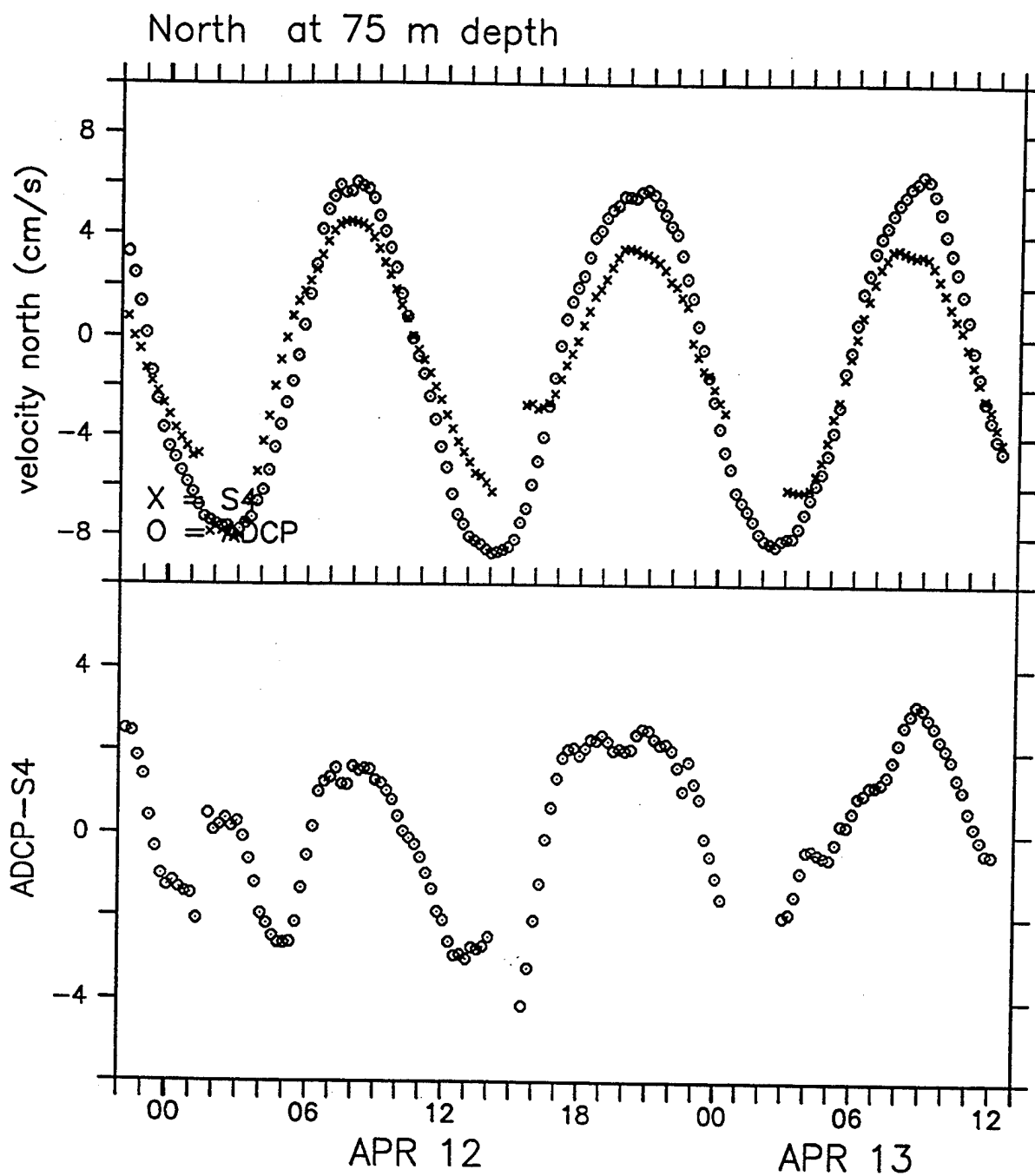


Figure 38: Time series of ADCP and S4 north velocities (upper panel) and ADCP - S4 velocity difference (lower panel) at 75 m depth.

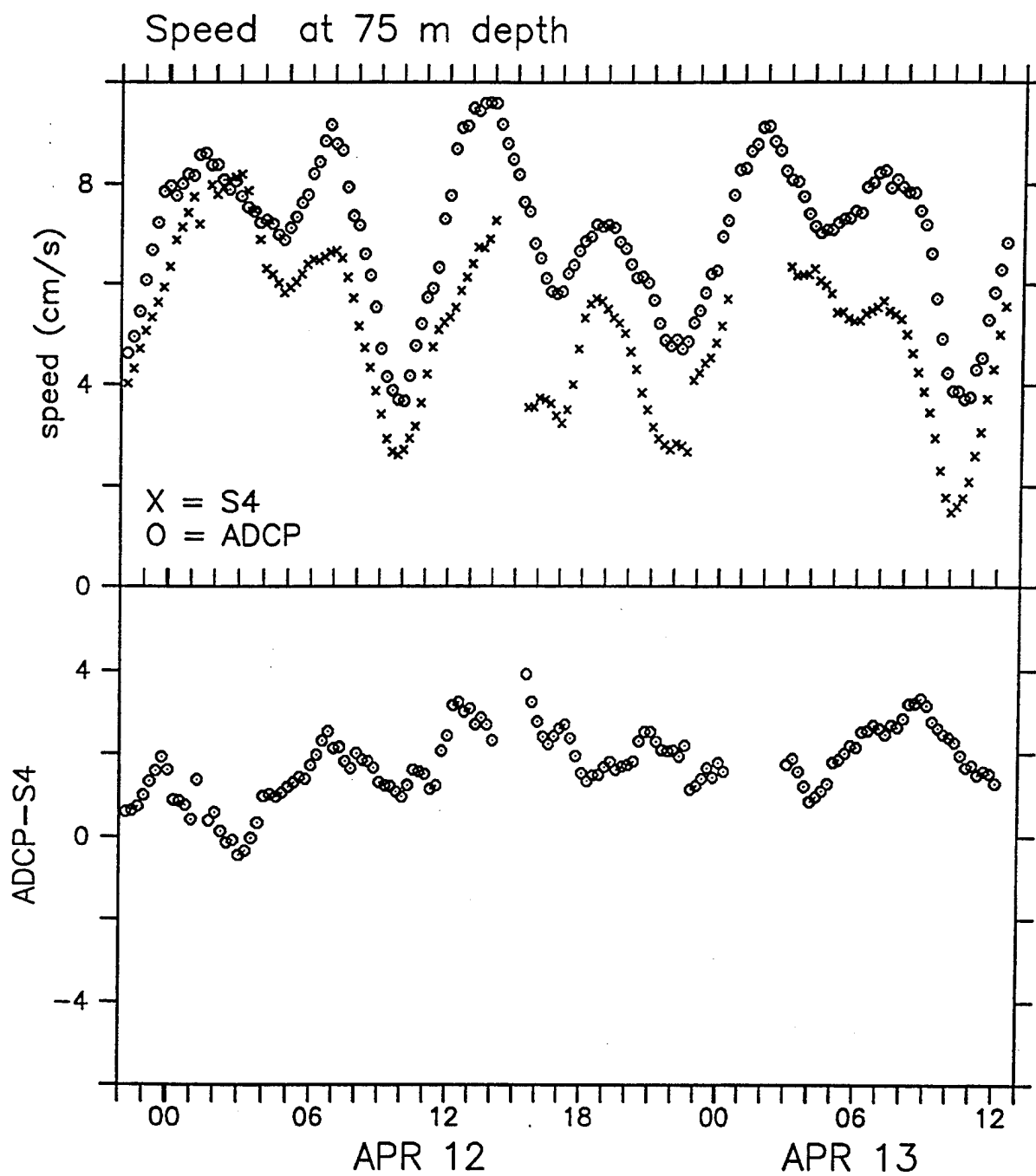


Figure 39: Time series of ADCP and S4 speed (upper panel) and ADCP - S4 speed difference (lower panel) at 75 m depth.



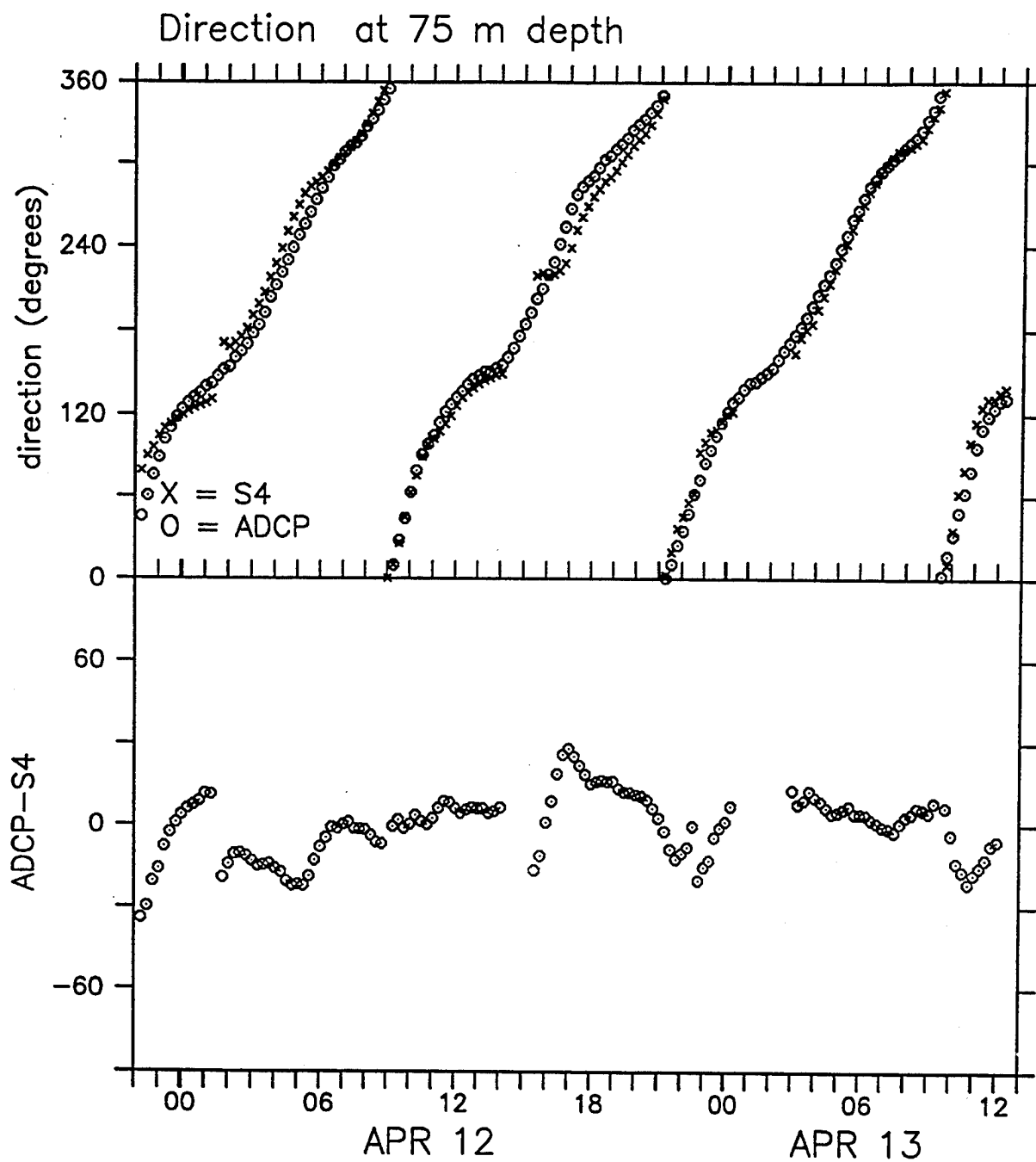


Figure 40: Time series of ADCP and S4 direction (upper panel) and ADCP - S4 direction difference (lower panel) at 75 m depth.

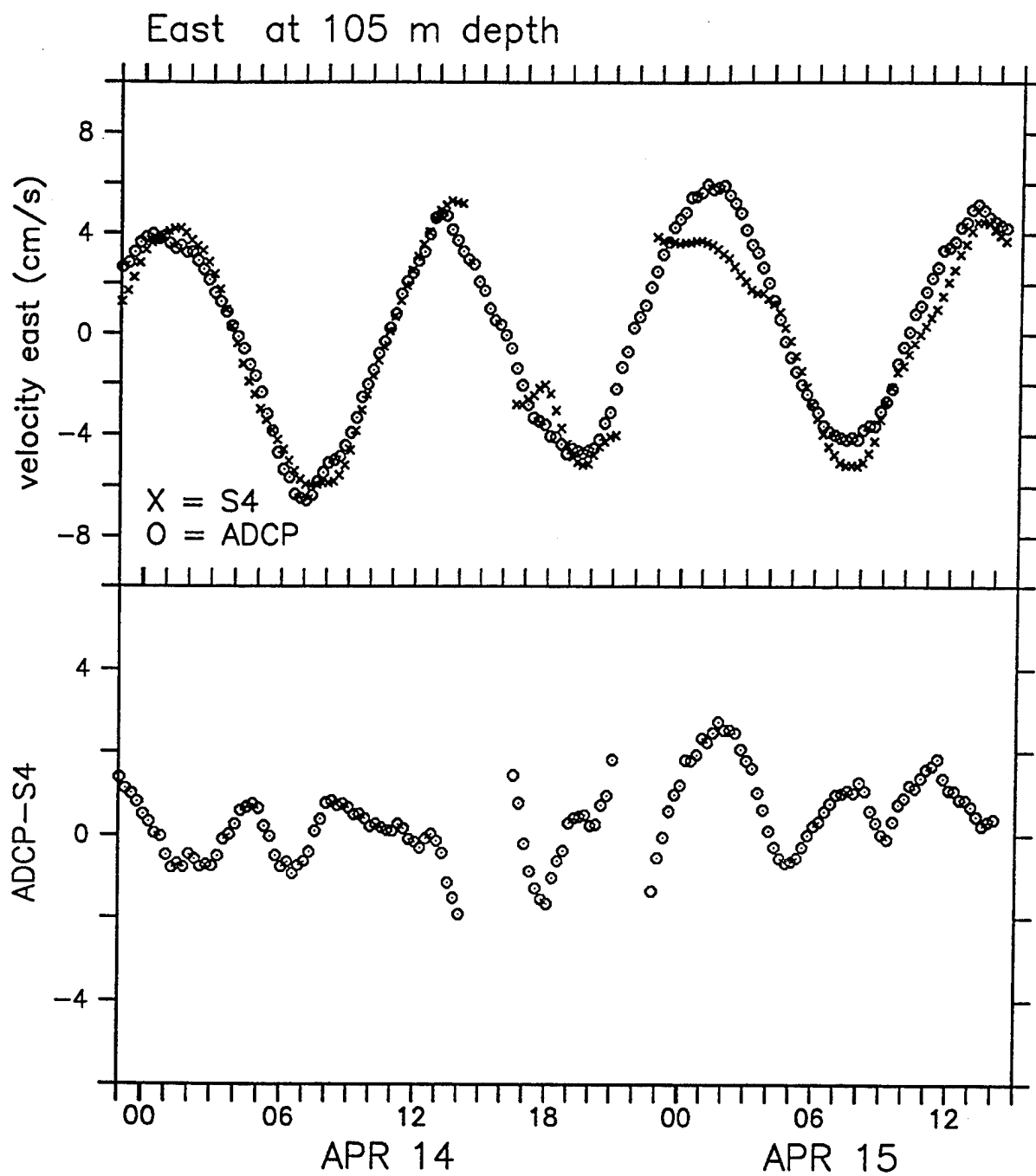


Figure 41: Time series of ADCP and S4 east velocities (upper panel) and ADCP - S4 velocity difference (lower panel) at 105 m depth.

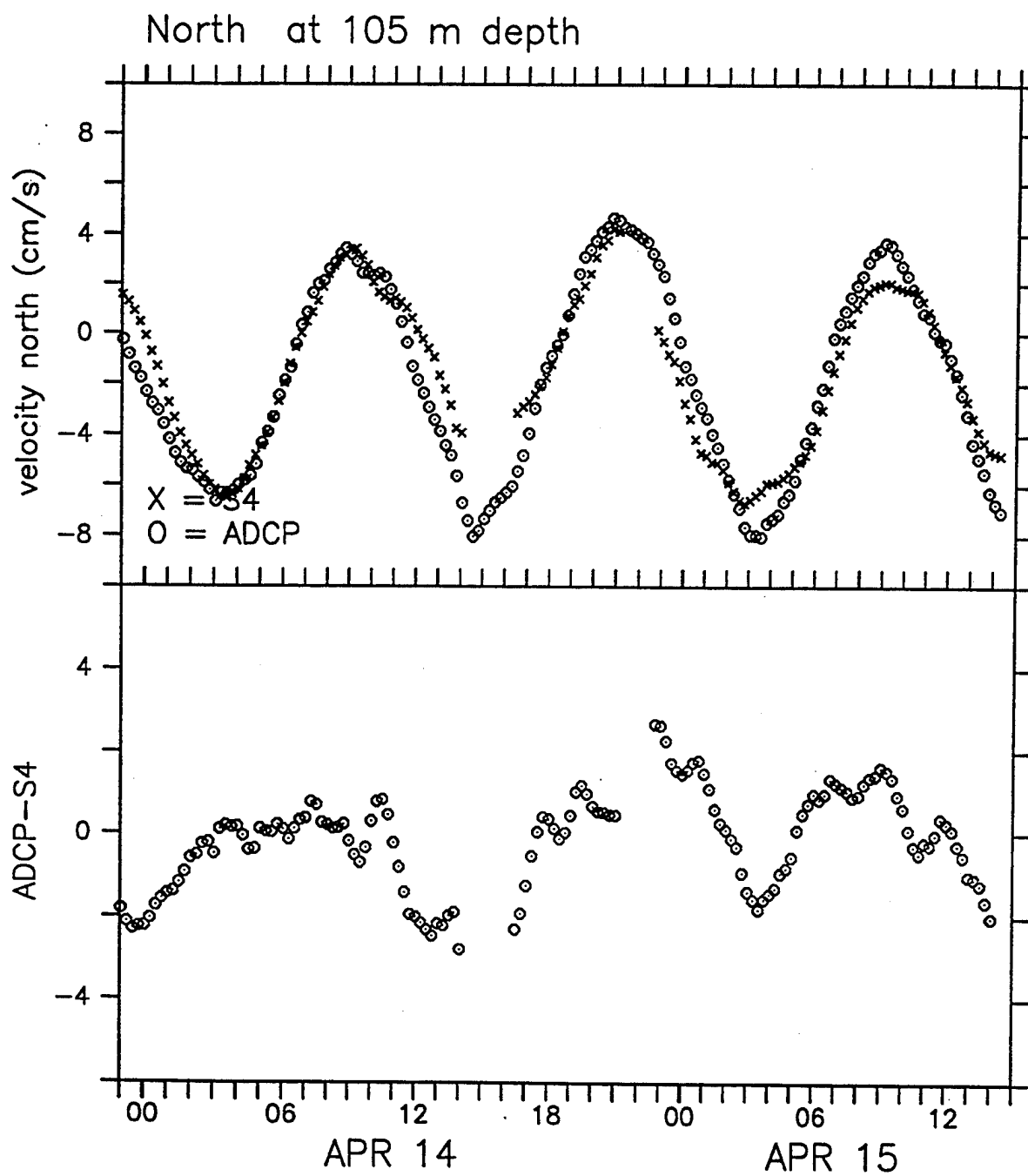


Figure 42: Time series of ADCP and S4 north velocities (upper panel) and ADCP - S4 velocity difference (lower panel) at 105 m depth.

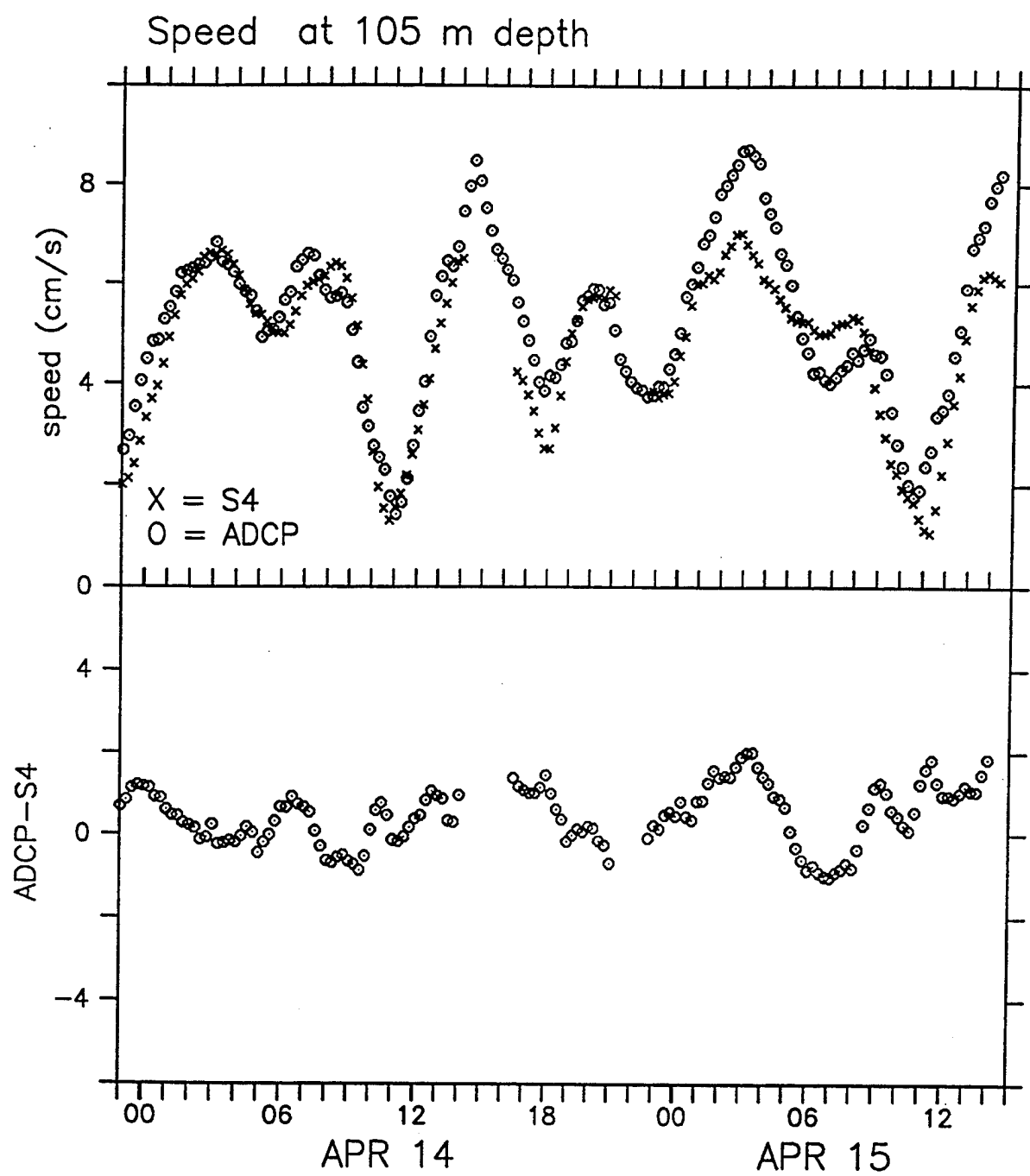


Figure 43: Time series of ADCP and S4 speed (upper panel) and ADCP - S4 speed difference (lower panel) at 105 m depth.

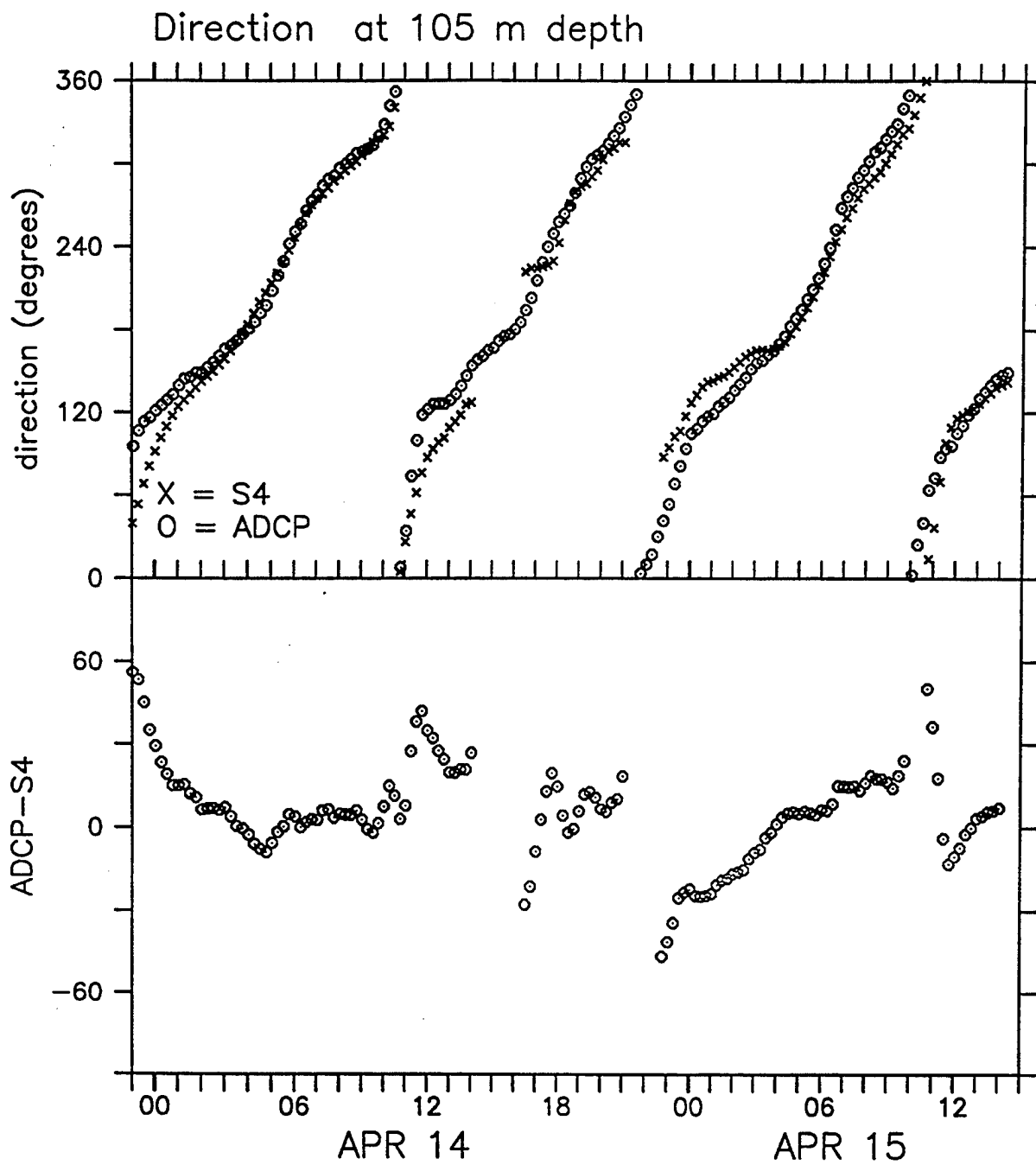


Figure 44: Time series of ADCP and S4 direction (upper panel) and ADCP - S4 direction difference (lower panel) at 105 m depth.

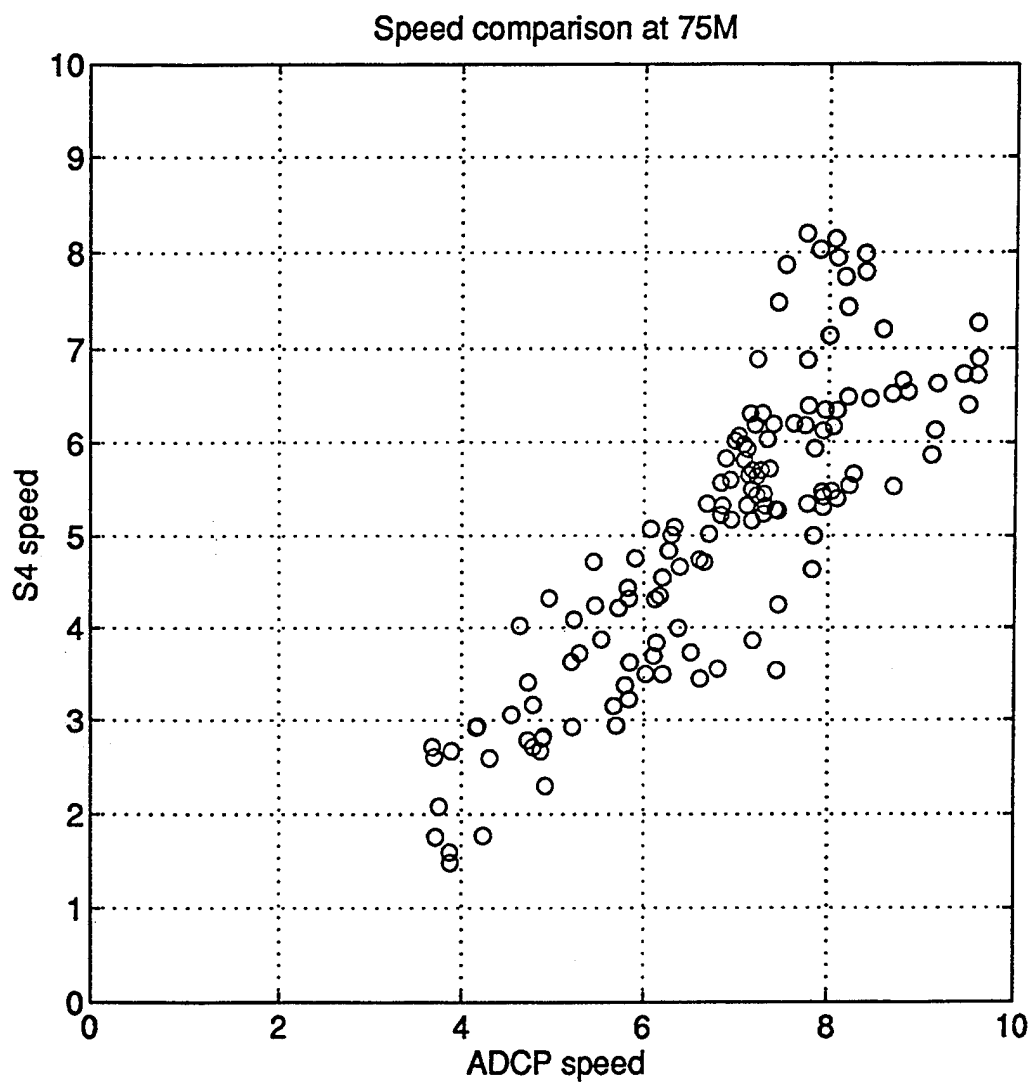


Figure 45: Scatter plot of ADCP vs. S4 speed at 75 m depth.

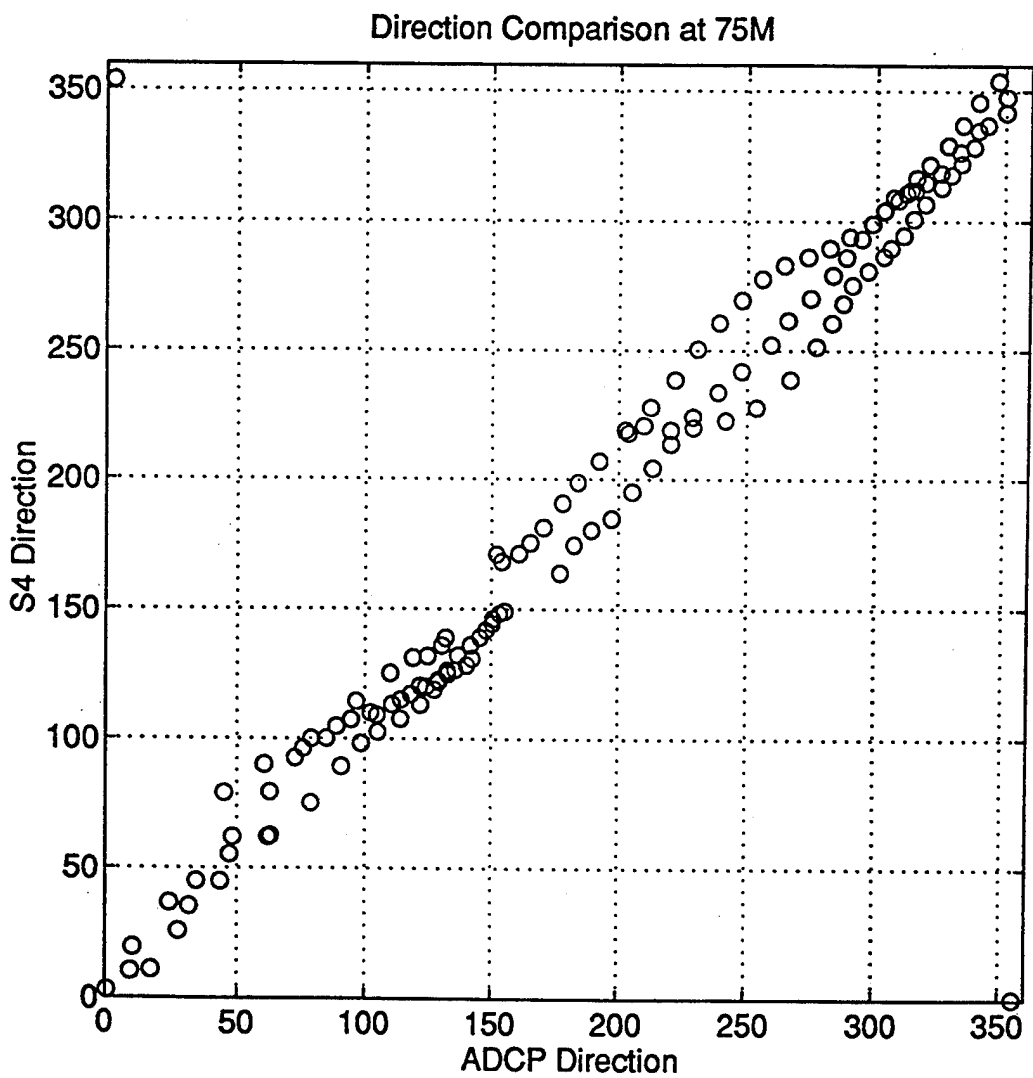


Figure 46: Scatter plot of ADCP vs. S4 direction at 75 m depth.

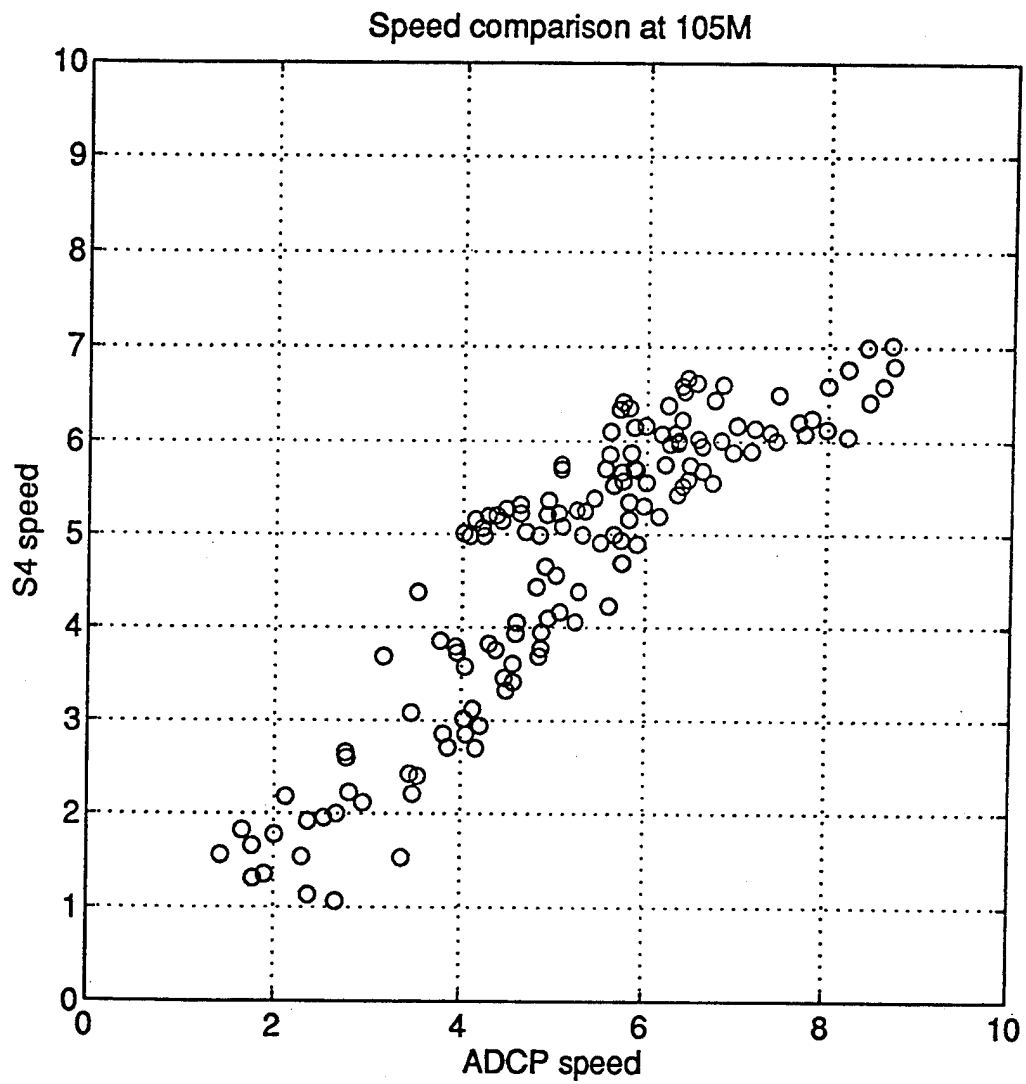


Figure 47: Scatter plot of ADCP vs. S4 speed at 105 m depth.



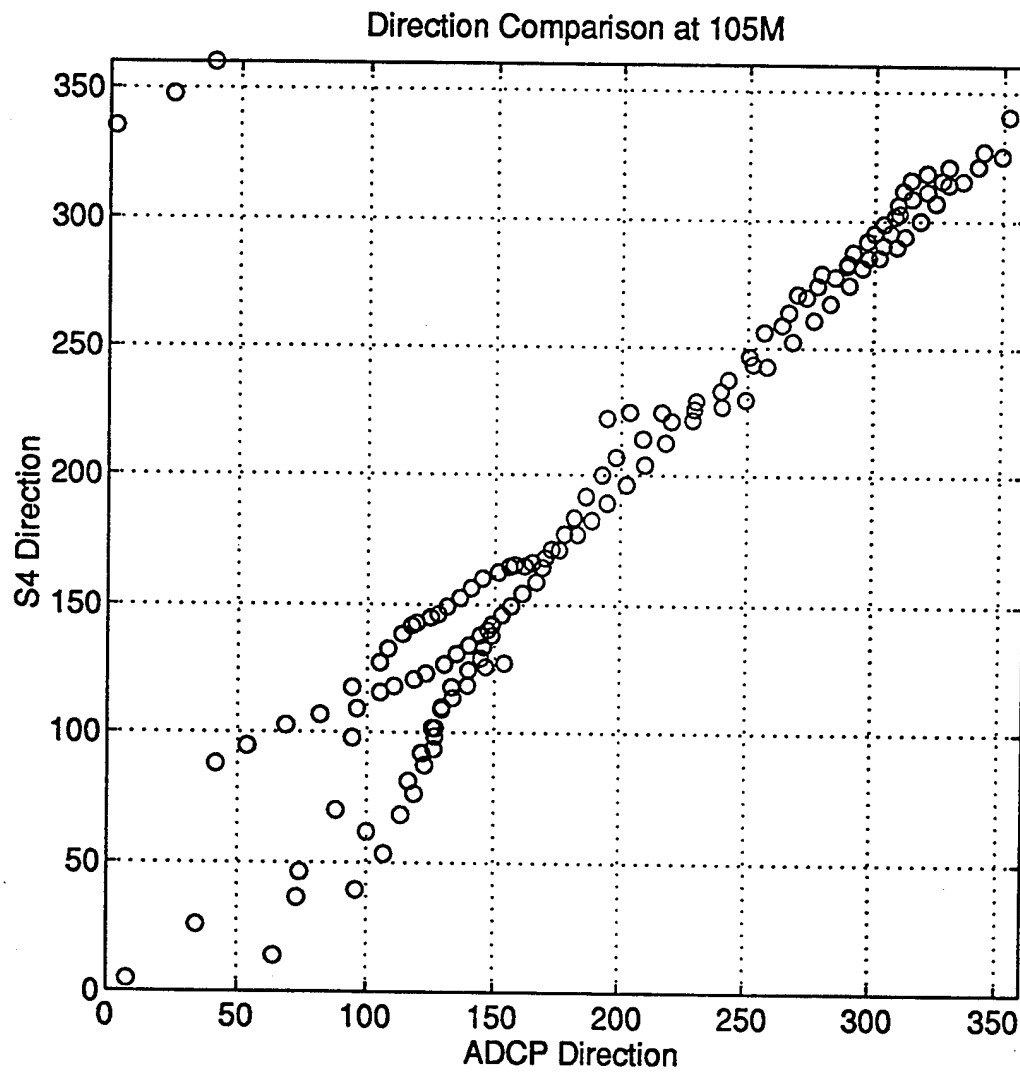


Figure 48: Scatter plot of ADCP vs. S4 direction at 105 m depth.

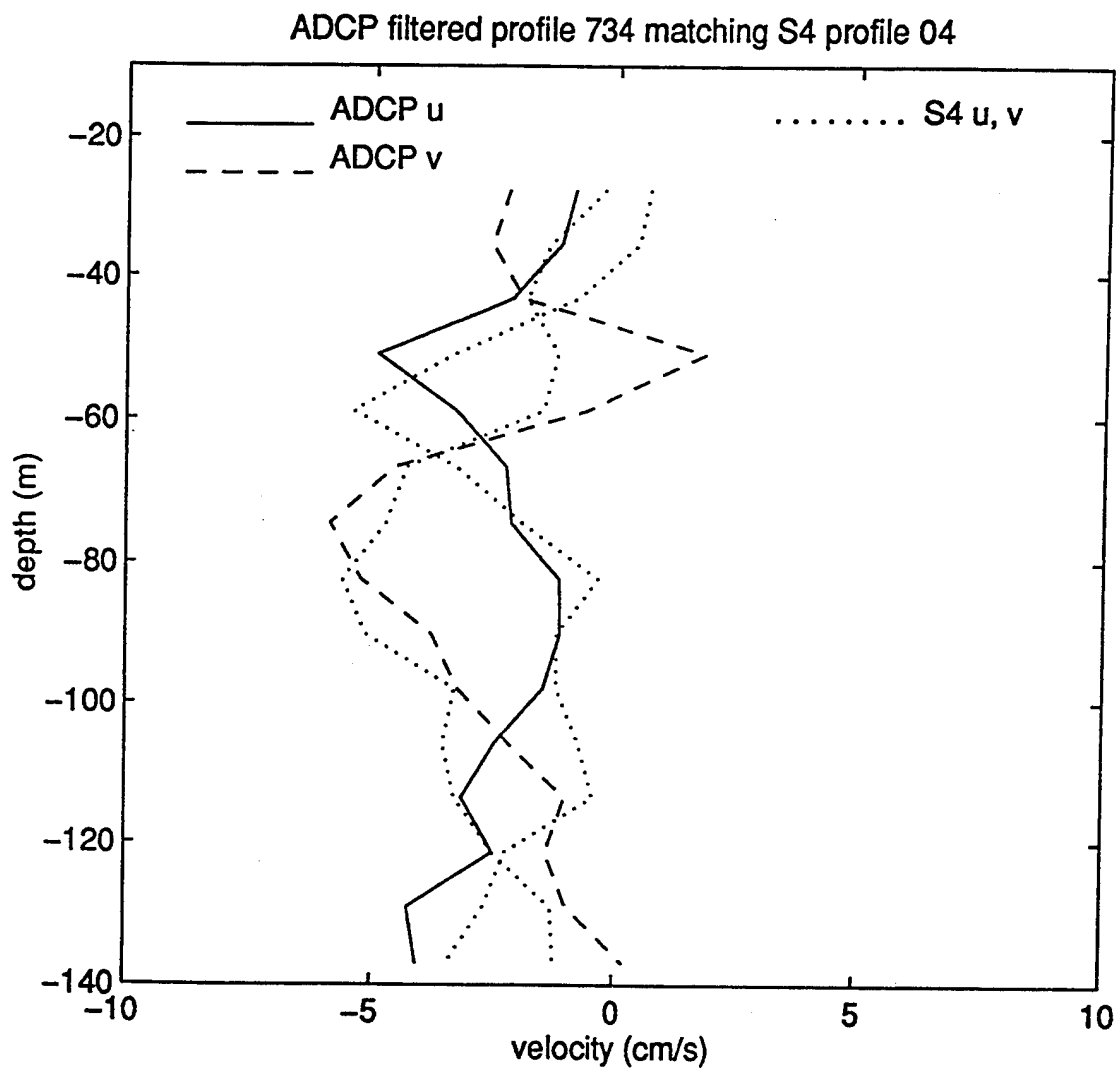


Figure 49: ADCP vs. S4 velocity comparison for profile S4-04. ADCP east (solid) and north (dashed) components are compared with those from the S4 current meter (dotted).

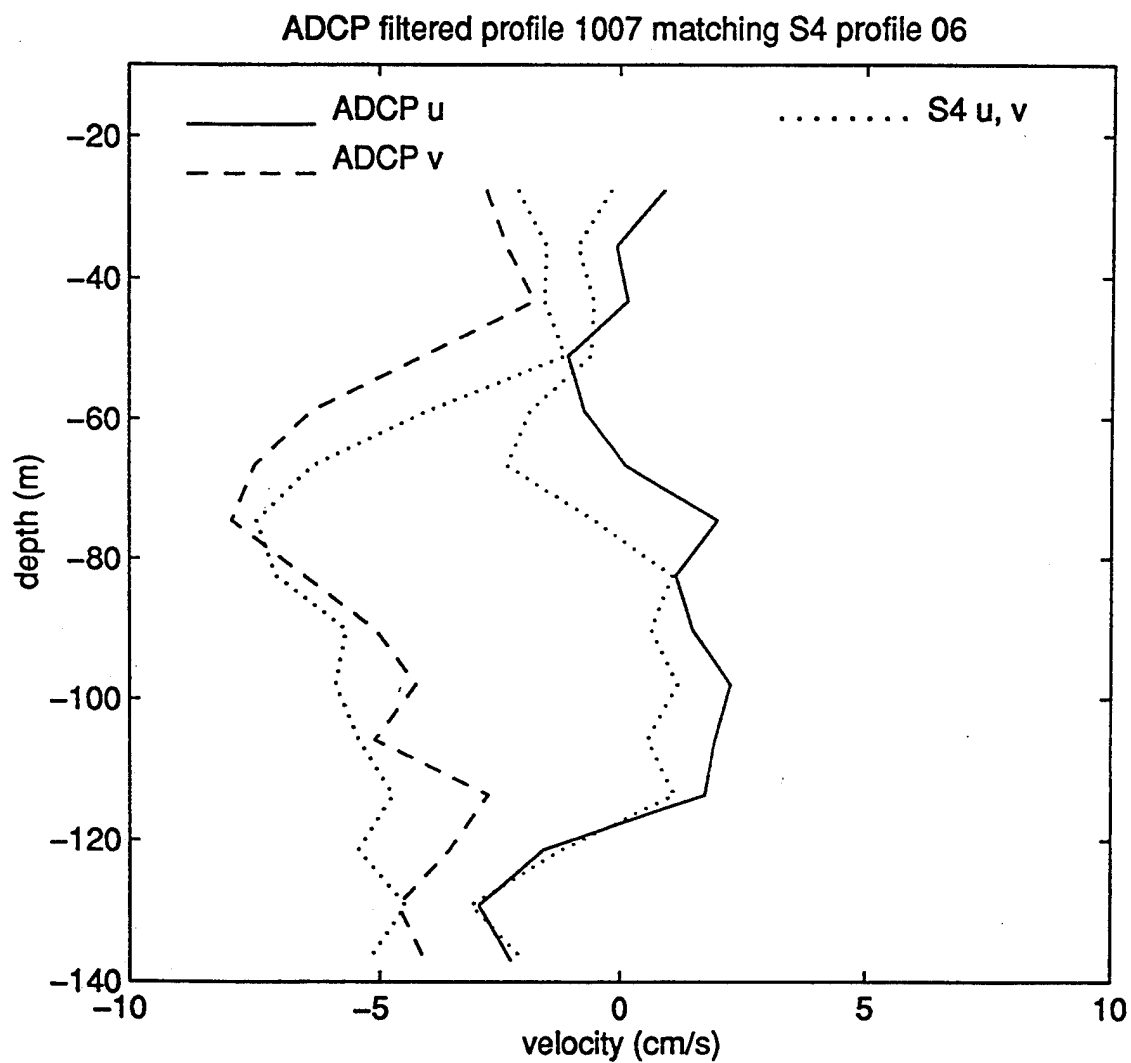


Figure 50: ADCP vs. S4 velocity comparison for profile S4-06. ADCP east (solid) and north (dashed) components are compared with those from the S4 current meter (dotted).

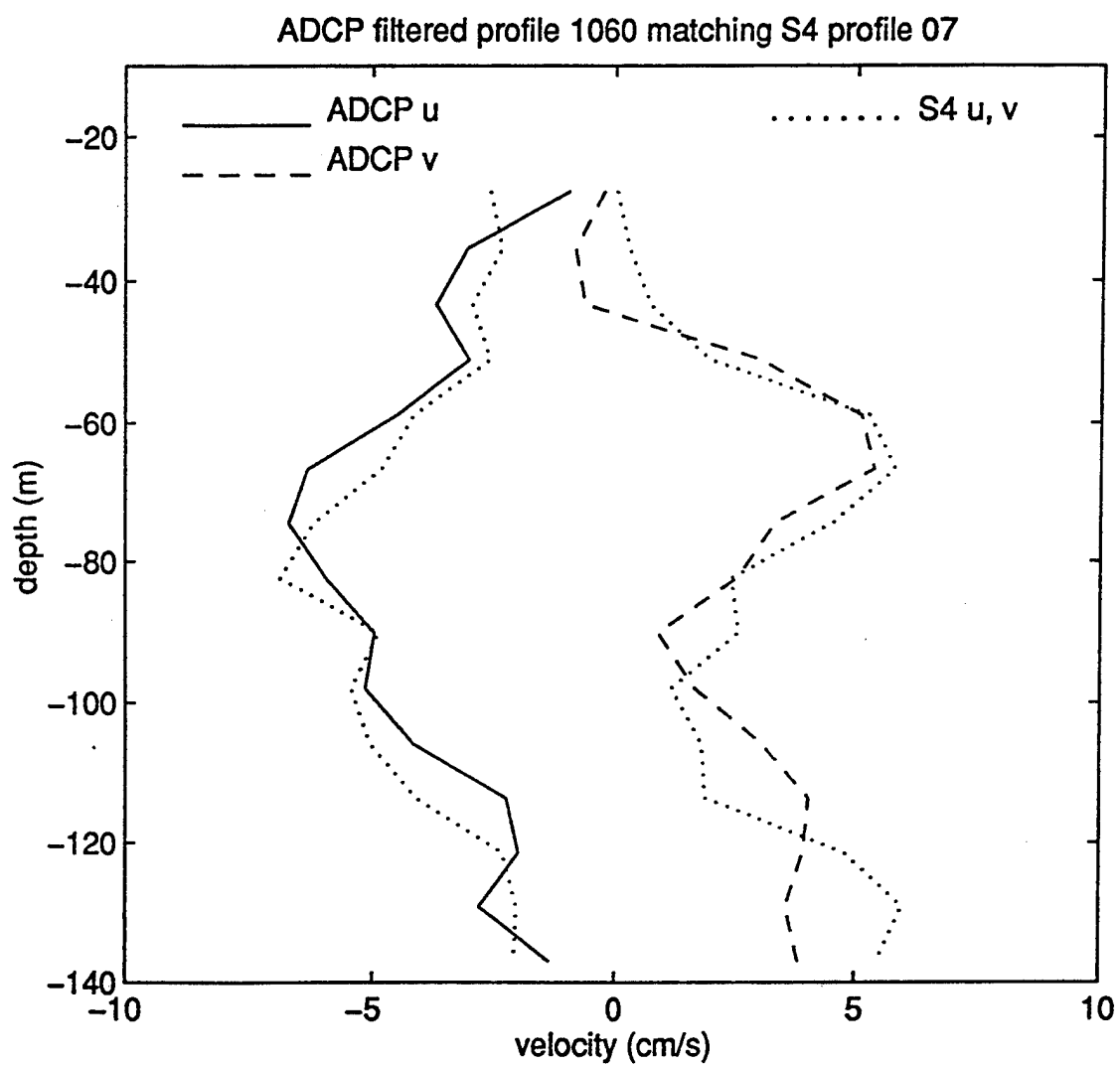


Figure 51: ADCP vs. S4 velocity comparison for profile S4-07. ADCP east (solid) and north (dashed) components are compared with those from the S4 current meter (dotted).

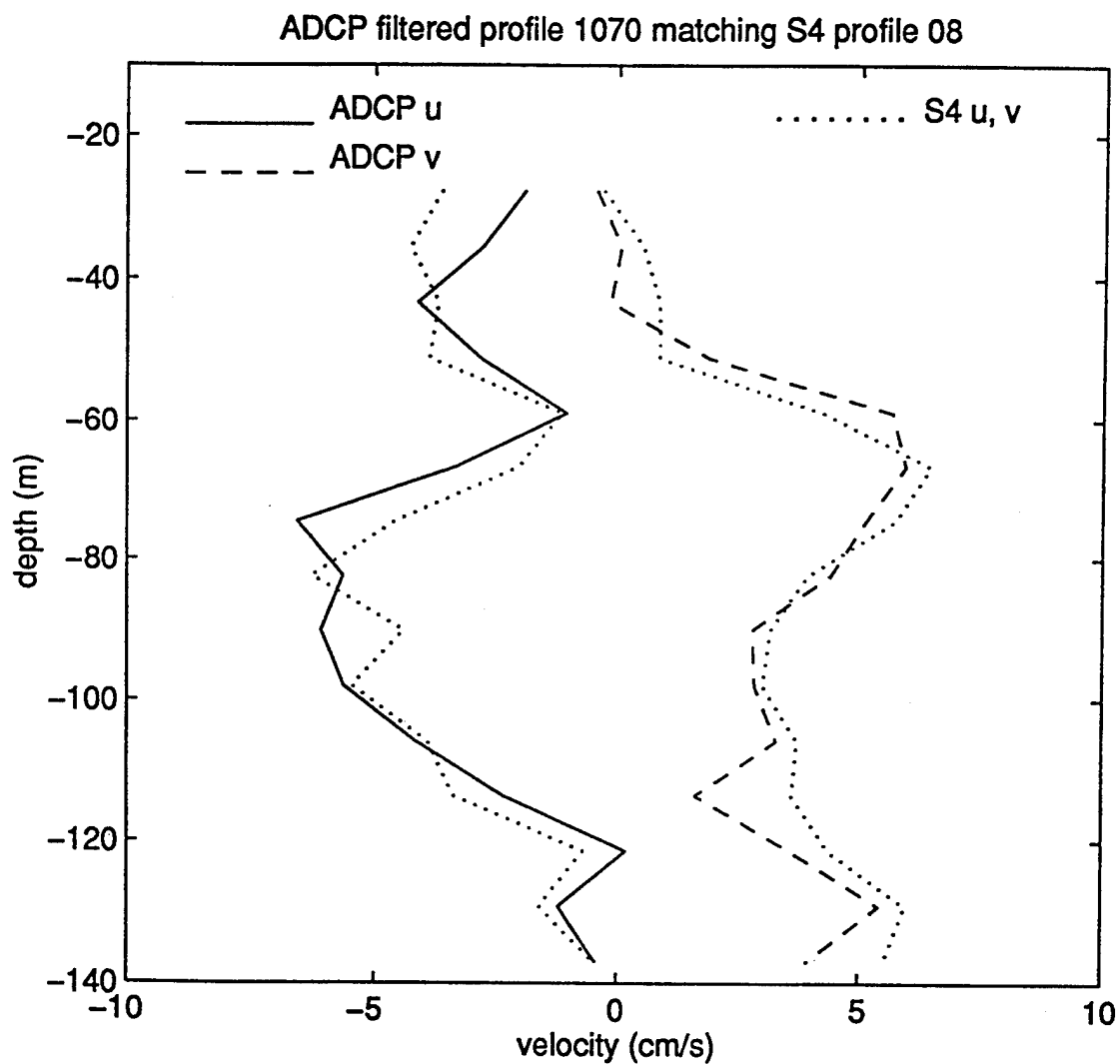


Figure 52: ADCP vs. S4 velocity comparison for profile S4-08. ADCP east (solid) and north (dashed) components are compared with those from the S4 current meter (dotted).

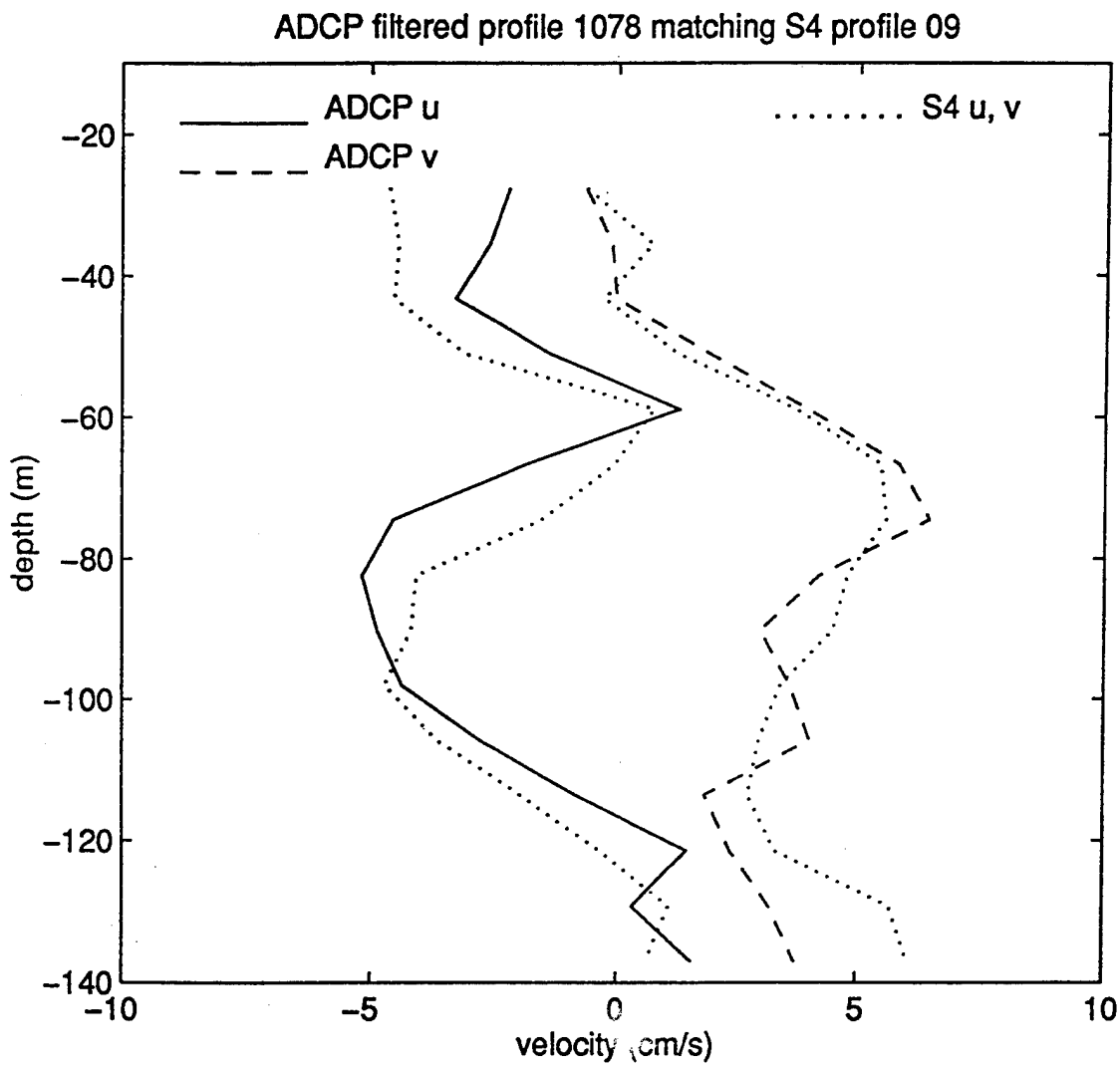


Figure 53: ADCP vs. S4 velocity comparison for profile S4-09. ADCP east (solid) and north (dashed) components are compared with those from the S4 current meter (dotted).

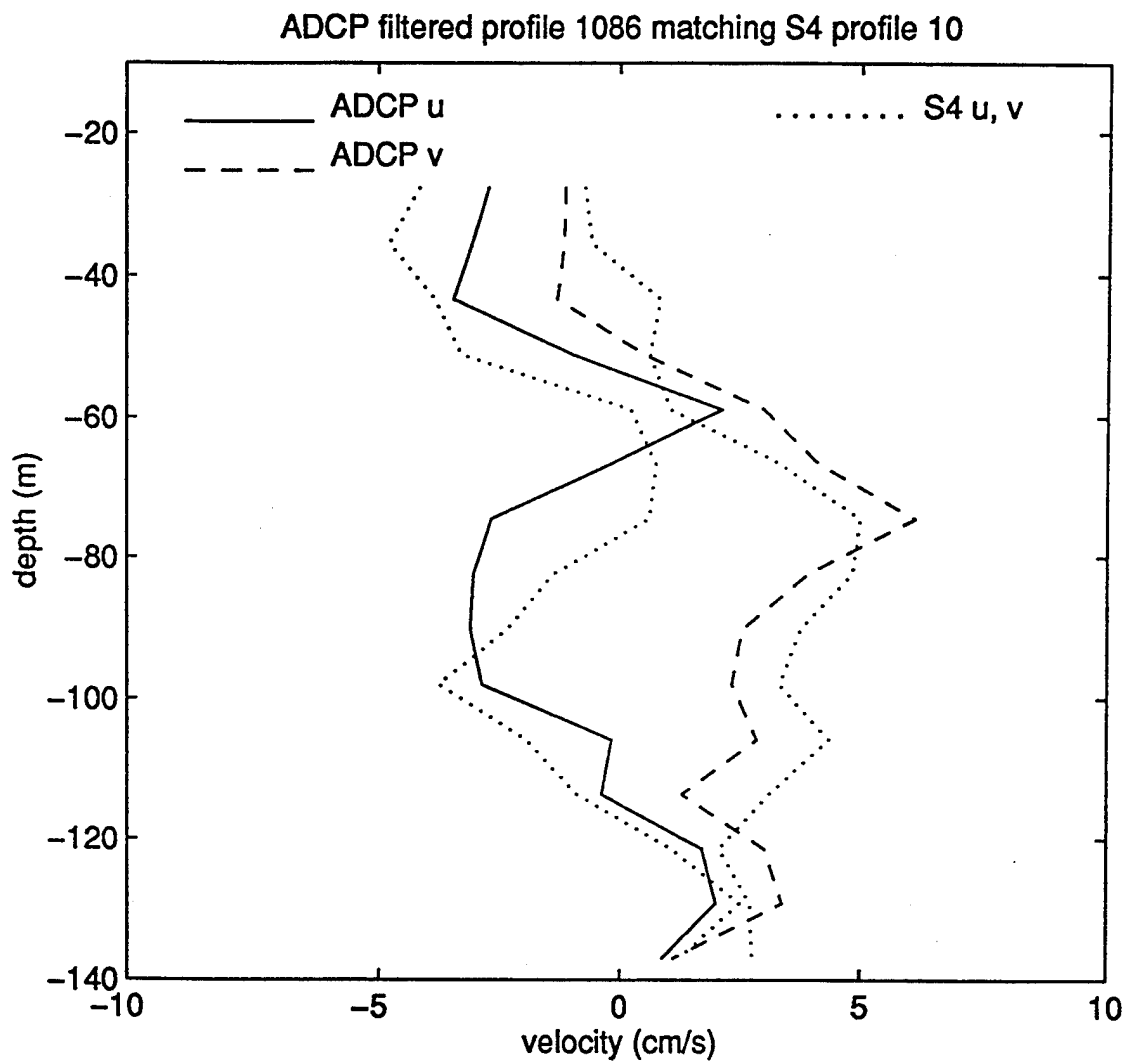


Figure 54: ADCP vs. S4 velocity comparison for profile S4-10. ADCP east (solid) and north (dashed) components are compared with those from the S4 current meter (dotted).

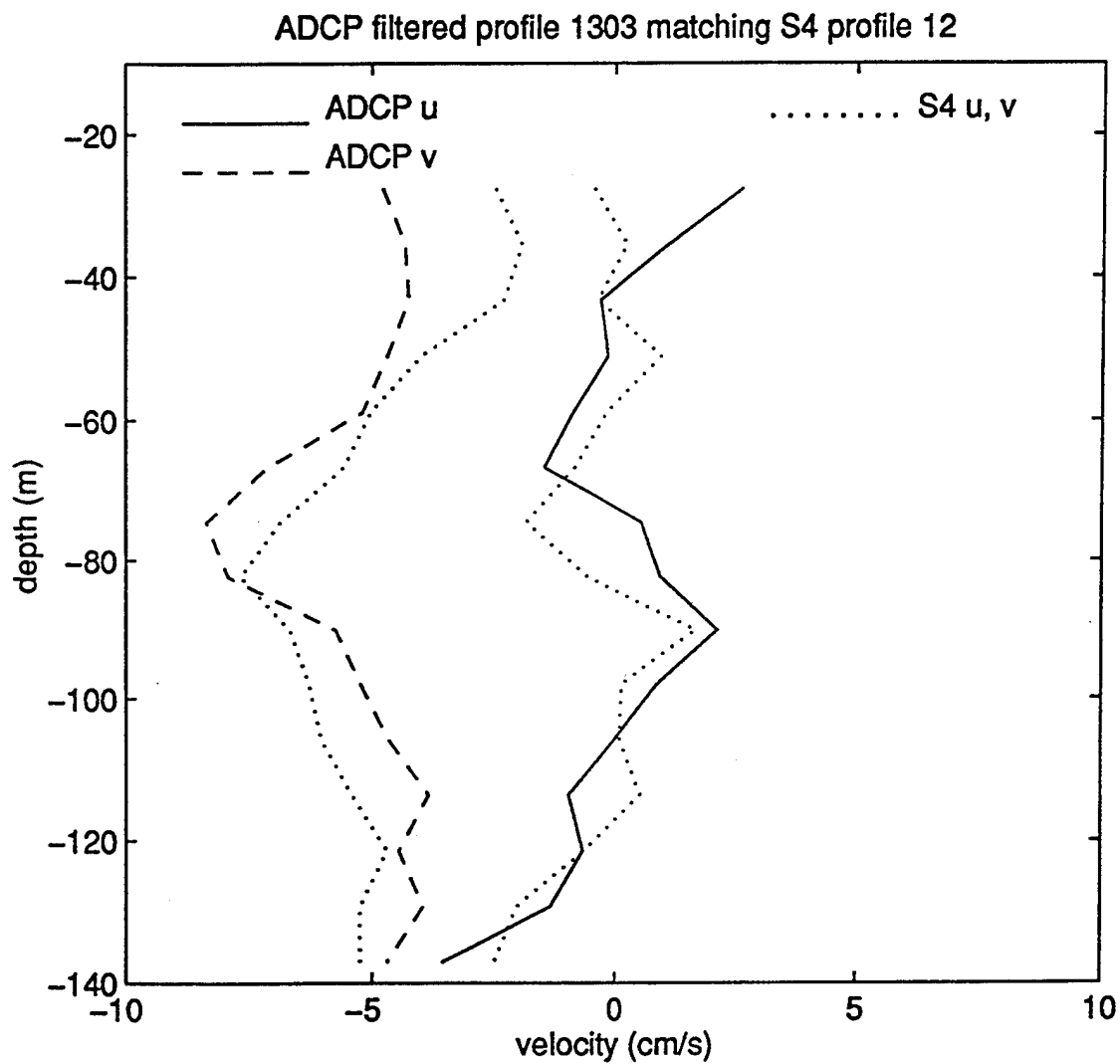


Figure 55: ADCP vs. S4 velocity comparison for profile S4-12. ADCP east (solid) and north (dashed) components are compared with those from the S4 current meter (dotted).



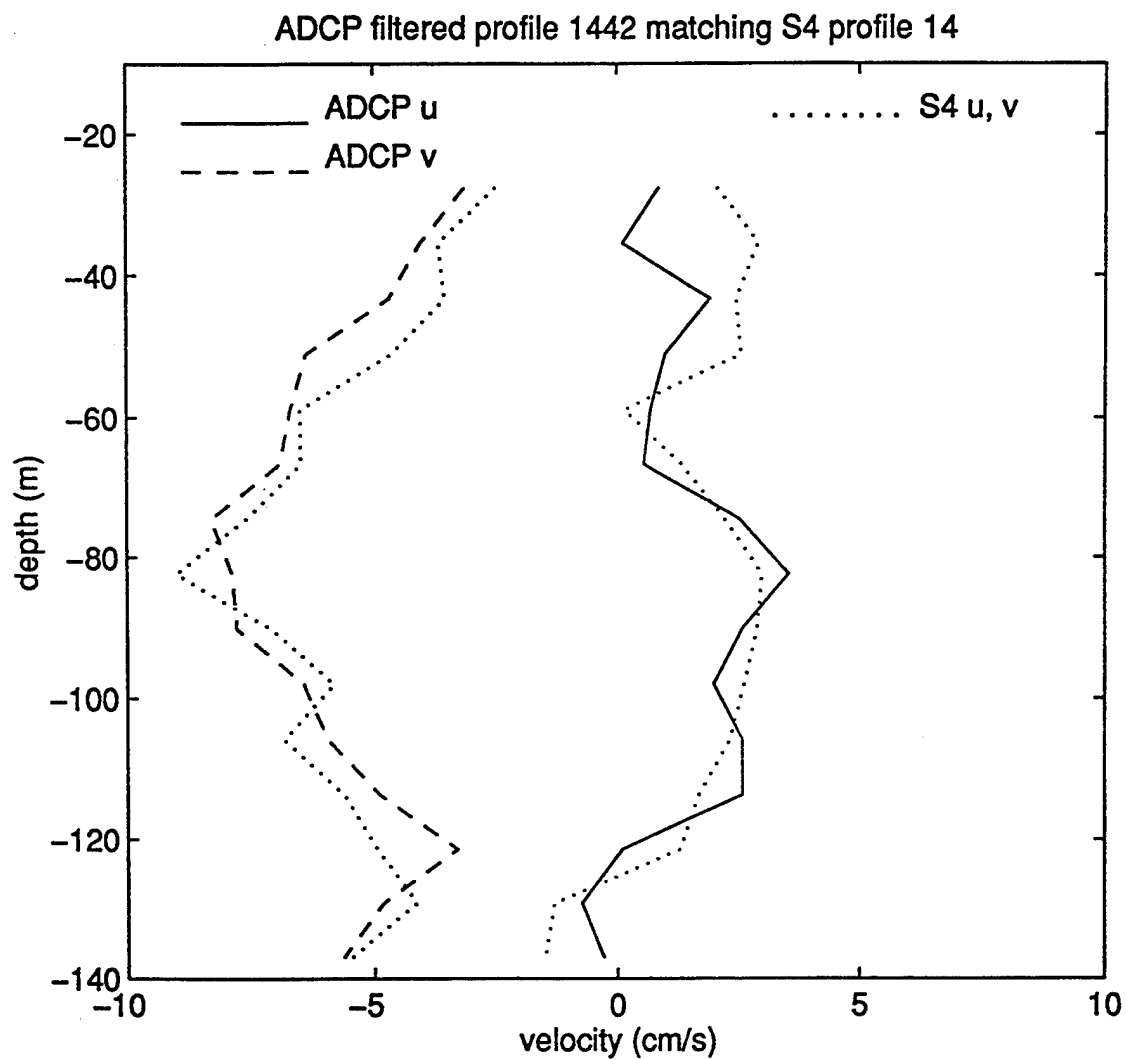


Figure 56: ADCP vs. S4 velocity comparison for profile S4-14. ADCP east (solid) and north (dashed) components are compared with those from the S4 current meter (dotted).

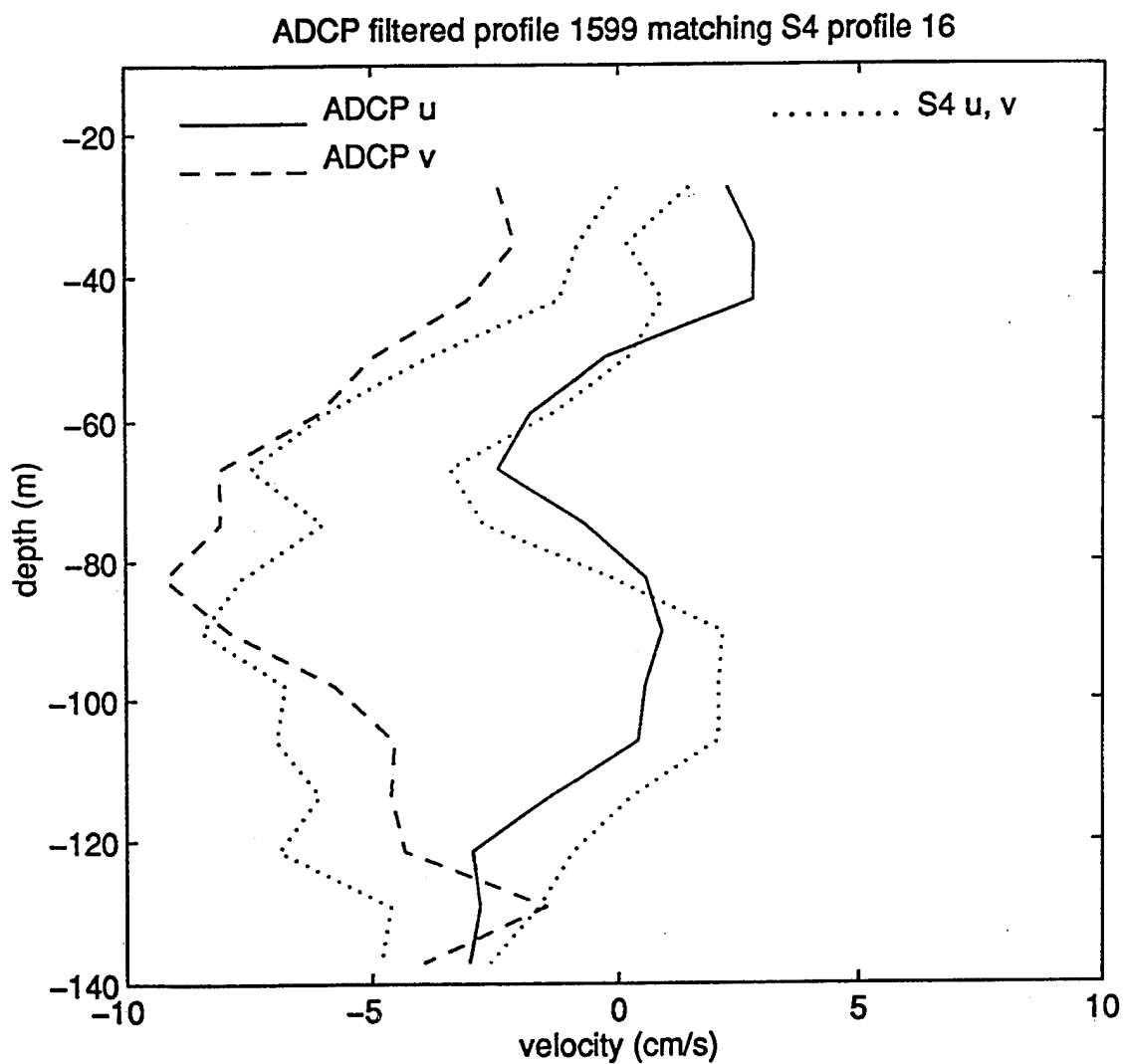


Figure 57: ADCP vs. S4 velocity comparison for profile S4-16. ADCP east (solid) and north (dashed) components are compared with those from the S4 current meter (dotted).

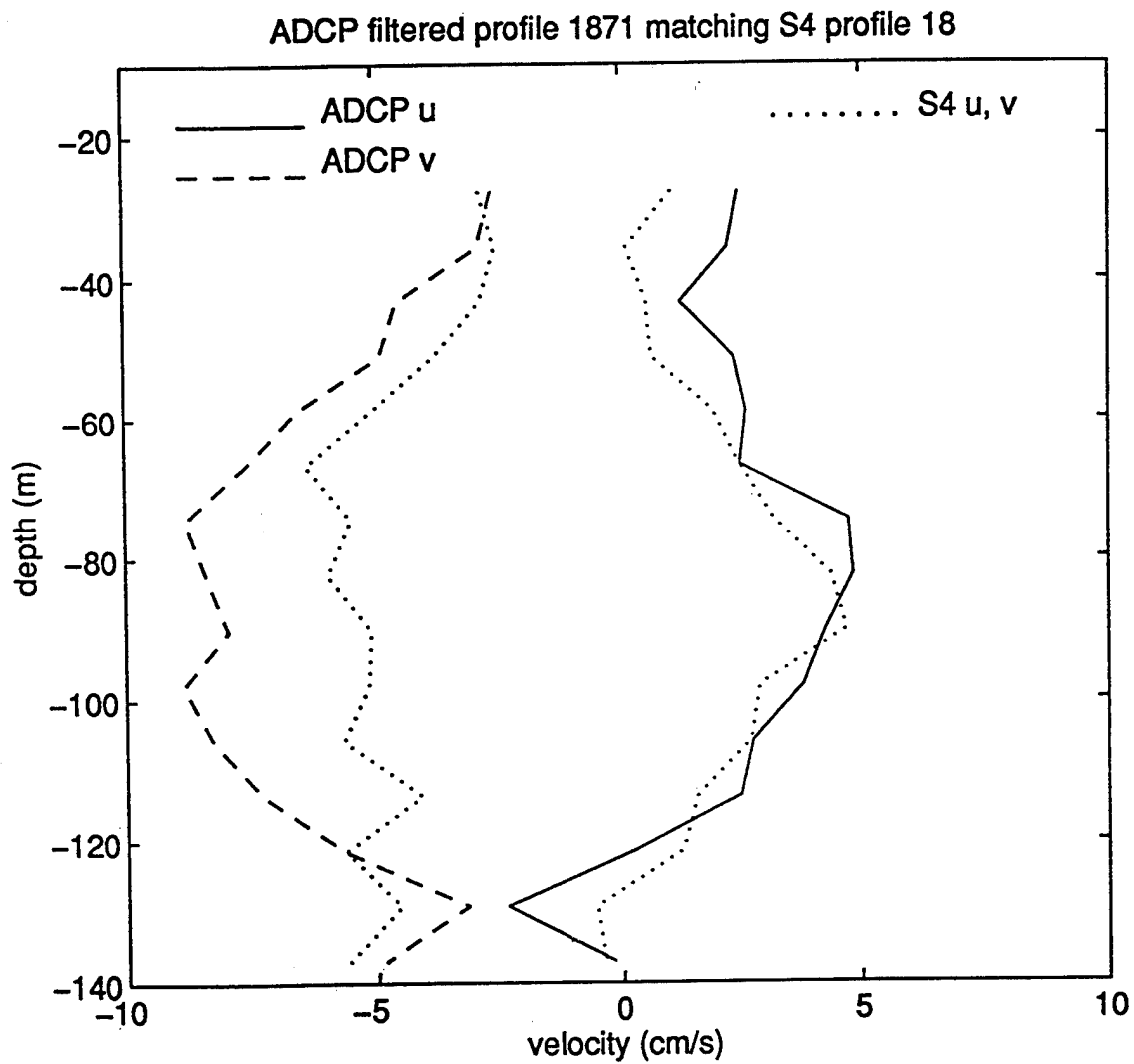


Figure 58: ADCP vs. S4 velocity comparison for profile S4-18. ADCP east (solid) and north (dashed) components are compared with those from the S4 current meter (dotted).

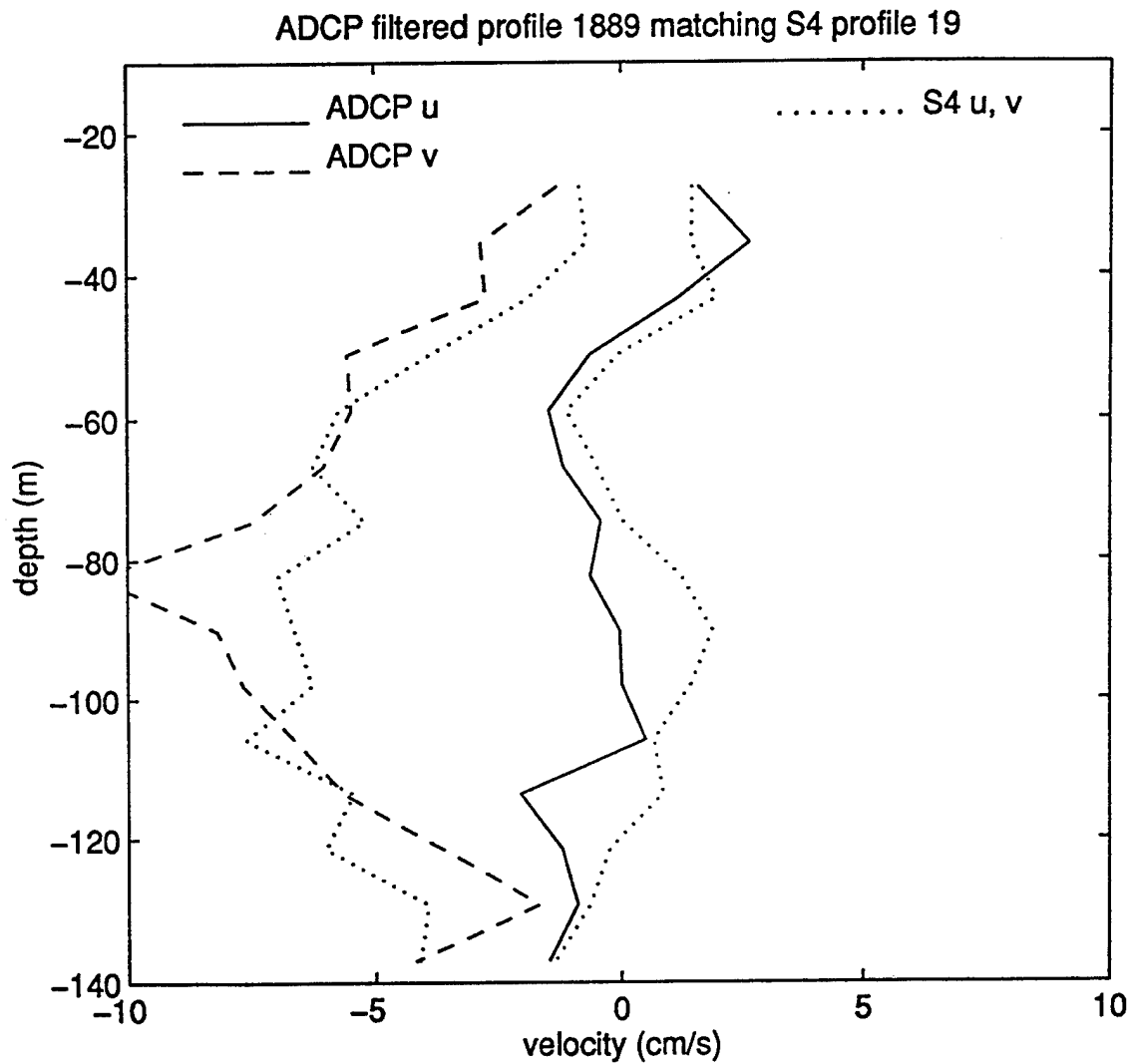


Figure 59: ADCP vs. S4 velocity comparison for profile S4-19. ADCP east (solid) and north (dashed) components are compared with those from the S4 current meter (dotted).

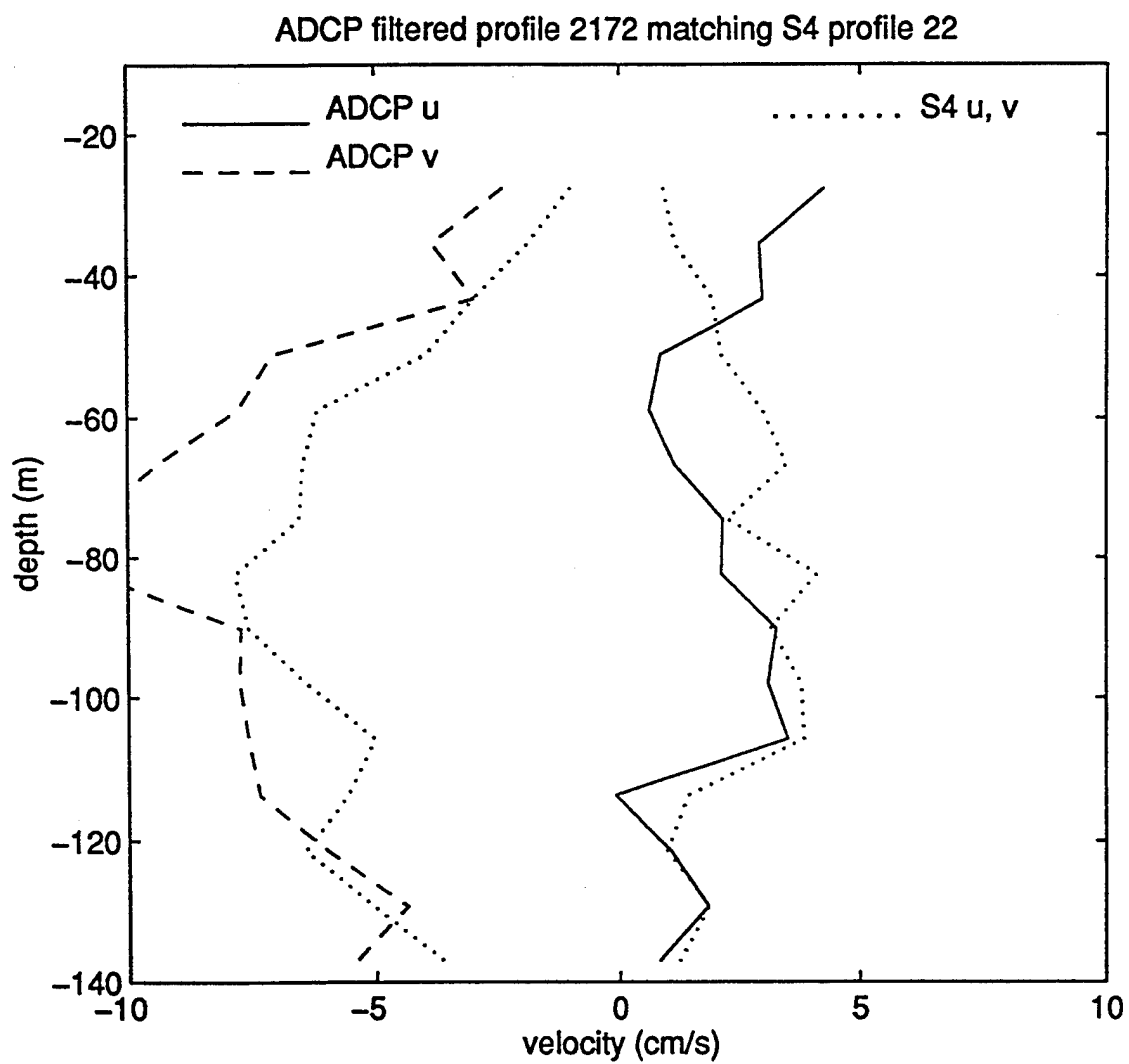


Figure 60: ADCP vs. S4 velocity comparison for profile S4-22. ADCP east (solid) and north (dashed) components are compared with those from the S4 current meter (dotted).

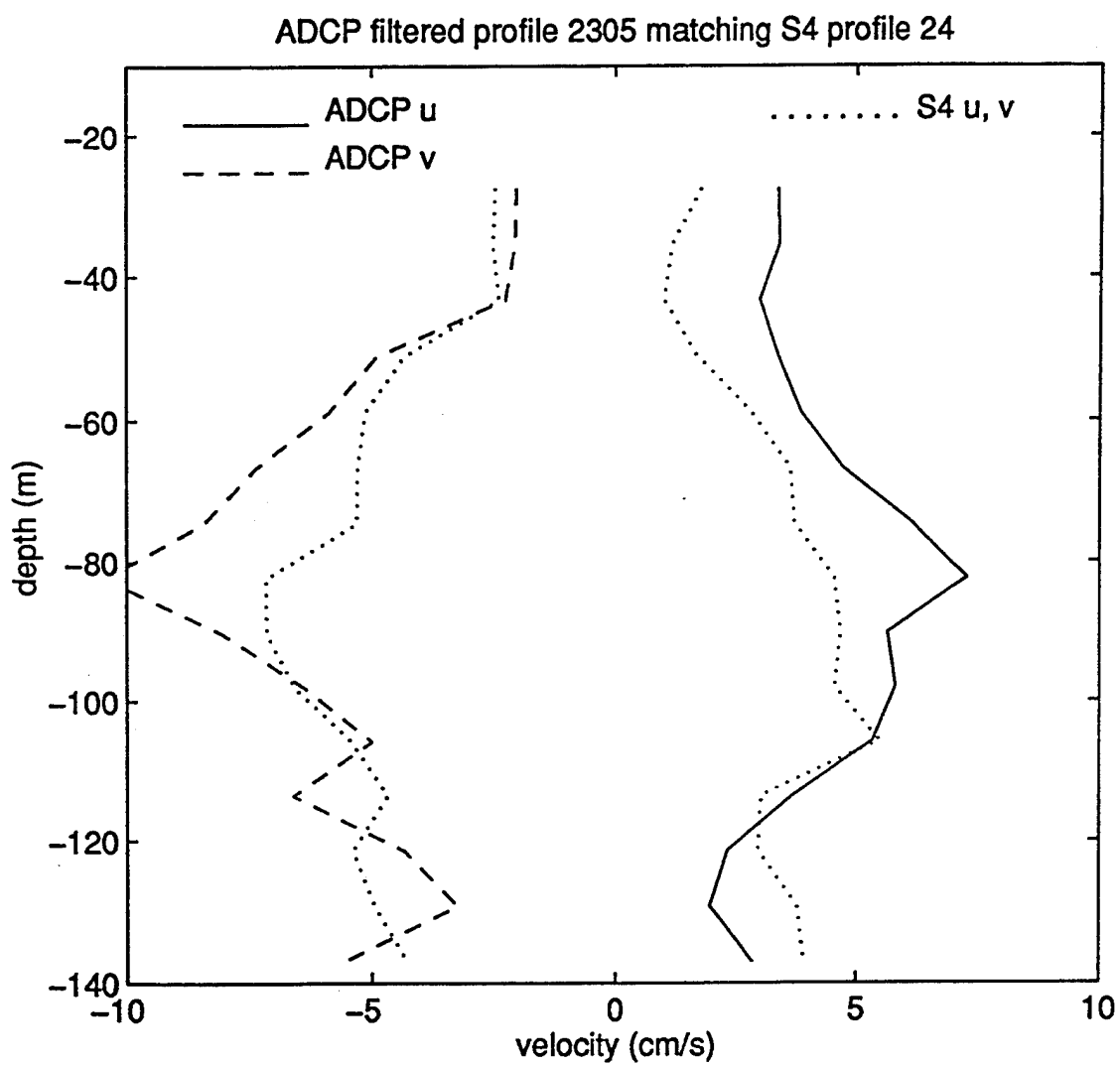


Figure 61: ADCP vs. S4 velocity comparison for profile S4-24. ADCP east (solid) and north (dashed) components are compared with those from the S4 current meter (dotted).

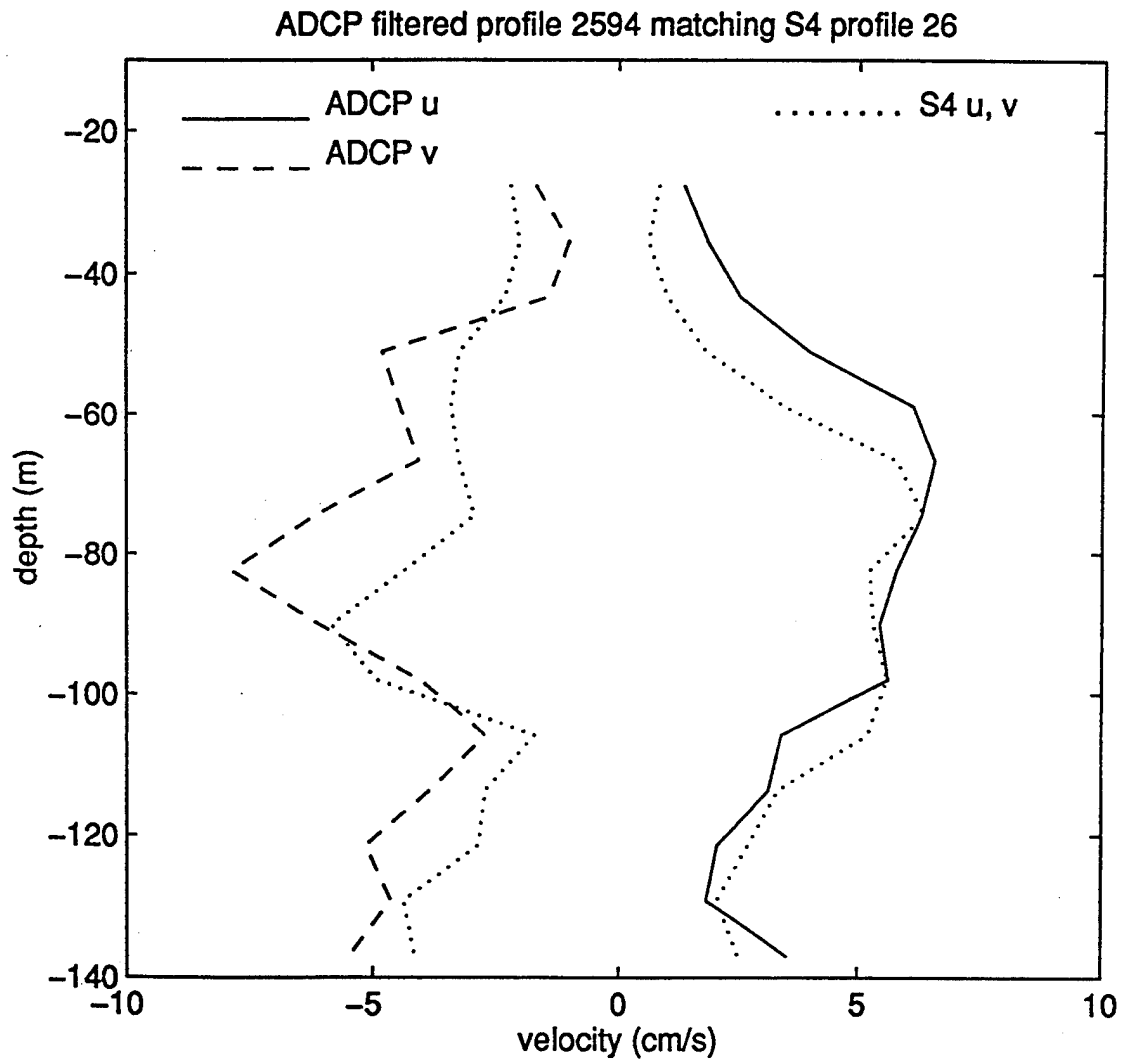


Figure 62: ADCP vs. S4 velocity comparison for profile S4-26. ADCP east (solid) and north (dashed) components are compared with those from the S4 current meter (dotted).

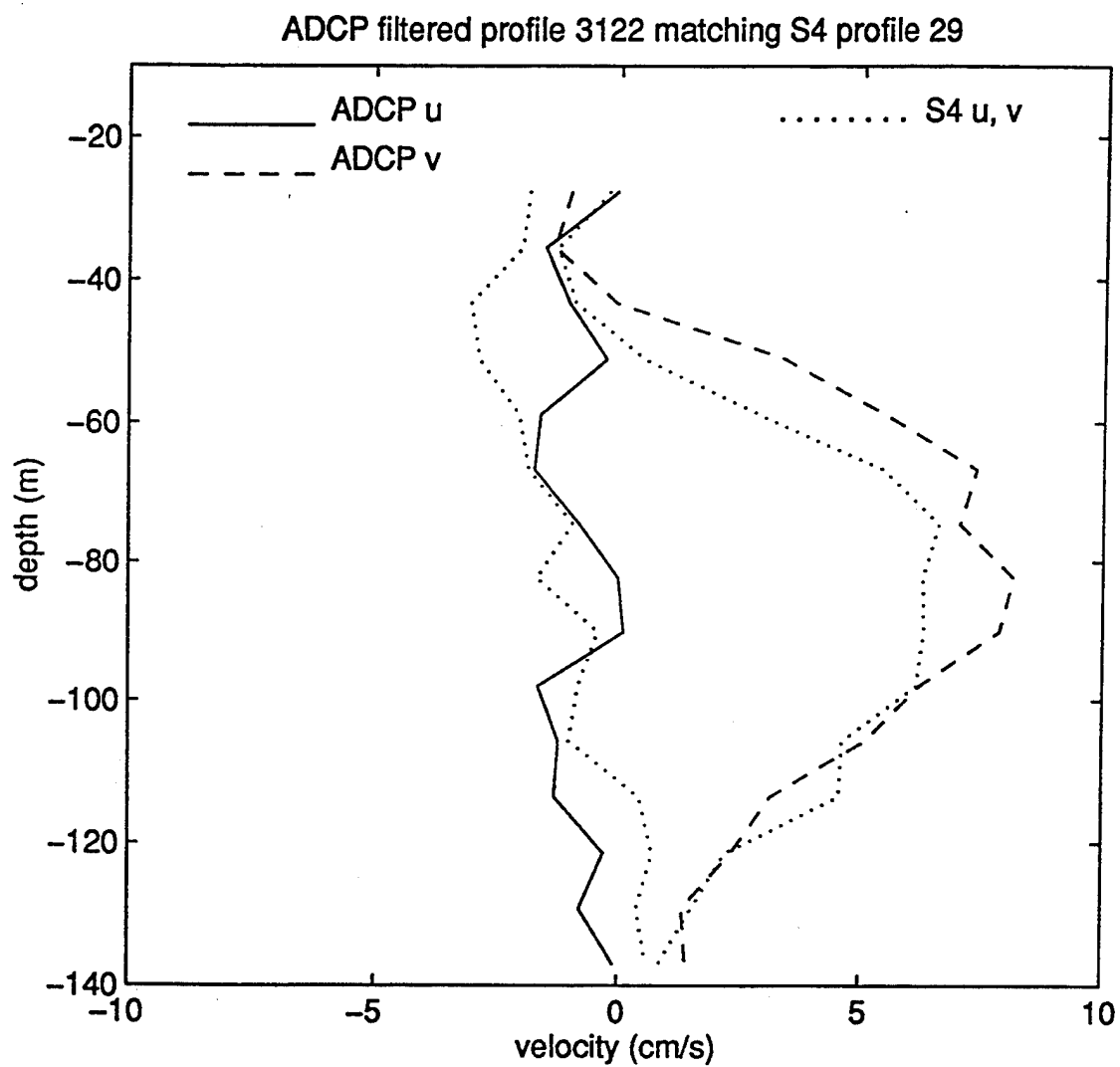


Figure 63: ADCP vs. S4 velocity comparison for profile S4-29. ADCP east (solid) and north (dashed) components are compared with those from the S4 current meter (dotted).



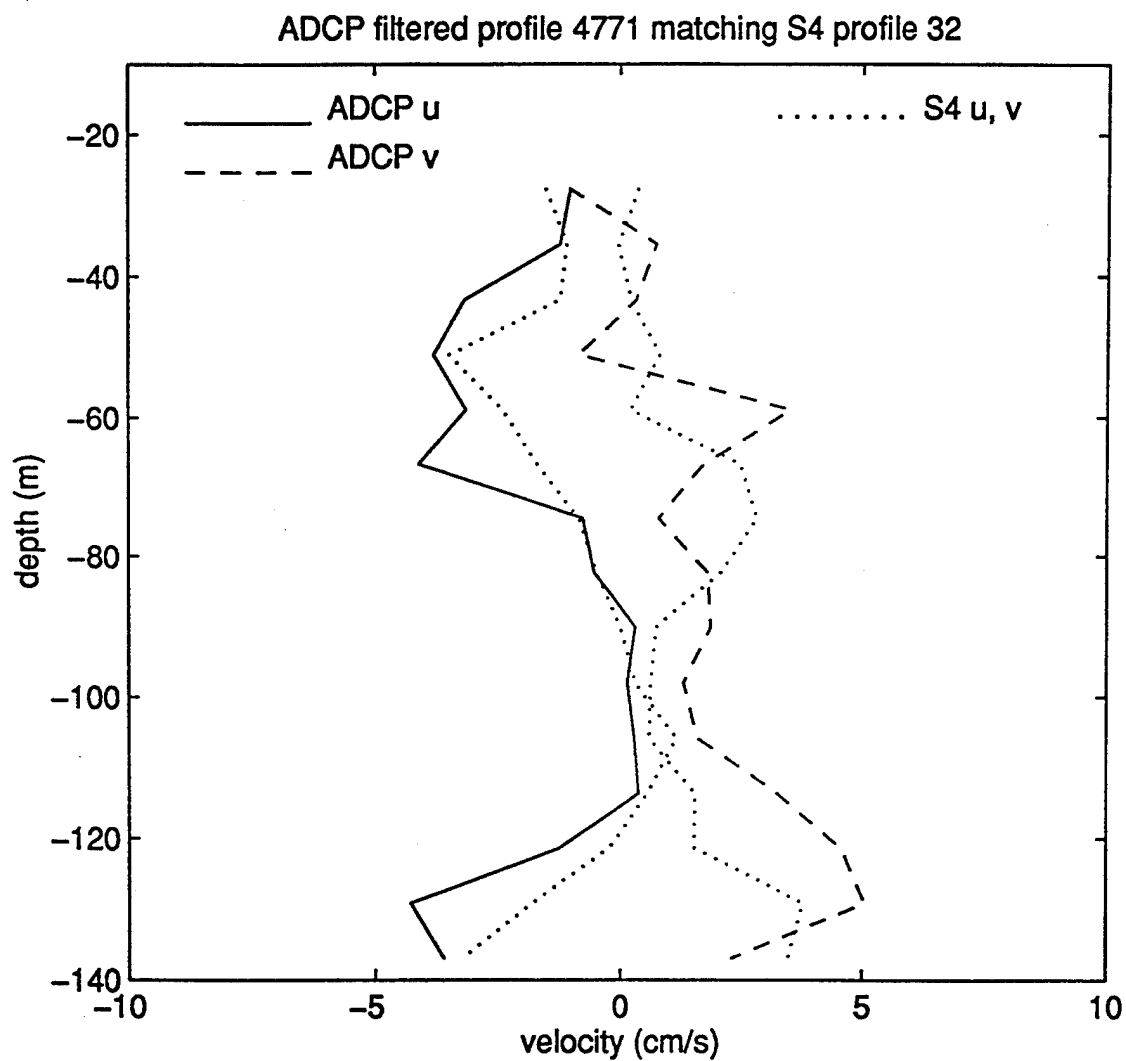


Figure 64: ADCP vs. S4 velocity comparison for profile S4-32. ADCP east (solid) and north (dashed) components are compared with those from the S4 current meter (dotted).

## Acknowledgments

Coordination of the joint effort between the Woods Hole Oceanographic Institution (WHOI) and the Naval Research and Development lab (NRaD) for ADCP measurements during ICESHELF 94 was done by Barbara Sotirin and John Newton of NRaD. They also handled the configuration and deployment of the ADCP at the ice camp. William Ostrom of the Upper Ocean Processes Group at WHOI provided the hardware for the ADCP deployment as well as expert advice. This work was funded by Code 322-HL of the Office of Naval Research under Grant Number N00014-90-J-1359.

## References

- Flagg, C. N. and S. L. Smith, 1989. On the use of the acoustic Doppler current profiler to measure zooplankton abundance. *Deep-Sea Research*, **36**(3), 455-474.
- Hansen, D. S., 1985. Asymptotic performance of a pulse-to-pulse incoherent Doppler sonar in an oceanic environment. *IEEE Journal of Ocean Engineering*, **OE-10**(2), 144, 158.
- Joyce, T. M., D. S. Bitterman, Jr., and K. E. Prada, 1982. Shipboard acoustic profiling of upper ocean currents. *Deep-Sea Research*, **29**(7A), 903-913.
- Pinkel, R. 1982. On estimating the quality of Doppler sonar data. *Proceedings IEEE Second Working Conference on Current Measurement*, 113-116.
- RD Instruments, 1989. Acoustic Doppler Current Profilers, principles of operation: A practical primer. RD Instruments, San Diego, CA, 36 pp..
- Rowe, F.D., and J.W. Young, 1979. An ocean current profiler using Doppler sonar. *IEEE Proceedings Oceans '79*, 292-297.
- Schramm, R. E., 1989. Experiences with the KVH Compass in RD Instruments Acoustic Doppler Current Profilers. *IEEE Proceedings Oceans '89*, 1314-1317.
- Sotirin, B. J. and J. L. Newton, 1993. Horizontal magnetic field fluctuations measured in the Lincoln Sea. *IEEE Proceedings Oceans '93*, II-30-II-34.
- Theriault, K. H., 1986. Incoherent multi-beam Doppler Current Meter performance, Part 1 - Estimate variance. *IEEE, Journal of Oceanographic Engineering*, **OE-11**(11), 7-15.

## DOCUMENT LIBRARY

*Distribution List for Technical Report Exchange - May 1995*

- University of California, San Diego  
SIO Library 0175C  
9500 Gilman Drive  
La Jolla, CA 92093-0175
- Hancock Library of Biology & Oceanography  
Alan Hancock Laboratory  
University of Southern California  
University Park  
Los Angeles, CA 90089-0371
- Gifts & Exchanges  
Library  
Bedford Institute of Oceanography  
P.O. Box 1006  
Dartmouth, NS, B2Y 4A2, CANADA
- Commander  
International Ice Patrol  
1082 Shennecossett Road  
Groton, CT 06340-6095
- NOAA/EDIS Miami Library Center  
4301 Rickenbacker Causeway  
Miami, FL 33149
- Research Library  
U.S. Army Corps of Engineers  
Waterways Experiment Station  
3909 Halls Ferry Road  
Vicksburg, MS 39180-6199
- Institute of Geophysics  
University of Hawaii  
Library Room 252  
2525 Correa Road  
Honolulu, HI 96822
- Marine Resources Information Center  
Building E38-320  
MIT  
Cambridge, MA 02139
- Library  
Lamont-Doherty Geological Observatory  
Columbia University  
Palisades, NY 10964
- Library  
Serials Department  
Oregon State University  
Corvallis, OR 97331
- Pell Marine Science Library  
University of Rhode Island  
Narragansett Bay Campus  
Narragansett, RI 02882
- Working Collection  
Texas A&M University  
Dept. of Oceanography  
College Station, TX 77843
- Fisheries-Oceanography Library  
151 Oceanography Teaching Bldg.  
University of Washington  
Seattle, WA 98195
- Library  
R.S.M.A.S.  
University of Miami  
4600 Rickenbacker Causeway  
Miami, FL 33149
- Maury Oceanographic Library  
Naval Oceanographic Office  
Building 1003 South  
1002 Balch Blvd.  
Stennis Space Center, MS, 39522-5001
- Library  
Institute of Ocean Sciences  
P.O. Box 6000  
Sidney, B.C. V8L 4B2  
CANADA
- Library  
Institute of Oceanographic Sciences  
Deacon Laboratory  
Wormley, Godalming  
Surrey GU8 5UB  
UNITED KINGDOM
- The Librarian  
CSIRO Marine Laboratories  
G.P.O. Box 1538  
Hobart, Tasmania  
AUSTRALIA 7001
- Library  
Proudman Oceanographic Laboratory  
Bidston Observatory  
Birkenhead  
Merseyside L43 7 RA  
UNITED KINGDOM
- IFREMER  
Centre de Brest  
Service Documentation - Publications  
BP 70 29280 PLOUZANE  
FRANCE